Lehigh University
Lehigh Preserve

Theses and Dissertations

1-1-2018

Monte Carlo Studies of Patchy Ellipsoids

Thienbao Nguyen Carpency
Lehigh University, thienbaon@gmail.com

Follow this and additional works at: https://preserve.lehigh.edu/etd

 Part of the Biophysics Commons

Recommended Citation
Carpency, Thienbao Nguyen, "Monte Carlo Studies of Patchy Ellipsoids" (2018). *Theses and Dissertations*. 4268.
https://preserve.lehigh.edu/etd/4268

This Dissertation is brought to you for free and open access by Lehigh Preserve. It has been accepted for inclusion in Theses and Dissertations by an authorized administrator of Lehigh Preserve. For more information, please contact preserve@lehigh.edu.

Monte Carlo Studies of Patchy Ellipsoids

by

Thienbao Nguyen Carpency

A Dissertation
Presented to the Graduate Committee
of Lehigh University
in Candidacy for the Degree of
Doctor of Philosophy
in
Physics

Lehigh University
January 2018

Copyright
Thienbao Nguyen Carpency

Approved and recommended for acceptance as a dissertation in partial fulfillment of the requirements for the degree of Doctor of Philosophy.

Thienbao Nguyen Carpency
(Monte Carlo Studies of Patchy Ellipsoids)

Date

Dr. James D. Gunton, Dissertation Director, Co-chair

Dr. Jeffrey M. Rickman,Dissertation Director, Co-chair

Accepted Date

Committee Members

Dr. Dimitrios Vavylonis

Dr. H. Daniel Ou-Yang

Dr. Javier Buceta

If I have known any degree of professional success at Lehigh, it would be, no doubt, impossible without the guidance, tutelage, and kindness of Dr. James Gunton who was my teacher, advisor and also my friend. To him, I owe immense gratitude.

To Dr. Rickman, thank you for your time, your patience, and instruction especially in the final years of my time at Lehigh.

I would also like to thank my committee members, Dr. Vavylonis, Dr. Ou-Yang, and Dr. Buceta for their encouragement and interest. In particular, I appreciate Dr. Vavylonis who brought me to Lehigh and also was a source of guidance and support.

To my group members and fellow graduate students, past and present, thank you for the ups and downs, the advice, the camaraderie, for making the little office and the everyday work of graduate student life feel not so lonely.

And finally thank you to my friends and family, especially my husband. My most treasured experiences during these years have been made with you.

This work is dedicated to the memory of fellow physics students and my beloved friends Isaac James Clark and Nickolas Adam Williams.

Contents

List of Tables

List of Figures

Abstract

Colloidal particles undergoing spontaneous aggregation are a system of interest. Protein aggregation has been shown to be an important pathway to disease and novel materials with new and desired properties can be synthesized quickly and effectively if they undergo self-assembly. Understanding this self-assembly and the mechanisms that cause it are of tantamount importance to solving these problems in biology and engineering. The simplest model particle is a hard, incompressible sphere. Simulation studies of these types of particles display different behaviors under different conditions illustrated on a phase diagram. Since this original study, particles with additional levels of complexity, anisotropic shape or directional attractive interaction have been studied in simulation and have demonstrated a wide variety of behavior. In this work, anisotropic shape ellipsoids and directional patchy interactions are combined in the model particle. The liquid-liquid phase transitions of these patchy ellipsoids are mapped out via Monte Carlo simulation techniques. Both increasing shape elongation and decreasing patchy surface act to depress the location of the critical temperature on the phase diagram. Thermodynamic properties of the dense fluid phase of patchy ellipsoids are also calculated and finite size effects are discussed. Additionally particle patch distribution is affected by elongated shape and found to have an effect on resultant phase behavior.

Chapter 1

Introduction

One of the fundamental aims of statistical mechanics is to link particle-particle type interactions to large scale thermodynamic behavior, such as the heat capacity, thermal conductivity, chemical potential or especially the phase behavior. Phase diagrams in particular are powerful because they provide a map that shows the particular conditions under which a substance will exist in some particular phase. Commonly known phases are liquid, solid, gas, but there is a plethora of research that shows the existence of distinct phases in between.

In general, a phase in a material can be characterized by the degree of order. A gas for example has little to no order, whereas a solid is a very ordered state. Self-assembly occurs when particles spontaneously come together and acquire some order from an initial state of less order. Therefore particles that undergo self assembly are also said to experience a phase transition.

The nature of the particle itself is important in determining how a group of particles react to certain thermodynamic conditions. It has been shown that real sythesized particles interacting with each other via anisotropic interactions can self-assemble into novel and interesting shapes. [26] [47] [68] [135] [136] [106]Additionally, biological molecules, such as proteins, are highly anisotropic. Proteins can self-assemble to a vast array of morphologies including crystals, gels, filaments and amorphous aggregates. This self-assembly is fundamental in either the proper or pathological expression *in vivo*.[78] For example the effect of anisotropic surface

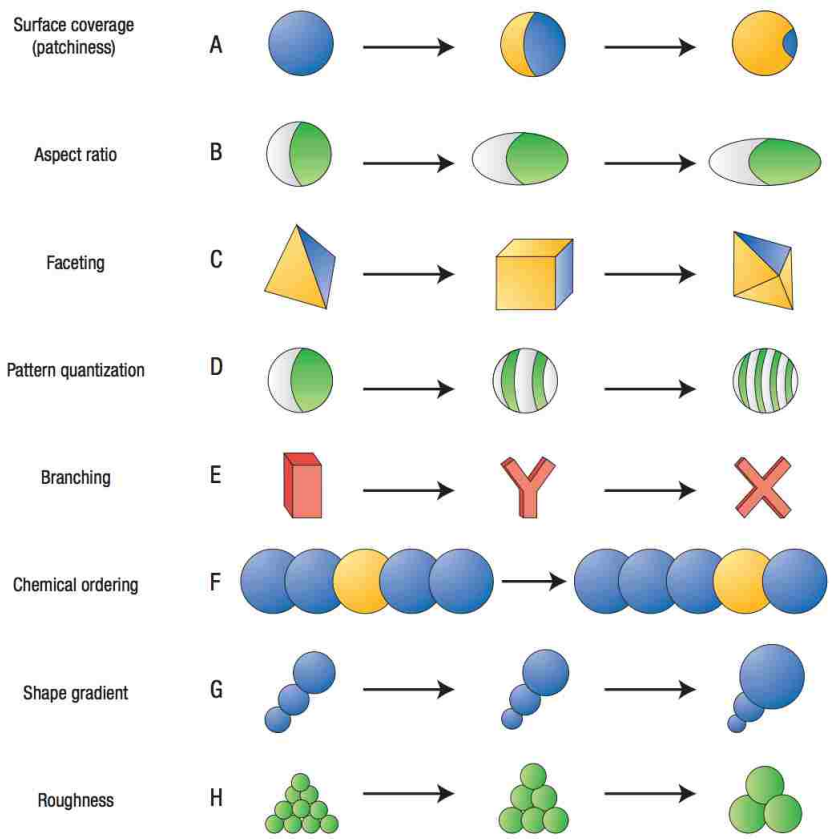

Figure 1.1: Anisotropy Dimensions used to categorize particles that interact via anisotropic interactions due to key features shown.

morphology, known as roughness, can affect protein adsorption. [107] Also conformational changes affect the aggregation of amyloid beta protein to form fibrils. [65]. Already there is a stunning array of particles that have been created and characterized displaying a vast variety of behaviors. [63][68] [2] [106]

In 2006, Glotzer and Solomon summarized this then emerging research and categorized self-assembling particles via what they called anisotropy dimensions. At the time they identified eight anisotropy dimensions. These are summarized in the following Figure 1. [47]

Particles with some type of anisotropy might be more or less likely to self-assemble than another similar particle under the same conditions because of even slight changes in anisotropy dimension changing the location and shape of the resultant phase diagram. [119]

Computational studies have also been performed on particles undergoing self-assembly. This has been on-going for many decades and proceeds the widespread usage of the term self-assembly. For example one of the anisotropy dimensions identified in 2006 was particle shape. Ellipsoidal particles have been studied via computational means since the 1950s. [5]

The advantages of computational methods are numerous. Computers can perform many exhausting calculations quickly and efficiently. Simulation studies are a type of computational method that aims to replicate a real physical system using the number crunching power of computers. In a simulation study, an idealized system with precisely the desired properties can be realized relatively quickly compared to experiments that often encounter many challenges in acheiving the exact desired conditions.

Computers work with as much or as little information as is given to them. Given the right information, computers can perform calculations leading to exact numerical results, and also overlook finer details of a system that are extraneous in the ultimate calculation.

The creation of computational models is a non-trivial and nuanced task. Too much information will slow down a calculation, leading to, at best, unnecessary delays. If a model retains too little infomation, it may not be an effective model for study. Knowing what features of a model are ultimately relevant, is often the work of educated trial and error, but knowing what key features underlie a particular behavior is critically important. For example Hungtinton's disease is one of a set of neurodegenerative diseases known to be related to an expanded polyglutamine repeat sequence near the N-terminus in the associated Huntingtin protein. [99] Therefore modeling efforts have focused on this and related parts of the protein. [66] [31] [138]

Computational models therefore provide idealized systems that allow for the

testing of theories and comparision with experiment.

In general there are two main types of computer simulation methods, Monte Carlo and molecular dynamics. The main goal of the Monte Carlo method is to investigate systems in equilibrium. Whereas molecular dynamics simulations study the dynamic progression of a system, Monte Carlo methods are used to study a system in equilibrium. Since phase diagrams represent the states of matter for some material under equilibrium conditions, Monte Carlo methods were chosen for the extent of this work.

Combining computer simulation with the study of anisotropy and its effect on phase diagrams is the goal of this work. In particular, the two anisotropy dimensions, called patchiness and shape are of interest.

Patchy particles form a whole class of particles that interact via highly directional interactions that are isolated on specific regions of the particle surface area known as a patch. Experimentally patchy spheres have been shown to self assemble into interesting non-close-packed structures due to the presence of patchiness. [63][68] [2] [106] For example triblock patchy hard spheres have been shown to self-assemble into a kagome lattice which has a particularly desired porous structure. [26].

As for computer simulations of patchy particles, the seminal work of Kern and Frenkel in 2003 provided the basis for many following studies on patchy spheres.[60] [46] [114] [18] Simulation studies of this model has shown that patchy spheres can assemble into wires, lamellae and other shapes. [84]

Further complexity is added when one considers shape anisotropy as well. As previously mentioned, studies of particles with shape anisotropy have existed for decades and have shown that anisotropic shape gives rise to novel phases that are not present in the case of isotropic shape. [42] [41] [91] [50] [92] [13]

However it is only recently that both shape and patchy types of anisotropy have been studied congruently. The work of the Gunton group has been instrumental in these studies. Since it was found that patchy particles self-assemble into a diversity of shapes, previous work in the Gunton group focused on either squeezing or elongating the patchy sphere shape into a patchy ellipsoids and studying the resultant aggregates. [74] [70] [71] [72] [115]

This thesis is a continuation of that work, but is also distinct in that here the phase diagram of patchy ellipsoids is explored extensively and with greater variety. Previous work has focused solely on particles with one patch, covering half of the particle surface, Janus particles. Here, we present work on particles with a variety of patch coverages. Additionally the degree of shape anisotropy is also varied and characterized by a quantity known as the aspect ratio. For these model particles the liquid-vapor phase diagram is mapped. There is also a brief discussion of future work on the isotropic to nematic phase transition.

In a liquid-vapor phase transition, under the right conditions, a fluid of particles will spontaneously self-assemble into a particle-rich fluid and a particle-poor fluid. This is the type of phase transition that has been studied most commonly in previous studies of patchy particles. This type of phase transition is also the type most commonly explored in experiments that aimed to determine the phase diagram of real proteins such as lysozyme and bovine pancreatic trypsin inhibitor. [78], [45] [48]

The liquid-vapor phase transition is characterized by the density of the equilibrium fluids. At temperatures above the critical point on the phase diagram the fluid of particles is homogeneous. At cooler temperatures the fluid will spontaneously separate. The densities of the resultant vapor phase and liquid phase at various temperatures form a curve that is known as a binodal or coexistence curve.

The structure of this work is broken into seven chapters. In chapter 2, the computational methods employed in the effort of studying phase diagrams is discussed in detail. This chapter provides a brief overview of the statistical physics that underlies the work, starting with the two main types of ensemble used NVT and NPT. There is a brief introduction to random sampling and the Monte Carlo method in general. The Metropolis algorithm in particular was employed and discussed as well as the various move types that are fundamental to the algorithm. Detailed-balance, microscopic reversibility and erogdicity, are explained as stipulations that must be met in order to guarantee accurate sampling of parameter space and that the simulation will eventually reach and stay in equilibrium. Special Monte Carlo techniques, the Gibbs ensemble and Replica Exchange Method, used for these studies are also

elucidated. Since computational simulation is only meaningful when connected with the real world, brief comments of the role of units is also included.

Chapter 3 is an overview of history of simulations studies that were done before and are relevant to this work. Starting with the simulation work on the phase diagrams of hard spheres having nontrivial volume and moving towards greater complexity. The hard ellipsoid problem is introduced. Limiting cases are discussed such as the case of infinitely long needles and the hard sphere. Simulation work is presented and discussed as there are two main studies on the hard ellipsoid problem. The first was done in the 1980s [41] [42] and the problem was revisited again in 2012. [92] [13] Simulation studies of patchiness are discussed in greater detail as is the type of interaction that is being modeled between any pair of interacting particles. Interesting morphologies of patchy particles are described. Relevant, existing phase diagrams are presented for all of these cases leading up to the case of patchy ellipsoids. Chapter 3, provides the reader some perspective and context for the rest of this work.

Chapter 4 begins the start of new work on the patchy ellipsoids. First we examined the liquid-liquid phase separation of particles with various elongations and with various amounts of surface patch coverage and patch number. This work closely follows the original study of Kern and Frenkel and aims to extend their results into the realm of ellipsoids. A standard NVT ensemble was used as well as the Gibbs ensemble method in conjunction with the law of rectilinear diameters to make estimates for the critical points. Results were analyzed with particular emphasis on the location of the critical point. It was found that the critical temperature T_c depends inversely on the degree of ellipsoid elongation. The critical density did not vary much. More elongated ellipsoids had lower critical temperatures. This T_c behavior was explained in several ways. Particle elongation seemed to correlate with decreasing bond strength between particles even though on average inter-particle distance did not seem to vary much with particle elongation. Additionally in order to hold particle volume constant, but increase elongation, particle surface area must necessarily increase. Therefore fractional patch coverage likely decreases with particle elongation. Finally elongated particles with directional interactions might

be inclined to undergo some sort of orientational change; so particle orientation was examined and indeed more elongated particles were more likely to adopt some average orientation than semi-spheres. This work was done on model particles with two patches and model particles with four patches.

Chapter 5 describes additional work that was done on the model in chapter 4 of patchy ellipsoid fluids for particles with two patches. Two thermodynamic properties, the response function, also known as the isothermal compressibility was examined as well as the specific heat. In the thermodynamic limit, these properties should diverge near the criticial points. Finite size effects introduce rounding errors and the divergence is smoothed out. These finite size effects are discussed as are the roles of shape and patchiness. Again using standard NVT ensemble Monte Carlo techniques, the dense fluid region of the phase diagram was explored. This chapter further illustrates how starting from a particle description, thermodynamic properties can be found.

In chapter 6, the phase diagram of patchy ellipsoids is examined again, but with emphasis on patchy distribution instead of aspect ratio. Patch distribution has not been a very well studied topic because in spheres particles with patches on diametrically different sides are identical. Since particles are allowed to rotate in simulation, a particle with patches on the top and bottom is identical to a particle with patches on the front and back. In ellipsoids however changing the overall particle shape necessities changes in the surface patches. A prolate ellipsoid with patches on the two pointy ends is not identical to a particle with patches on the two sides. The liquid-liquid phase separation of particles with two opposite patches is mapped out. In one case the two opposite patches are found at the polar ends of the model particle. In the second case, the two opposite patches are found at on the model particle's sides. Patch distribution is found to affect phase behavior between these two cases of particles, especially for particles with higher values of total patch coverage. Possible reasons underlying the differences between these two patch configurations are examined.

Moving beyond the liquid-liquid phase transition, chapter 7 introduces future work on the isotropic to nematic phase transition. The nematic phase is a distinct

feature that appears in the phase diagram of sufficiently elongated particles that is absent in the phase diagram for spheres. [41] [42] [92] [13] The transition point is characterized by examining the order parameters as well as other metrics. Published work on prolate ellipsoids in an encompassing attractive potential already exists. [132] The goal of the future work will be to study the effect of patches.

Chapter 2

Monte Carlo Methods

The advent of computer simulation brought about a huge advancement in science. There exist many problems in statistical physics, such as investigation into collective behavior, that require large data sets that would have been intractable without the use of computers. For many non-trivial problems, analytic solutions are difficult or impossible to attain so numerical calculation is necessary. Carrying out sums over all possible configurations is one of the predominant tasks in computational studies.

The Monte Carlo method, named after the famous gambling destination, is a method to simplify these calculations by generating a random sampling of possible configuration states and averaging over them. The simplest Monte Carlo method generates a random ensemble of all possible outcomes of a variable of interest and takes an average over that ensemble. For example, suppose we are interested in calculating the value of some definite integral over the range [a,b] (the area, of the curve between a and b).

$$\int_a^b f(x)dx \tag{2.1}$$

Using a random set of N points within the area A, $x_i \in [a, b]$, we evaluate the value of the function at each of those points $f(x_i)$. Taking an average over the values of $f(x_i)$, we can approximate the value of f.

$$\langle f \rangle = \frac{1}{N} \sum_{i=1}^{N} f(x_i) \tag{2.2}$$

In the continuous limit this is:

$$\langle f \rangle = \frac{1}{(b-a)} \int f(x_i) dx \tag{2.3}$$

As the number of random samples increases, then the accuracy of the expected value obtained also increases. In the case of more complicated integrals, the convergence of calculating such integrals via simple random Monte Carlo becomes increasingly slow with complexity. Above, the probability distribution of the particles was simply $\frac{1}{(b-a)}$, which is a flat line.

In statistical mechanics, in a sufficiently large system (such as a large number of identical particles), the Boltzmann distribution of the microstates of such a system would be quite sharp. It is useful therefore to weight the sampling according to the Boltzmann distribution.

A Monte Carlo method that uses what is called importance sampling relies upon weighted probabilities based on the Boltzmann distribution to compute average quantities such as the energy, magnetization or other thermodynamic quantities. In classical statistical mechanics, the partition function, the sum of all Boltzmann factors in a system, is constructed from an ensemble of all possible states of the system and essentially counts the number of accessible states. Importance sampling involves taking random samples where the Boltzmann factor is large and not sampling as often where the Boltzmann factor is small. Since certain states are more probable than others, an average over such an ensemble yields these quantities.

Before discussing details about how to schematically carry out importance sampling it is important to discuss the ensembles, all possible configurations that a system may occupy, that are used.

2.1 Ensembles

In statistical physics, a typical Monte Carlo simulation will be run in the canonical, NVT, ensemble so named because simulations run in such an ensemble have the number of particles N, volume V and temperature T fixed. Simulations in other ensembles are also common. The NPT ensemble (particle number, pressure and

temperature are fixed), for example, is also frequently used. In the thermodynamic limit, it shouldn't matter what ensemble is used; however different ensembles do give different values when calculating the root mean square value of fluctuations around desired thermodynamic quantities. Furthermore, the choice of ensemble also dictates the acceptance criteria that is used in the implementation of Monte Carlo programs in these ensembles. For example, simulations in a standard NVT ensemble obviously do not involve changes in volume of the simulation cell as a type of trial move so there is not acceptance criterion for this. However volume changes are a necessary part of simulations in the NPT ensemble where changing the volume is a means of keeping the pressure constant so the list of acceptance criterion changes to accommodate volume moves. This will be explained more later.

The choice of which ensemble to use is based on convenience. The NVT ensemble for example was the clear choice for simulation of the Ising model because the number of spins, the size of the simulation cell and the temperature could all be set easily. If one wants to compare the results from simulation directly with experiment, it might be wise to simulate in the NPT ensemble because those are the conditions often controllable in experiment.

Finally, before discussing more deeply each of the ensembles that were used, note that there exists additional methods to further increase the sampling rate by sampling more of the available configuration space at once as in the case of replica exchange or to simulate two phase equilibrium in one simulation as in the Gibbs ensemble method.

2.1.1 The Canonical (NVT) Ensemble

Consider the canonical ensemble of N identical particles. Particles in a NVT ensemble are as if they are in contact with a heat bath. The energy of the system is not constant and instead fluctuates around an average. It is also assumed that the particles only interact via an inter-particle potential. There is no external force field and the particles do not have some sort of extra internal energy.

If we wanted to calculate the expected value of some property, A, in the system,

this would be given by:

$$\langle A \rangle = \frac{\frac{1}{N!}\frac{1}{h^{3N}} \int dr^N dp^N A(r^N) \exp\left[-H(r,p)/k_B T\right]}{Q_{NVT}} \tag{2.4}$$

Notice that in this equation the probability distribution function is given by

$$p = \frac{\exp\left[-H(r,p)/k_B T\right]}{Q_{NVT}} \tag{2.5}$$

and Q_{NVT} is the canonical partition function this is written as:

$$Q_{NVT} = \frac{1}{N!}\frac{1}{h^{3N}} \int dr^N dp^N \exp\left[-H(r,p)/k_B T\right] \tag{2.6}$$

r^N denotes the position of all N particles. p^N is the momentum of the particles. h is Plank's constant. $H(r,p) = K(p)+U(r)$ is the Hamiltonian of that particles that can be written as the sum of a kinetic part, that depends only the the momentum (velocity) of the particles $K(p)$, and a potential part that depends only the the positions of the particles $U(r)$.

Substituting this into the partition function, Q_{NVT} can be factorized such that the kinetic contribution and the potential contribution.

$$Q_{NVT} = \frac{1}{N}\frac{1}{h^{3N}} \int dr^N exp\left[U(r)/k_B T\right] \int dp^N exp\left[K(p)/k_B T\right] \tag{2.7}$$

The second part of the integral is just the well-known ideal gas contribution. This is important because in simulation we do not need to deal with the momentum/velocity of the particles. The first part of the integral, known as the configuration integral is the part that remains important.

$$Q_{NVT} \propto \int dr^N exp\left[U(r)/k_B T\right] \tag{2.8}$$

This means that we only need to look at the particle positions in simulation and the inter-particle potential. Note that the probability distribution of random samples is now given by a factor that depends on the exponential of the internal energy and the partition function.

2.1.2 The Isobaric-Isothermal NPT Ensemble

Now consider the NPT ensemble, with constant pressure P in addition to constant N and T. In this case, the system is in contact with both a thermostat and a bariostat, and it is allowed to exchange volume (work) with the bariostat. This means that the system is not at constant energy or volume, but both values fluctuate around some average.

NPT ensemble methods are useful in the case of first-order phase transitions because at constant pressure the system can transform into a state of lowest Gibbs Free Energy. In a standard NVT ensemble, the system, may try to phase separate, but is prevented from doing so because of finite-size effects.

For the most part, the NPT ensemble is similar to the NVT ensemble, except the important difference is that volume is no longer fixed.

As before, to calculate some quantity, A, in the NPT ensemble one needs to evaluate:

$$\langle A \rangle = \frac{\frac{1}{N!}\frac{1}{h^{3N}}\frac{1}{V_0}\int dr^N dp^N A(r^N) \exp\left[-(H(r,p)+PV)/k_B T\right]}{Q_{NPT}} \tag{2.9}$$

The partition function in the NPT ensemble is given by:

$$Q_{NPT} = \frac{1}{N!}\frac{1}{h^{3N}}\int dr^N dp^N \exp\left[-(H(r,p)+PV)/k_B T\right] \tag{2.10}$$

Since the volume in an NPT ensemble is variable it is useful to have some dimensionless quantity in place of the coordinate r in the integral. Therefore assuming that we are integrating in some space between -L/2 and L/2 then we can use the dimensionless quantity $s = r/L$. Additionally, leaving out the kinetic part of the integral leaves the configuration integral:

$$Z_{NPT} = \int ds^N \exp\left[-U(s^N)/k_B T\right] \int dV V^N \exp\left[-PV/k_B T\right] \tag{2.11}$$

And (2.9) can be rewritten as:

$$\langle A \rangle = \frac{\int_0^\infty dV V^N \exp\left[-PV/k_B T\right] \int ds^N A(s^N) \exp\left[-U(s^N)/k_B T\right]}{Q_{NPT}} \tag{2.12}$$

This means that the probability distribution function is:

$$p = \frac{\exp\left[-(N\ln(V)PV + U(s^N))/k_B T\right]}{Q_{NPT}} \tag{2.13}$$

2.2 Implementation

2.2.1 The Metropolis Algorithm

In simulation, the scheme to carry out this random but weighted sampling is called the Metropolis method. First some configuration of the system is created with a non-vanishing Boltzmann factor. Next, we create a second configuration which differs from the first by some small trial move. The difference in energy between the two trial moves is calculated. If the difference is found to be such that the trial move lowered the system energy, the move is accepted. Otherwise, a random number if generated. This number is then compared to the quotient of the Boltzmann Factor of the two states. If the random number is greater than this quotient, the move is rejected. If it is less than the quotient, the move is accepted. Whether the move was accepted or not, the algorithm will repeat the process, generating another trail move from whatever configuration it is in. Each step of this process is can be called a Monte Carlo step. Each Monte Carlo step produces a new configuration and the sequence of these configurations creates the ensemble of states. Furthermore, this type of Monte Carlo algorithm is also an example of a Markov Chain Monte Carlo since the probability of being in some state depends on the probability of being in the state before.

Fig. 2.1 depicts these steps.

2.2.2 Trial Moves and Associated Acceptance Rules

For a system of particles in a box, the first and most obvious type of trial move is that of particle translation.For the sake of being able to move from easily from one configuration state to the next (and back), one particle is chosen in the box and translated some distance $\Delta\vec{r}$ which is a function of some random number. For example $\delta r_x = r_x + (random - 0.5)$, $\delta r_y = r_y + (random - 0.5)$ and $\delta r_z = r_z + (random - 0.5)$ and $random$ is a random number between 0 and 1.

To ensure equilibrium a property called detailed balance must hold. Therefore,

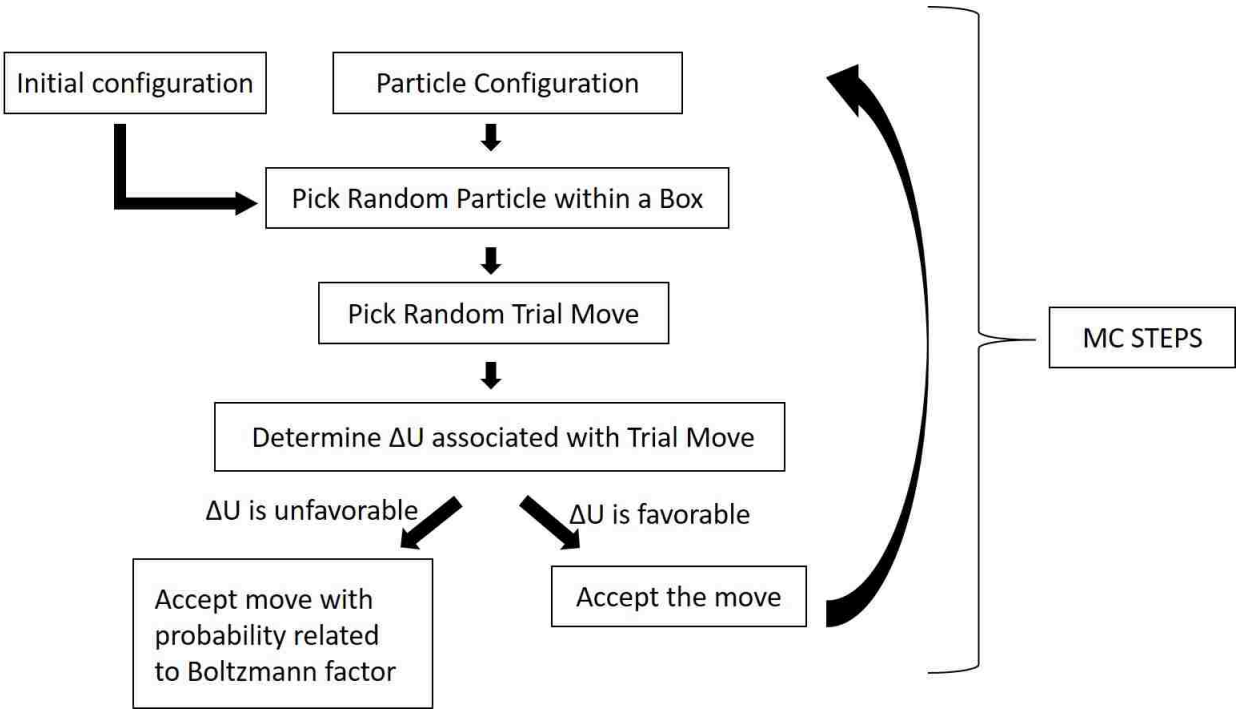

Figure 2.1: Figure schematically depicting a typical Monte Carlo run

the probability of being in any particular state i, P_i times the probability of transitioning out of it $\kappa(i \to j)$ of it must be equal to the probability of being a state j, P_j and transitions back $\kappa(j \to i)$.

$$P_i \kappa(j \to i) = P_j \kappa(i \to j) \tag{2.14}$$

The transition probability is itself a product of the probability to generate the state i from j and the acceptance probability of such a move $acc(i \to j)$.

$$\kappa(i \to j) = \alpha(i \to j) acc(i \to j) \tag{2.15}$$

Since $\alpha(i \to j)$ must equal $\alpha(j \to i)$, substituting into (2.14) gives:

$$P_i acc(i \to j) = P_j(j \to i) \tag{2.16}$$

Since $P_i = \frac{\exp[-U_i/k_BT]}{Q_{NVT}}$ and $P_j = \frac{\exp[-U_j/k_BT]}{Q_{NVT}}$. This implies:

$$\frac{acc(i \to j)}{acc(j \to i)} = \frac{P_j}{P_i} = \exp -(U_j - U_i/k_BT) \tag{2.17}$$

Therefore the associated acceptance rule for a trial translation move is given by:

$$acc(i \to j) = min\left\{1, \exp -(U_j - U_i)/k_BT\right\} \tag{2.18}$$

For an orientational move, such as a particle rotation, the associated acceptance rule is the same as for translation since the probability distributions also come from the NVT ensemble.

Using the NPT ensemble in a similar way, it follows that the associated acceptance rule for a trial volume change from a state with volume V to a state with volume V' is $V' = V + \Delta V$ where $\Delta V = 0.5Vrandom$ and associated energy change i to j is:

$$acc(i \to j) = min\left\{1, \left(\frac{V'}{V}\right)^N \exp\left[-(U_j - U_i) + P(V' - V)\right]/k_BT\right\} \tag{2.19}$$

2.2.3 Ergodicity

In order for any simulation algorithm to be valid it is also important to note that there must be some nonzero probability of visiting all possible system states in whatever ensemble. This is called ergodicity. A system is called ergodic if it is possible to reach every possible configuration in a finite number of Monte Carlo steps. In a truly ergodic system whether or not a system reaches equilibrium also does not depend upon the initial configuration of the system. That does not mean that the efficiency of reaching equilibrium is not affected by initial conditions. For example starting a system of particles in a crystal state with the intention of melting into a liquid can become tricky near a metastable point where the system will spend a very long time in a state other than equilibrium. If it is found that after a series of Monte Carlo steps the system depends on the initial configuration either the system was somehow non-ergodic, or more likely, the simulation simply has not been run for long enough to reach equilibrium.

2.2.4 Detailed Balance and Microscopic Reversibility

Another important aspect of Monte Carlo algorithms, as mentioned above, is that they must satisfy detailed-balance. Detailed balance is important because it is the condition that ensures that such a sampling will eventually lead the simulation to equilibrium and stay there such that in equilibrium the simulation can be stopped and measurements made at anytime.

In order to stay in equilibrium, the probability of the system moving from one state, A, to another state, B, must exactly equal the probability of moving back to A (from state B or any other state). This is similar to the principle of microscopic reversibility which states that in a dynamic system, when one reaches equilibrium, there may be activity at the atomic or molecular level, but the system as a whole is observed to be unchanging.

In 1999, Manousiouthakis and Deem showed that strict detailed balance is not necessary to reach equilibrium, that a weaker balance condition was sufficient. [77]

To explain the difference between strict detailed balance and just balance, consider the one-dimensional Ising model where up or down spins are all in some sort of configuration along a line. In a Monte Carlo scheme that obeys detailed balance, a trial move would involve picking one of the spins in the line at random and flipping it. After determining whether this move was accepted or not, in the next Monte Carlo step, another spin would be selected at random, with the probability of the original spin being selected again equal to the probability that all other spins are selected for a trail move.

By contrast, in a Monte Carlo scheme that obeys just the balance condition, one can move sequentially down the line selecting spins. This example illustrates how the balance condition violates detailed balance since the probability of moving from a state B back to A (the initial spin is chosen again and is flipped back to the original configuration) is zero. In practice, simulations that do not follow detailed balance are often wrong, especially in the case of Monte Carlo algorithms that employ multiple types of moves so it is still considered good practice to follow the detailed balance condition.

Quantity	Reduced Units	Real Units
temperature	$T* = 1$	$T = 119.8K$
density	$\rho* = 1$	$\rho = 1680kg/m^3$
pressure	P*=1	$P = 41.9MPa$

Table 2.1: Table of relevant reduced units used in simulation and their connect to real units.

2.2.5 Reduced Units

It is also important to consider the units of the results of any simulation. It is often convenient to use what are called reduced units. The basic ideas behind reduced units is that we pick convenient units based on convention and the specifics of our problem and express all other quantities according to those units. For example, in the following chapter on the fluid-fluid phase separation of patchy ellipsoids, we use the $2a$ where a is one of the semi-axes of our model ellipsoids as the fundamental length unit, $\sigma = 2a$ and express all other lengths in terms of this unit.

By convention there are other standard versions of reduced units and these and often denoted by the star notation. $T* = k_BT/\varepsilon$ is the reduced temperature in a simulation. k_B is the standard Boltzmann constant. ε is the chosen unit of energy. $u* = u/\varepsilon$ is the normalized reduced energy of the system. $\rho* = \rho\sigma^3$ is the reduced density. $P = P\sigma^3/\varepsilon$ is the reduced pressure.

One of the primary benefits of using reduced units is clear. The Boltzmann constant in SI units is on the order of 10^{23}. Carrying such a quantity around during simulation would become very computationally expensive. The use of reduced units therefore allows for quantities to remain within reasonable order. One other important aspect of reduced units is that they allow for the possibility of direct comparison between two systems using the law of corresponding states. If such a correspondence existed between them, they would exhibit the same behaviors at the same reduced units.

In their book, Frenkel and Smit offer a table to convert between reduced units and standard SI units. The relevant aspects of are reproduced in Table 2.1.[43]

2.2.6 Periodic Boundary Conditions and The Nearest Neighbor Convention

Returning to the one-dimensional Ising model, suppose that one were to write a Monte Carlo method that sampled using the balance condition. It has been proven that doing this will eventually lead to the same result as in the detailed balance case. However, since simulation size is finite, at some point, sampling sequentially, one will reach the end of the line of spins. This is an example of a boundary effect. At the boundaries, properties can be very different than in the bulk, so it is often desirable to avoid boundary effects. A common method of doing this to implement periodic boundary conditions. In the case of the one-dimensional Ising model, an implementation of periodic boundary conditions would simply be to write within the lines of the simulation code that if one comes to the end of a line of spins, take the first spin in the line and treat that as the next spin and continue as before. Doing so, creates a pseudo-infinite simulation space and avoids encountering the boundary.

For the case of a two or three-dimensional simulation, such as a box of fluid particles, each dimension will be subjected to periodic boundary conditions individually. In this case, one can imagine that a simulation cell is surrounded by an infinite number of other simulation cells that are exactly like itself such that if a particle moves towards the boundary of the simulation cell, it will simply reappear again directly across from where it disappeared. Fig 2.2 gives an idea of what this would look like.

Note that, this implies that the maximum range of an interaction potential between two particles in simulation is one-half the size of the simulation cell. If there exist only two particles, A and B, in a simulation, B to the left of A, and they are separated by more than the one-half the size of the simulation cell, then particle A does not interact with particle B, rather, particle As nearest neighbor is the image of particle B to the right of A. Periodic boundary conditions are important, because, like reduced units, they are necessary part of making computer simulations tractable. The average computer can handle degrees of freedom on the order of 10^5 or 10^6. In a one-dimensional Ising model where spins can flip only one of two

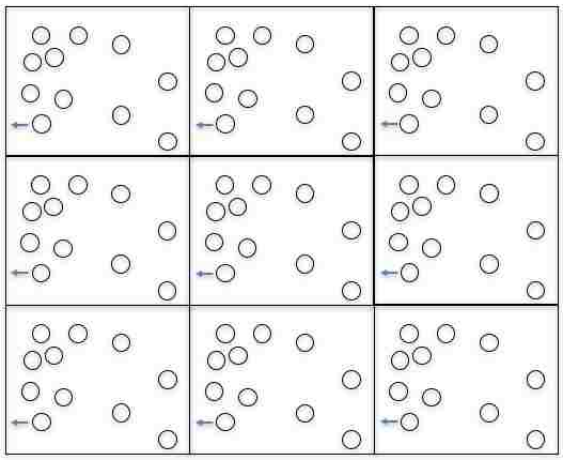

Figure 2.2: A schematic showing periodic boundary conditions for a two-dimensional simulation of box with fluid particles

directions, up or down, a 100-spin system would have 2^{100} degrees of freedom which is on the order of 10^{30}, this would be intractable and 100 spins is pathetically short of the thermodynamic limit.

2.3 Special Techniques

2.3.1 The Gibbs Ensemble

The Gibbs Ensemble method is a type of NVT simulation that is unique because it allows for two phases to be simulated at once. In a real experiment, when a system undergoes phase separation, one can see two distinct phases and a the boundary between them and it is relatively straightforward to measure the properties of the two phases. In simulation, because there are many fewer particles. Therefore the boundary effects become significant since most particle would be at the boundary. Thus one has to indirectly measure the thermodynamic properties at equilibrium.

The basic idea of the Gibbs ensemble method is that two simulation cells are run simultaneously each with its own set of periodic boundary conditions. Particles are dispersed inside the two boxes and the configurations are allowed to undergo a set

of trial moves: particle translation, particle rotation, particle swapping and volume change.

Since the Gibbs ensemble method is done in the NVT ensemble, the total number of particles N and the volume V should remain constant. The number of particles in one box is n_1 and the other is $n_2 = N - n_1$. Also the volume in one box is V_1 and the other box has volume $V_2 = V - V_1$. If a particle is moved out of one box, it is necessarily transferred to the other simulation box. Likewise if the volume of one box was scaled to become larger or smaller, the other box would also change size becoming smaller or larger respectively. The temperature in simulation boxes is the same.

Note that it is the particle swap move in particular from which the Gibbs ensemble method derives its advantage in simulating phase separation. Since the order parameter of an isotropic liquid is the difference in density, the connection between particle insertion and liquid-liquid phase separation is obvious. However the Gibbs ensemble method is only really useful for simulation of vapor-liquid or liquid-liquid phase separation. Since a solid phase would be too dense the probability of particle swapping in a very dense system would be very small.

The associated acceptance rules for these trial moves are as follows:

For translation and rotation:

$$acc(i \to j) = min\left\{1, \exp\left[-(U(s_j^{n_1}) - (U(s_i^{n_1})\right]\right\} \tag{2.20}$$

For volume change:

$$acc(i \to j) = min\left\{\frac{(V_1^j)^{n_1}(V - V_1^j)^{N-n_1}}{(V_1^i)^{n_1}(V - V_1^i)^{N-n_1}} \exp\left[-(U(s_j^{n_1}) - (U(s_i^{n_1})\right]\right\} \tag{2.21}$$

And for particle exchange:

$$acc(i \to j) = min\left\{1, \frac{n_1(V - V_1)}{(N - n_1 + 1)V_1} \exp\left[-(U(s_j^{n_1}) - (U(s_i^{n_1})\right]\right\} \tag{2.22}$$

The implementation of the Gibbs ensemble method follows the Metropolis algorithm with the addition that before a trial move is chosen at random, first a trial simulation box is chosen at random. If a particle exchange or volume change is

made then both boxes are affected, otherwise the boxes run as if two independent NVT simulations.

Fig. 2.3 depicts the Gibbs ensemble trial moves.

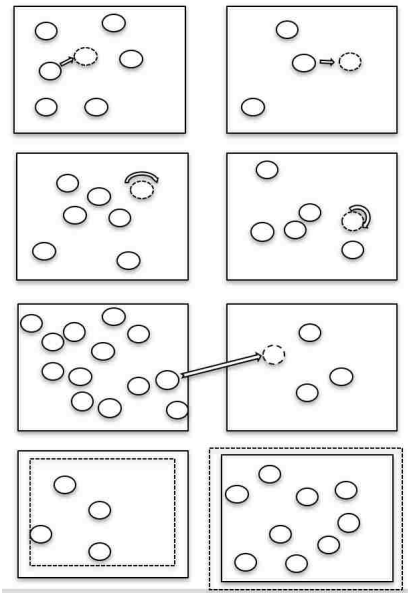

Figure 2.3: Figure depicting the two simulation boxes and the various types of trial moves that occur during a Gibbs ensemble simulation

Note that in order to reach phase equilibrium with two phases in coexistence, the intensive variables in each of the two boxes: pressure, temperature and chemical potential, should be equal to one another. This is one way to determine that equilibrium is reached. Another way to determine equilibrium is to make a graph of the densities of the simulation boxes as a function of Monte Carlo steps. At the start of the simulation, before equilibrium is reached the densities will gradually start to change as the simulation goes through trial moves. Once equilibrium is reached, the box densities will continue to fluctuate, but these fluctuations will be relatively small and around some average. In equilibrium, the system essentially just samples one of two configurations that correspond to equilibrium with some fluctuation. This corresponds, on the graph, to a bifurcation of the densities, that plateaus out and oscillates around some high density value and some low density value.

2.3.2 Law of Rectilinear Diameters

In the vicinity of critical points the curvature of the coexistence curve flattens out. Therefore small external factors can lead to large fluctuations in density. At conditions too close to the critical point, these fluctuations will become too large to reliably use the Gibbs ensemble method. So other methods to calculate the critical point are necessary such as the law of rectilinear diameters.

Proposed in 1886, the law of rectilinear diameters is a means of extrapolating from coexistence data to the critical point. The idea behind the law is that the average of density of the coexisting liquid and gas are linear with respect to temperature up to the critical point.In practice by solving a system of equations

$$(\rho_{liq} + \rho_{gas})/2 = \rho_c - A \cdot |T - T_c| \tag{2.23}$$

$$(\rho_{liq} + \rho_{gas}) = B \cdot |T - T_c|^{0.32}\,, \tag{2.24}$$

A and B are parameters determined by a best fit to existing data. [21]

Although the law has been shown to be only approximate, it often overestimates the curvature of the coexistence line and it does not work for a mixture, the law has held up very well such that deviations from the law are often undetectable in experimental work. The law of rectilinear diameters therefore remains a well established means of determining critical points.

2.3.3 Parallel Tempering and Replica-Exchange

As a means of speeding up the sampling of a free energy landscape with many local minima, the method of parallel tempering was introduced. The basic idea of the method is to run n-copies of a system each at a different state that varies in some parameter. The method of parallel tempering varies the temperature of the n copies of an NVT ensemble. Low temperature ensembles probe local minima, but in order to prevent them from getting stuck over long times, their configurations are periodically swapped with high temperature ensembles according to some probability again

related to the Boltzmann distribution. The n-copies can then be ordered according to temperature $T_1, T_2 ... T_n$.

The extended partition function of these n copies is given by

$$Q_{extended} = \prod_{i=1}^{n} Q_{NVT_i} = \prod_{i=1}^{n} Q_{NVT_i} = \frac{1}{N!}\frac{1}{h_i^{3N}} \int dr_i^N dp_i^N \exp\left[-H(r_i, p_i)/k_B T_i\right] \tag{2.25}$$

The NVT ensembles are then each run in parallel individually with standard particle translation and rotation moves. Periodic swap moves between the n copies must follow detailed balance. Using similar notation as before the probability of swapping configurations between some ensemble i and another ensemble j is given by

$$P_i \kappa((i, \beta_i)(j, \beta_j) \rightarrow (j, \beta_j)(i, \beta_i)) = P_j \kappa((j, \beta_j)(i, \beta_i) \rightarrow (i, \beta_i)(j, \beta_j)) \tag{2.26}$$

And again

$$\kappa((i, \beta_i)(j, \beta_j) \rightarrow (j, \beta_j)(i, \beta_i)) = \alpha((i, \beta_i)(j, \beta_j) \rightarrow (j, \beta_j)(i, \beta_i)) acc((i, \beta_i)(j, \beta_j) \rightarrow (j, \beta_j)(i, \beta_i)) \tag{2.27}$$

Since swap trials $\alpha((i, \beta_i)(j, \beta_j) \rightarrow (j, \beta_j)(i, \beta_i))$ must be equal for all i and j this implies:

$$\frac{acc((i, \beta_i)(j, \beta_j) \rightarrow (j, \beta_j)(i, \beta_i))}{acc((j, \beta_j)(i, \beta_i) \rightarrow (i, \beta_i)(j, \beta_j))} = \frac{P_j}{P_i} = \exp -((\beta_i - \beta_j)(U_j - U_i)) \tag{2.28}$$

Therefore the associated acceptance rule for a trial translation move is given by:

$$acc((i, \beta_i)(j, \beta_j) \rightarrow (j, \beta_j)(i, \beta_i)) = min\left\{1, \exp -((\beta_i - \beta_j)(U_j - U_i))\right\} \tag{2.29}$$

Note that if the temperature difference between any two copies is too large, the probability of swapping between them, is small so it is important that the incremental temperature between each copy is small.

This parallel tempering works for a system in which energy interactions are dominant, but for hard-core systems in which excluded volume and entropy is also

(or more) important, extending the ensembles in pressure can be more useful since entropically driven structures are not as affected by temperature.

In the replica exchange method, n NPT ensembles are run in parallel with standard translation and volume moves. The extended partition function is

$$Q_{extended} = \prod_{i=1}^{n} Q_{NP_iT} = \prod_{i=1}^{n} Q_{NP_iT} = \frac{1}{N!}\frac{1}{h_i^{3N}} \int dr_i^N dp_i^N \exp\left[-(H(r_i, p_i) + P_i V_i)/k_B T\right] \tag{2.30}$$

and associated swap acceptance

$$acc((i, P_i)(j, P_j) \rightarrow (j, P_j)(i, P_i))) = min\left\{1, \exp -((P_i - P_j)(V_j - V_i))\right\} \tag{2.31}$$

Where $V_i - V_j$ is the volume difference between ensembles i and j and $P_i - P_j$ is the pressure difference. Notice that the energy between systems is not considered, as in the parallel tempering method. And again, the difference in pressures should be small enough that the probability of swapping is nontrivial. This is especially important at phase transitions points where $|V_i - V_j|$ can be large. Furthermore there is a dependence on system size. Larger systems sizes can have a more narrow density distribution such that the swap acceptance rate decreases.

In both parallel tempering and replica exchange, the methods above describe the swapping of particle configurations. However in practice it is more efficient to swap the temperature and pressure values during the course of a simulation run since that means just swapping one number, instead of the entire configuration of particles. The output of the simulation runs, can be collated at the end according to the temperature or pressure.

2.4 Random Numbers Generators

Finally, the Monte Carlo method relies heavily on random number generators. In truth, these generators are not perfect and can only produce pseudo-random numbers. Meaning that in the long run, in a sequence of generated random numbers, a pattern will begin to emerge.

The method by which a pseudo random number is generated depends upon the use of some mathematical algorithm that is repeated extensively to create the next number in the sequence as well as a starting number seed.

There are two major families of random number generators, linear and nonlinear. The second, linear is much slower but can make much larger samples before some pattern is observed. The Mersenne Twister algorithm developed in the late 1990s relies upon a linear matrix recurrence method and is one of the most predominant types of random number generators used in science today. This is because the method is known for having a period of $2^{19937} - 1$ (the largest known prime in a Mersenne sequence) which means that the Mersenne Twister method will create that number of random numbers before a pattern will emerge.

For this reason the Mersenne Twister random number generator was the one that was used for the content of this work.

Chapter 3

The Patchy Ellipsoid Problem

Ellipsoids are a model system that is both interesting and useful. Ellipsoidal shape is anisotropic, meaning that it has nonuniform behavior that depends on orientation. Ellipsoids undergo more complex phase behavior than spheres. Many systems of interest rely on ellipsoidal models. Systems as diverse as viruses [27] [6] and laponite clays [30] [116] have been described by researchers employing ellipsoidal descriptions. Models with increasing complexity from the most simple (spheres) to ellipsoids with high anisotropy are an effort to capture the cogent properties of many interesting problems.

3.1 The Hard Core Potential

3.1.1 Hard Spheres

The most idealized and simple system in thermodynamics is of course the ideal gas. Moving towards a more realistic description of particles, one of the first advances was the concept that particles could be more than just infinitesimally small, that they could occupy some volume. Theoretically this idea has been around since van der Waals, whose famous equation of state includes a term that accounts for the volume of the particles.

Taking the particle volume idea alone, one of the first systems ever studied using

the techniques of computer simulations was the hard sphere problem. In this system, identical rigid spheres interact solely via a hard core potential that is defined:

$$U(r) = \begin{cases} \infty & for \quad r < \sigma \\ 0 & for \quad r > \sigma \end{cases} \tag{3.1}$$

r is the distance between the spheres and σ is the diameter of the sphere. Since the potential can either be 0 or infinity only, the Boltzmann Factor $exp(-\beta U)$ is either 0 or 1 and the partition function is independent of temperature. Therefore the hard sphere system can be described by a parameter that depends only on the volume of the spheres and how that relates to the box volume.

The earliest computational work that was done on the hard sphere problem was done by Rosenbluth in 1954. He calculated the equation of state for a system of 256 $3D$ hard spheres using Monte Carlo methods that he helped develop with Nicholas Metropolis and others the year before. [111] [80]

Furthermore to quantify how the position of hard spheres deviate from those of an ideal gas, the radial distribution function $g(r)$ was examined in Fig 3.1. In units of V/V_0 where $V_0 = N\frac{\pi}{6}\sigma^3/\phi_c p$ and $\phi_c p$ is the volume at close packing, it was found that for V/V_0=1.8 $g(r)$ had the smeared out indistinct features of a liquid. Whereas for V/V_0=1.145 a much more dense system, the resulting $g(r)$ showed the distinct and regular shape of a crystalline solid. This study provided evidence that already particle volume provides a level of complexity that is manifested in the necessary existence of a phase transition in a system of hard spheres.

In 1957 Alder and Wainwright performed a Molecular dynamics simulation on a system of hard spheres. It was found that the hard sphere system exhibits two distinct phases at different ranges of volume fraction, ϕ. Since the hard-core potential includes solely a repulsive part, phase transitions in the system are the result of entropy. For $\phi < 0.494$ a system of hard spheres will behave as a stable fluid. For $\phi > 0.545$ the system will arrange themselves into an FCC lattice. Values of volume fraction in between these points correspond to metastable regions of two phase coexistence between the liquid and crystal. [5] Note that the close packed volume fraction for a $3-D$ system of hard spheres is 0.74. Alder and Wainwright showed

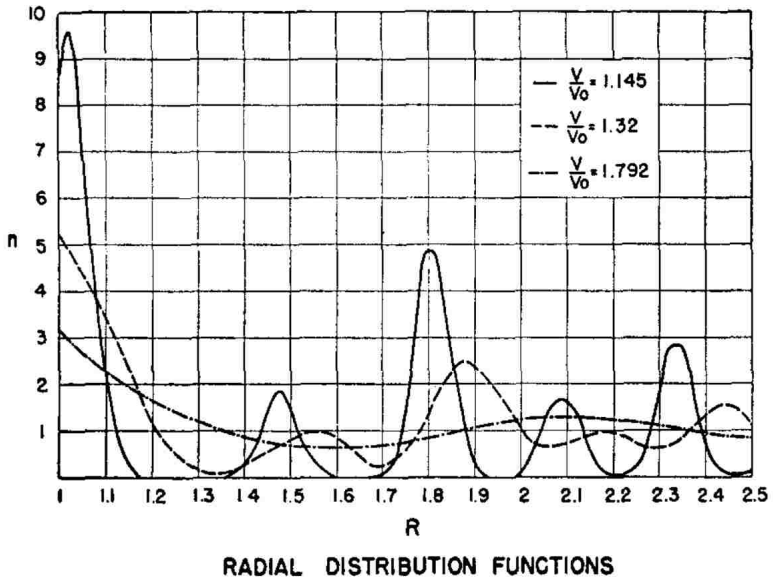

Figure 3.1: Radial distribution function $g(r)$ from [111] for various simulated densities in units of R particle diameter vs n the density of particles surrounding a given particle. As the value of V/V_0 increases system size increases thereby decreasing system density.

that for values of volume fraction well below close packing the system crystallizes. The well accepted phase diagram of packing fraction vs pressure for the hard sphere system is shown in Fig 3.2. [83]

3.1.2 Hard Ellipsoids

The hard-sphere problem can be thought of as a special and distinct case of a more general hard ellipsoid problem. In general the triaxial ellipsoid is defined in cartesian coordinates as

$$\frac{x^2}{a^2} + \frac{y^2}{b^2} + \frac{z^2}{c^2} = 1 \tag{3.2}$$

a, b and c define the axis lengths of the ellipsoid. For a sphere $a = b = c$. For the rest of this chapter the ellipsoids discussed are ellipsoids of revolution in which

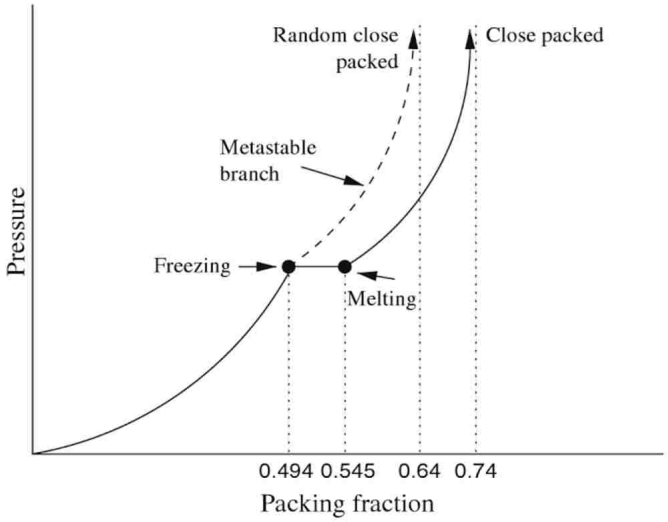

Figure 3.2: Accepted phase diagram of hard for the hard sphere system. For $\phi < 0.494$ hard spheres exist in the fluid phase. For $\phi > 0.545$ the system crytallizes, well below close packing at $phi = 0.74$ [83]

two of three axes are equal, typically $a = b \neq c$.

The aspect ratio ϵ, a ratio of the length of the symmetry axis and the length of any perpendicular axis for a sphere is 1. $\epsilon = \frac{c}{a}$. For oblate (disk-like) ellipsoids, $\epsilon < 1$. For prolate (lemon like) ellipsoids $\epsilon > 1$.

Like the hard-sphere problem, entropy drives phase transitions in systems of hard ellipsoids. In 1949 Onsager studied hard spherocylinders, which are cylinders with length L and diameter D and hemisphere caps at both ends. In particular Onsager investigated the behavior of spherocylinders with $L >> D$. He showed that these particles also undergo an entropy driven phase transition from an isotropic fluid to anisotropic phases. [93]

The entropy that underlies Onsagers phase transitions are of two competing types, translational entropy and orientational entropy. In a gas of hard rods, particles have both high translational entropy and orientational entropy. There is a lot of room for particles to move around and be oriented in any direction. However with

increasing particle density, particle orientational entropy is sacrificed for increasing translational entropy. This is an isotropic to nematic phase transition. In an isotropic phase, particles are without translational or orientational order. Particles with an average orientational order, but no translational order are said to be in a nematic phase. This phase transition occurs because in a system of rods, aligning the rods in some direction, decreases the overall excluded volume of the system, thus increasing the translational entropy. [38]

For a very dense system of rods, particles lack both orientational and translational entropy and crystallize into some sort of lattice. For densities in between a gas phase and a crystalline solid phase, the competition between the two entropies underpins the phase transitions that occur.

Although Onsagers original study was on spherocylinders, similar arguments can be made for the case of hard-ellipsoids with very large $\epsilon >> 1$ so called hard needles and can also be considered a special limiting case of the hard ellipsoids problem. To see this, it can be shown that in limit of $L >> D$ Onsager's infinitely long rods have excluded volume $V_{excl} = L^2 D\,|sin(\theta)|$ where θ is the angle between the rods. Similarly it can be shown that for the infinitely long needles, their excluded volume is $V_{excl} = 4\pi a^2 b\,|sin(\theta)|$. Again θ is the angle between adjacent needles. Comparing these expressions for excluded volume, one can simply substitute $4\pi a^2 b$ for $L^2 D$ and apply the known results from Onsager's model to to the hard ellipsoids in the limit of very long length. [9]

Frenkel and Mulder

For aspect ratios between these two cases, however, phase behavior was not well known until the work of Frenkel and Mulder.[42][41] In a series of seminal papers from 1984 and 1985, Frenkel and Mulder used computer simulation, specifically, constant-pressure Monte Carlo to characterize the phase behavior of both oblate ($\epsilon < 1$) and prolate ellipsoids ($\epsilon > 1$) for the range of aspect ratios between $\approx \frac{1}{3}$ and ≈ 3. In their simulation study they used a system of approximately 100 particles that were initially set on a FCC lattice. This lattice was allowed to melt and rearrange

under various conditions until equilibrium was reached in about 10^3 steps. Another 10^4 configuration steps were averaged to get equilibrium statistics.

At the time of their work, it was known that for infinitely thin oblate spheroids with $\epsilon \to 0$ at the freezing transition, the volume fraction $\phi = O(1)$. [41] Similar knowledge was not known for $\epsilon \to \infty$. However the equilvalent volume fraction values for spheres was known, $\phi = 0.545$, as above.[5] So it was assumed that even though the transition points depend on particle shape, for finite ϵ, volume fraction ϕ at the transition between isotropic to nematic phase and nematic to crystal would also be finite.

Furthermore, at close packing, hard-spheres assume an FCC structure. For hard ellipsoids, Frenkel and Mulder knew that the crystal structure at close packing was likely different, but they presumed at a simple compression or expansion of the FCC into a stretched FCC lattice would be sufficient to closely pack hard ellipsoids.

Frenkel and Mulder also calculated the coexistence densities of their phases by finding the free energy using thermodyanmic integration techniques, orientationally-averaged pair distribution function, the short range second rank order parameter and for the solid phases, the structure factor.

Compiling their work into a phase diagram of aspect ratio vs volume fraction, they identified four distinct phases: a isotropic phase, a nematic phase, a solid phase and, a plastic solid phase. Their phase diagram is shown below in Fig. 3.3. Notice that for semi-spherical particles, there is no change from isotropic to nematic phase, but there is a transition from an isotropic to plastic solid phase. Only with sufficient anistropy, aspect ratio less than $\frac{1}{2}$ or greater than 2 is a nematic phase observed. [42]

Frenkel and Mulder also noticed that they saw a striking symmetry appear in the phase diagram of oblate and prolate particles. They reasoned that this is logical for semi-spheres with aspect ratios near 1 and at low densities because the lower order virial coefficients are the same. However since knowledge of Onsagers work on high aspect ratio hard rods and very low aspect ratio hard platelets was known at the time, they knew that this symmetry was only approximate.

In furtherance of Frenkel and Mulders work in 1984, Allen et al. also studied

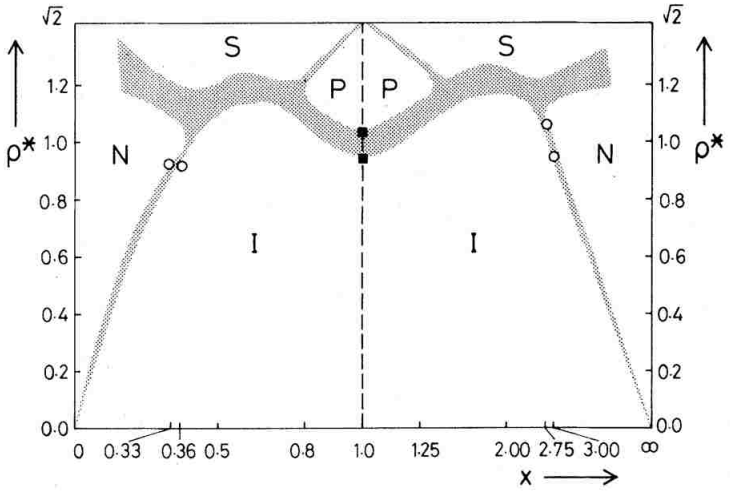

Figure 3.3: Monte Carlo simulation results for the phase diagram of Hard Ellipsoids of Revolution for both oblate and prolate shapes done by Frenkel and Mulder. [42]

hard ellipsoids in 1996 with even greater aspect ratios. Their interest focused particularly on the isotropic to nematic phase transition, in which particles lose their orientational randomness and being to align without translational order. [22]

Using the Gibbs-Duhem integration technique which find coexistence points as some parameter such as temperature is varied. This technique involves numerically solving a differential equation. They examined hard-prolate ellipsoids with aspect ratios in the range of 5 to 20.

Their simulation studies showed that as the particle shape become more and more elongated, the isotropic to nematic transition shifts to lower and lower densities. This result follows from the arguments made before that as a particle comes less and less spherical, the excluded volume of the particle is greater at higher densities unless the particles adopt some alignment.

Revisiting the Hard Ellipsoid

In 2012, Odriozola et al reexamined the phase transition of hard ellipsoids. [92] The motivation for doing this was two fold. At the time of the study, a family of new crystal structures, called SM2 were found. The SM2 unit cell is monoclinic with three unequal axes and one at a right angle to the other two and with particles at different orientations to each other. This structure appeared to have a lower free energy and ϕ than the stretched FCC that Frenkel and Mulder assumed. [35] [128] [104] This brought into question the original transition points. Reexamining the hard ellipsoids therefore would mean relocating the phase transitions and determining if the SM2 structure was the true equilibrium structure of a solid of hard ellipsoids.

Although it was not a part of the original motivation, since the Frenkel and Mulder's work, advances in finding an appoximation to the exact overlap distance between adjacent ellipoids with some eccentricity had been made. Originally Frenekl and Mulder's work relied upon the earlier work of Viellard-Baron who originally used spherocylinders to approximate the overlap distance between two adjacent ellipsoids. [134]At the time of their paper in 1984, Frenkel and Mulder already acknowledged the short-comings of is approximation and noted the work of Perram et al as more accurate. [41]

Since then a modification by Rickayzen to the Gaussian overlap model that approximates ellipsoid overlaps was proposed. This model adds a term to the the original such that two ellipsoids colliding in the shape of a T could be modeled correctly. The resulting expression for the closest approach between two ellipsoids called the Rickayzen Berne and Pechukas model was used and is shown below. [108]

$$\sigma_{RBP} = \sigma_{\perp}\left(1 - \frac{1}{2}\chi\left[A^{+} + A^{-}\right] + (1-\chi)\,\chi\prime\left[A^{+}A^{-}\right]\right)^{\frac{1}{2}} \tag{3.3}$$

$$A\pm = \frac{(\hat{r}\cdot\hat{u_i} \pm \hat{r}\cdot\hat{u_j})^2}{1 + \chi\hat{u_i}\cdot\hat{u_j}}$$

$$\chi = \frac{\epsilon^2 - 1}{\epsilon^2 + 1}$$

$$\chi\prime = \left(\frac{\epsilon - 1}{\epsilon + 1}\right)^2$$

Here $\hat{r}$ is the distance between particles and $\hat{u}_i$ is a normal vector pointing along the axis of symmetry of particle i.

As a brief aside, in 1992, Monte Carlo simulations done by Zarragoichoechea et al showed that a system of 256 prolate ellipsoids with $\epsilon = 3$ did not transition into a nematic phase at values of ϕ reported by Frenkel and Mulder. Their particles were also put on an FCC lattice and statistics calculated over similar Monte Carlo steps. In their paper they also studied a second system with 108 particles and found transition points in agreement with Frenkel and Mulder, suggesting that there might be some sort of density dependence in the original hard core results. [146]

Odriozola's method therefore included 100 particles.

The study also employed a replica-exchange Monte Carlo in the NPT ensemble. The advantage of the replica exchange method is that by running simulations simultaneously at different pressures and periodically swapping configurations, the system can more efficiently sample high density regions of the phase diagram to reach equilibiurm and do so without imposing some crystal structure a priori. [50] [91]

The replica exchange method uses an extended ensemble with replicas of varying pressure.

$$Q_{extend} = \prod_{i=1}^{n_r} Q_{NTP_i} \tag{3.4}$$

n_r the number of replicas =64 and Q_{NTP_i} is the partition function of the ith ensemble/replica and P_i is it's pressure. Particles are initially placed in the simulation box at random locations and with random orientations. Swaps are periodically made between adjacent replicas.

Simulations ran for $2X10^{13}$ trial moves to get to equilibrium with another $2X10^{13}$ steps for sampling.

Various methods were used to determine phase transition points: dimensionless pressure defined $Z = \frac{\beta P}{\rho}$, the isothermal compressibility $\chi = N\left(\langle\rho^2\rangle - \langle\rho\rangle^2\right) / \langle\rho\rangle^2$.

The order parameter $Q_6 = \left(\frac{4\pi}{13}\sum_{m=-6}^{m=6}\left|\langle Y_{6m}(\theta,\phi)\rangle^2\right|\right)^{1/2}$, where $Y_{6m}(\theta,\phi)$ is the ensemble average over all bonds of spherical harmonics of polar angles θ and ϕ. Q_6 is a measure of positional order and is 0 for random order and nonzero for configurations that have positional order. The orientational order parameter $P_2(r) = \left\langle \frac{1}{2}\left(3\left(\hat{u_i}\cdot\hat{u_j}\right)-1\right)\right\rangle$ is zero for random particle orientations and nonzero if particles adopt some alignment. [92]

For semi-spherical particles with longer axis up to 1.3 times the shorter axis for both oblates $\epsilon \simeq 0.769$ and prolates $\epsilon = 1.3$ as density and pressure increase, the system is epxcted to behave similarly to the hard sphere case with a transition from an isotropic to plastic solid. The point at which this transition occurs appears via a jump in a graph of the dimensionless pressure Z versus volume fraction ϕ. Additionally χ is expected to diverge at the thermodynamic limit. Plots of χ vs ϕ also shows a marked peak. Together these metrics indicate that the system underwent some first order phase transition. The change in Q_6 from zero to non-zero but only small change in $P_2(r)$ indicate that the transition was from a isotropic fluid to a ordered solid. At even higher pressures, orientational order does develop. Snapshots of the solid regions reveal that the transition in the solid phase is between a plastic-solid and an FCC-like crystal.

The point at which these transitions occurred depended on shape, and for increasing anisotropy away from the hard sphere shape, the value of ϕ would shift to the right. Indicating that for both oblates and prolates particles with more anisotropic shape underwent transitions more readily.

For oblates with higher anisotropy up to particles with long axis twice as large as the symmetry axis $\epsilon = 0.5$, there appears to be a reluctance to crystallize, although the crystal state is eventually found. For particles with $\epsilon = 0.5$ at $\phi \approx 0.634$ an isotropic to nematic transition starts to appear in which there is no appreciable change in Q_6 but $P_2(r)$ is nonzero.

For prolates with ϵ up to 2, the results are inconclusive, neither Z or χ indicate a transition. For $\epsilon > 2$ symmetric behavior to the oblates was found with the emergence of an isotropic to nematic phase transition occurring at $\phi \approx 0.64$.

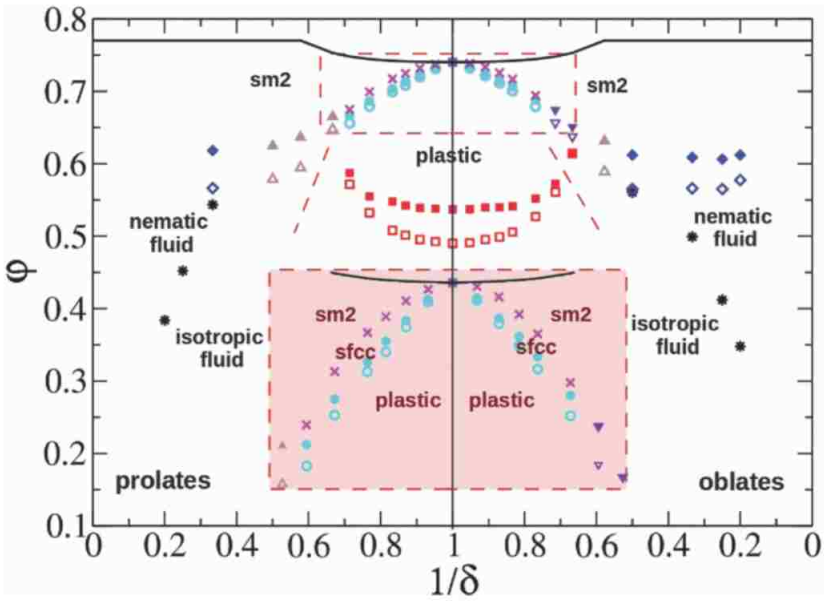

Figure 3.4: Phase diagram for oblate and prolate hard ellipsoids aspect ratio vs volume fraction from simulation results performed by Odriozola et al. on hard ellipsoids of revolution. [13]

In general for cases of the long axis being greater than 2 (both oblate and prolate) up to 5, at low pressure a system of particles would exist in the isotropic phase, increasing pressure the system would undergo a transition to a nematic phase and eventually crystallize. Visual inspection of the crystal phase reveals that it does have SM2 structure. The point at which these transitions occurred depended on the shape of the particles, with more anisotropic particles undergoing transitions at lower pressures and densities. Less anisotropic particles need to undergo additional solid-solid transitions to get to the highest ϕ SM2 configuration.[104] [13]. Oblates transitions also occured at slightly lower densities than prolates, but the found transition points for both shapes and the overall symmetry of the ϵ vs ϕ phase diagram that Frenkel and Mulder originally noted remains. A depiction of the updated phase diagram is shown in Fig 3.4. [92]

3.2 Attractive Potentials

Thus far, the phases discussed that were found at various packing fractions ϕ of hard-core particles exhibited behavior that could be characterized by the degree of order: no order for the isotropic phase, orientational order for a nematic phase, and both positional and orientational order for a solid phase. To get a richer variety of phase behavior particles need to have both attractive and repulsive properties. Furthermore until now, the intensive variable that was varied to achieve different values of ϕ was the pressure. The addition of an attractive component to the potential also add complexity by introducing the role of temperature.

3.2.1 The Square Well Potential

The most simple inter-molecular potential that encompasses both a repulsive and attractive part is the square well-potential defined:

$$U(r) = \begin{cases} \infty & for \quad r < \sigma \\ -U_0 & for \quad \sigma \leq r < \lambda\sigma \\ 0 & for \quad r \geq \lambda\sigma \end{cases} \tag{3.5}$$

r is the center-to-center distance between particles, σ is the particle diameter, λ is the range of the square-well attraction in units of σ and U_0 is the well-depth, a measure of the attractiveness of the interaction. The reduced temperature in a Monte Carlo simulation is given in units relating to the well-depth U_0. Particles are attractive if they are within a certain distance from one another, but if the distance is too small particles repel each other with a hard-core.

Note that the value σ is exact, but in the Rickayzen Berne and Pechukas equation σ is an approximation. Therefore, in ellipsoidal particle models that use this approximation, the square-well potential can only really be a quasi-square-well. Nevertheless, for the rest of this work, when referring to a square-well potential with ellipsoidal particles, the quasi aspect is assumed.

The square-well model is often used in computer simulations since it has numerous advantages. First the model is idealized so it it simple to implement. Square

wells are also unambiguous with respect to the number contact particles because of their sharp potential cutoffs. [133] The exhibited behavior of particles with square-well potentials depends on both the range of interaction and the well-depth.

Using a Monte Carlo simulation, Vega et al looked at a the range of interaction between isotropic particles for a simple square well spanning 1.25λ to 2λ. The group found liquid-liquid phase transitions whose order parameter is the absolute value of densities of the liquids. The critical points for these phase transitions and the shape of the coexistence curves in the phase diagram depended on this range of interaction. For 1.25λ ,1.375λ, 1.5λ and 1.75λ the shape of the coexistence curves were most closely approximated as cubic, as expected by their critical exponents. However for 2λ, the longest tested interaction range, the shape of the coexistence curve was quadratic.[133]

Smaller ranges of interaction were investigated by Pagan and Gunton, who looked at 1.15λ and 1.25λ The liquid/liquid coexistence line had already been well characterized for $\geq 1.25\lambda$.[94]

In 1996 Asherie et al. additionally showed that interaction range, along with well-depth and number of contact particles can also affect the order of phases that appear as one systematically lowers the temperature in a colloidal solution. For most fluids that undergo cooling, gas followed by liquid followed by solid is the normal order of phase transformation. However for colloids, a solution can go from gas to solid without ever passing through a liquid state. The group attributed this to requirements for metastability that included the range of interaction.[8]

Clearly range and well-depth of interaction is a means to affect the phase behavior of systems.

There are other attractive type potentials that also include repulsive terms, most notably the Lennard-Jones potential, but the focus here will be on models that use the simple square-well potential.

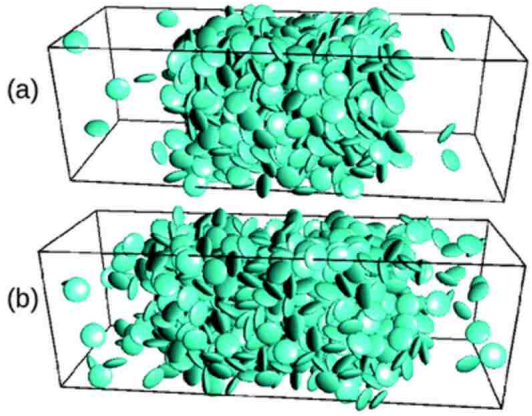

Figure 3.5: Snapshot of slab method used in [79]. Oblate particles are placed in the center of the slab. After some simulation time, particles move outward and phase coexistence is calculated.

3.2.2 Attractive Hard Ellipsoids

Following his groups work on Hard Ellipsoids, Odriozola et al turned their attention to attractive hard ellipsoids with an attractive square well potential. He first looked at just oblate ellipsoids with a short range attraction given by $\lambda = 0.25$ in units of the shorter particle axis. Using Monte Carlo techniques and van der Waals type perturbation theory, the group investigated the phase behavior that depended on both temperature T, volume fraction ϕ and aspect ratio ϵ. [79]

Briefly, the slab method of Monte Carlo simulation was used which is a means of investigating vapor-liquid coexistence. A $3D$ simulation box that has the length of 3 cubes put together is filled with particles in the middle cube. There is no barrier between the 3 cubes. The two side cubes are empty. Monte Carlo steps progress as particles move randomly from the center out to the sides. At equilibrium the center of the simulation box gives the particle rich liquid phase and the two adjacent boxes are the particle poor vapor phase. Between each phase is an interface.

One of the results of simulation under various conditions was that the critical volume fraction ϕ_c, that is the volume fraction for which $\phi < \phi_c$ vapor and liquid

phases separate and for $\phi > \phi_c$ is a homogeneous solution, was non-monotonic with increasing aspect ratio.

For semi-spherical particles with elongation axis $k < 1.3$ (and symmetry axis =1), ϕ_c was found to increase. For particles with elongation axis $k > 1.5$, ϕ_c decreased with increasing aspect ratio. For values of ϕ_c in between a plateau was observed.

The non-monotonic behavior can be understood as a competition between energy and entropy effects. For semi-spherical particles, as k increases, the relative square-well range decreases. So particles need to be closer to one another to feel each other's attractive potential. Therefore ϕ_c increases. However as k increases, the excluded volume per particle also increases, thereby increasing the inter-particle distance. Apparently for small k semi-spheres, the square-well energy effect is dominant, but beyond a certain aspect ratio, the excluded volume entropy effect is dominant.

Since hard-ellipsoids with square well attractions have been known to form smetic liquid crystals, the isotropic to nematic phase transition was also examined using the perturbation theory, which approximates the free energy with a contribution from a Parsons-Lee term for anisotropic hard particles (including both a radial and orientational part) as well as an attractive term via the second virial coefficient for a square well potential.

Results showed that isotropic to nematic transition occurs at higher densities than in a hard-oblate ellipsoid case. Reasoning that particles with an attractive potential would want to maximize the number of bonds with other particles, orientational ordering (i.e. parallel particle orientation) is not the most favorable for high particle contact. Thus when the square well attraction is stronger, such as in the case of lower temperature, a liquid phase or even vapor-liquid favored.

The prolate case was examined subsequently as well as an expanded square-well range from $\lambda = 0.25$ to $\lambda = 1$ in units of the short ellipsoid diameter. Since it is well known for spheres that the range of a square-well affects the resultant phase behavior, it was demonstrated that the same is true for ellipsoids of both prolate and oblate shape. Plots of the critical temperature T_c for a liquid-vapor phase separation vs elongation k show that for both prolate and oblate ellipsoids the longest studied range $\lambda = 1$ had the highest T_c. $\lambda = 0.25$ had the lowest T_c with λ ranges in between

following the same order. [131]

Particles with a longer interaction range, can more easily interact with each other and form bonds and undergo a particle dense and particle poor phase transition. A higher temperature is required to break those bonds.

The observed result of varying square-well range is as predicted. Furthermore, as in the case of oblates, in general, for greater elongation, particle shape decreases ϕ_c.

The istropic/nematic transition for prolates was also examined using many previously mentioned metrics, Z the reduced pressure, χ the isothermal compressibility and $P_2(r)$ the order parameter for orientational order. Additional metrics used were $P_4(r)$ the second order orientational order parameter, $< u >$ the average energy per particle, and $< m >$ the average cluster size.

These first first five metrics were a way of determining the transition point for the isotropic to nematic transition. Note that as in the oblate case the competition between energy and entropy, wanting to maximize bonds and wanting to keep excluded volume low, determines phase behavior. The nematic transition is destabilized by the attractive potential and using configuration snapshots, special structures were observed: aggregates that for oblates appeared cubatic and for prolates star-shaped.

These special structures, were characterized by the final metric, the $< m >$ the average cluster size. Again the role of temperature is important because at relatively high T, aggregate shapes were not observed. Only at low T (strong attraction) were clusters possible.

Phase diagrams depicting the studied vapor liquid and isotropic/nematic phases for both oblates and prolates is shown in Fig. 3.6 [131]

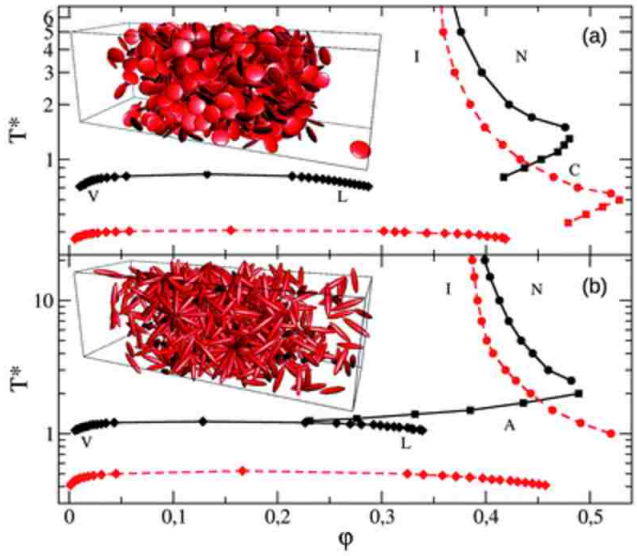

Figure 3.6: Phase diagram for attractive square-well hard ellipsoids from [131]. Liquid-vapor coexistence curve is shown (denoted by V, L) as well as isotropic/nematic phase curve (denoted by I, N). Red curve shows short range interaction with $\lambda = 0.25$, black curve shows long range interaction with $\lambda = 1$. Aggregate phase in the prolate phase diagram is denoted by A.

3.3 Valence and Patchiness

Controlling directionality of particle interactions is another means of adding diversity to the behavior of a system of ellipsoidal particles. Atoms and molecules already control the directionality of their interactions via valence electrons. So a similar concept can be used for larger particles.

3.3.1 Directional Spheres

One way of adding directional interactions to a particle is to only apply an attractive potential to only part of the particle. In the most simple cases some fraction of the particle interacts with its neighbors as a hard body and the other fraction of the particle interacts as a hard-body with an additional attractive potential. Particles

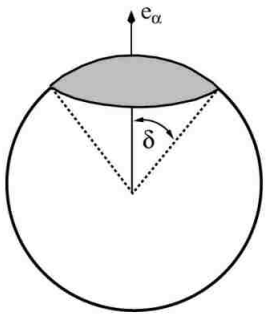

Figure 3.7: Illustration of directional hard sphere proposed by Kern and Frenkel with attractive patch and associated patch vector [60]

with regions of different physical properties are called patchy particles with the region of particle surface area that carries the attractive potential known as an attractive patch. In the parlance of colloidal particles, the concept of valence is used to describe the number of patches on a particle.

The special case of a particle with only one patch such that the particle has two different properties: repulsive and attractive is known as a Janus particle. (Typically Janus particle surface area is equally divided between repulsive and attractive potentials).

As always, when adding complexity to a model it is easiest to start with the case of spheres. Kern and Frenkel proposed a computationally simple, but effective means of applying directional patchiness to hard spheres. [60]In their model, a hard sphere with diameter σ has attractive square well patches. The percentage of total surface area of a particle that is covered by its patches is defined by parameter $\chi = n \cdot \sin^2(\theta/2)$ where n is the number of patches and δ is the half angle that subtends any particular patch. It is assumed in the model that all patches are of the same size. This equation for χ can be found via simple surface integration of a sphere.

The intermolecular potential between any two Kern and Frenkel model spheres is given by

$$U_{ij}\left(r_{ij},\hat{u}_i,\hat{u}_j\right)=U_{ij}\left(r_{ij}\right)f\left(\hat{u}_i,\hat{u}_j\right), \tag{3.6}$$

$U_{ij}(r_{ij}$ is the radial part of the potential that accounts for inter-particle distance r between particles i and j is the same as before in equation 3.5. $f\left(\hat{u}_i,\hat{u}_j\right)$ is an orientationally dependent part that depends on how particles aligned.

where U_0 is the well depth.

$$f(\hat{u}_i,\hat{u}_j)=\begin{cases}1,\hat{u}_i\cdot\hat{r}_{ij}\leq\cos\delta \quad \text{and } \hat{u}_j\cdot\hat{r}_{ji}\leq\cos\delta\\ 0,\text{otherwise}\end{cases} \tag{3.7}$$

$\hat{u}_i$ is a normal vector that points outward from a patch on particle i. $\hat{u}_j$ is a normal vector that points outwards from a patch on particle j.

In their original paper, Kern and Frenkel studied the liquid-liquid phase separation of spheres with various patch numbers and coverages. Liquid-vapor phase coexistence curves are shown in Figure 3.8. They found that both changing the number of surfaces patches as well as the total patch coverage χ affected the location of the phase transition points. In general, holding n constant, greater χ shifted phase transition points to higher temperatures. Greater χ implied that the particles were more attractive and more likely to bond even as increasing temperatures diminished the attraction between them. Similarly holding χ constant, greater n also shifted transition points to higher temperatures which is likely the result of multiple particle bonds being more easily accessible with more patches. It was later shown that resultant liquid-vapor phase curves for these systems of varying n could not be scaled according to a law of corresponding states. [19]

This simple but powerful model has been the basis for many other studies on spheres with directional interaction. For example Sciortino et al performed a numerical study on the liquid-vapor phase diagram of one-patch spheres with coverages between $\chi=1$, isotropic attractive particles down to the Janus case, $\chi=0.5$. The studied range of interaction was $\lambda=0.5\sigma$. [118] Like Kern and Frenkel, it was found that the critical temperature T_c of liquid-vapor transitions increased with χ. Additionally more interesting shapes emerged as temperature decreased. In the gas phase, orientationally ordered micelles and vesicles formed, in which the attractive

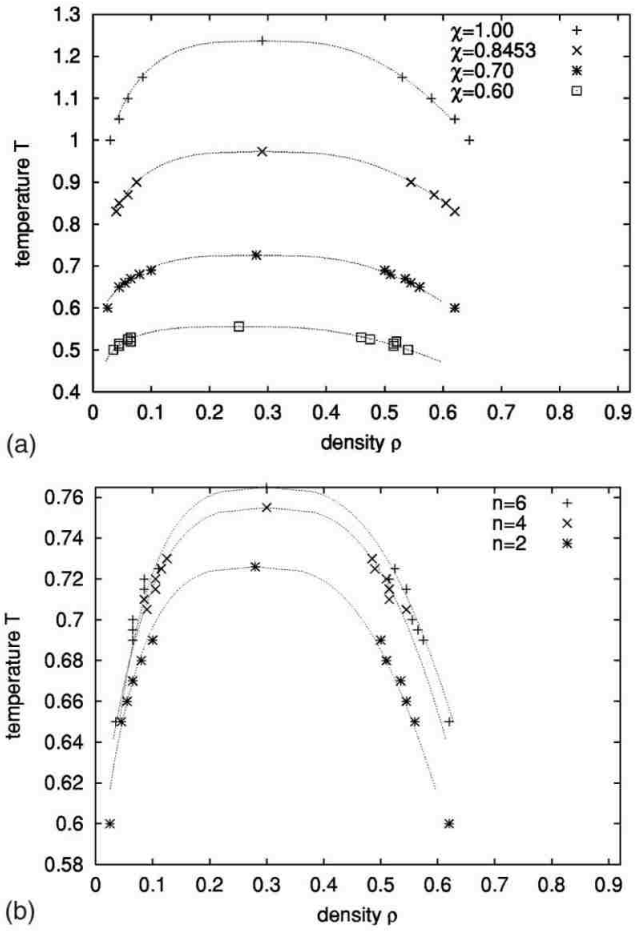

Figure 3.8: Liquid-Vapor phase coexistence curves for a fluid system of directional spheres with various values for total patch coverage χ and total patch number n. [60]

patches all turned in to face each other, exposing only the their repulsive surfaces. At sufficiently low temperatures, these micelles were shown to be very stable such that the system acted approximately as a fluid of micellar clusters interacting via excluded volume suppressing the liquid-vapor phase behavior.

Additionally the phase diagram of particles with Janus type coverage showed very anomalous behavior. In a plot of temperature vs density, the slope of the

liquid-vapor separation had a negative slope. Additionally, using the Claperyon equation $\frac{dP}{dT}$ was equated with $\frac{dS}{dV}$ and since Monte Carlo simulations were done in the NVT ensemble, the entropy of the liquid and vapor phases were accessed with the surprising results that the dense liquid phase had more entropy than the low density vapor. [119] The phase diagram is shown in Fig. 3.10(b).

Other studies have shown that this simple model on hard spheres can yield a vast array of behaviors. Small χ one patch particles for example have been shown to cluster into other special shapes such as wires and lamellae. [84] Empty liquids, liquids beneath the T_c critical point of liquid-vapor phase separation with vanishingly small packing fraction ϕ were reported and studied as well for the Kern and Frenkel model. [18]. Particles with various numbers of patches have been shown to undergo gelation. [113] [120] Together with many other studies, the complexity that arises from the addition of directionality to particle interaction is obvious.

3.3.2 Directional Ellipsoids

Although directionality was used in the last section on patchy spheres to discuss only about inter-particle potentials, the elongated ellipsoidal shape also inherently includes some concept of directionality. Combining these two concepts, interaction directionality and shape directionality, patchy ellipsoids hold the potential for an increasing display of complex behavior.

Studies on the self-assembly of Janus ellipsoids were done by Gunton et al who used the Kern and Frenkel model of patchy inter-particle directional potential and applied it to oblate and prolate ellipsoids by modifying the original potential. $U_{ij}\left(r_{ij}, \hat{u}_i, \hat{u}_j\right) = U_{ij}\left(r_{ij}\right) f\left(\hat{u}_i, \hat{u}_j\right)$. The radial part $U_{ij}(r_{ij})$ becomes more complicated with ellipsoidal shape since σ is not as easily calculated.

$$U_{ij}\left(r_{ij}\right) = \begin{cases} \infty, \text{ (if particles overlap)} \\ -U_0 H\left(\sigma_{ij} + 0.5\sigma - r_{ij}\right), \end{cases}$$

and where U_0 is the well depth, H(x) is the Heaviside function and σ represents the total length of the longer axis. The effective separation parameter, σ_{ij}, is the

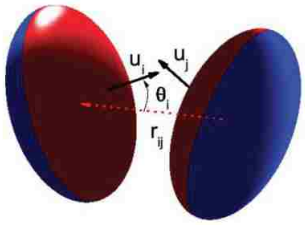

Figure 3.9: Illustration of two Janus oblate particles interacting. Attractive SW patches are shown in red and hard core repulive parts are shown in blue. [74]

approximate distance between the two spheroids, as obtained from the Gaussion overlap model of Pechukas and Berne [15], and is given by

$$\sigma_{ij} = 2b \left[1 - \frac{\alpha}{2} \left(\frac{\left(\hat{u}_i \cdot \hat{r}_{ij} + \hat{u}_j \cdot \hat{r}_{ij}\right)^2}{1 + \alpha \hat{u}_i \cdot \hat{u}_j} + \frac{\left(\hat{u}_i \cdot \hat{r}_{ij} - \hat{u}_j \cdot \hat{r}_{ij}\right)^2}{1 - \alpha \hat{u}_i \cdot \hat{u}_j} \right) \right]^{-1/2}, \tag{3.8}$$

where $\alpha = \left(\epsilon^2 - 1\right) / \left(\epsilon^2 + 1\right)$. This corresponds to an interaction range $\lambda = 1.5\sigma$.

The orientational part $f\left(\hat{u}_i, \hat{u}_j\right)$ is the same as in equation4.3, with $\delta = \frac{\pi}{2}$.

Motivated in part by the previous work that found micelle and vesicle clusters in Janus spheres,[118] [119] the goal of the work on Janus ellipsoids was to assess how changes in aspect ratio ϵ affected cluster morphology. Using standard NVT ensmeble Monte Carlo techniques, it was found that at low temperatures and low densities, systems of oblate Janus ellipsoids were found to form monomers, small oligomers, micelles and vesicles. Although Monte Carlo techniques are not able to explore the kinetic pathways of structure formation, sampling time does give an estimate of how long it takes to reach some structural configuration. In contrast to the Janus spheres, Janus ellipsoids were able to reach cluster configurations more quickly, but these clusters were less stable.

Also the distribution of the cluster size was affected by ϵ. Semi-spherical oblate were more likely to be found in a greater variety of cluster types with smaller probability for each type. Oblates with smaller ϵ, those that are more flattened, had clusters that were more uniform and in general were more likely to form larger clusters. Even bonds between just two particle bonds were also affected by increasing

ϵ with a similar behavior: semi-spherical particles were more likely to be oriented in a variety of positions, flatter disks, had stronger preference for inter-particle orientation.[74].

Prolate Janus ellipsoids too were found to self-assemble into various clustered morphologies. As ellipsoids became more elongated an progressive order of structures was found. For semi-spherical particles with $\epsilon < 1.2$ particles were found in vesicle bilayers. For $\epsilon \approx 1.3$ tubular micelles appeared. Increasing ϵ the length of the tubular micelle chain decreases above $\epsilon = 1.3$ until around $\epsilon = 1.7$ in which micelles start to dominate. Above $\epsilon = 2.0$ the micellar structure is stable and "star" shaped. In general higher ϵ, more elongated particles produced clusters with smaller cluster sizes and the distribution of particle orientations was more disperse for particles with greater elongation. [70].

These studies on Janus ellipsoids were done without knowledge of the phase diagram. Following the work on Janus spheres, simulations were done at low temperature and low density ($\rho = 0.037$ for Janus oblates and $\rho = 0.02$ for Janus prolates). So it was assumed by the authors that they were in the gas phase.

In a later study the phase diagram for one specific type of Janus ellipsoid was studied. Using an extended law of corresponding states from Noro and Frenkel,[90] the authors studied the liquid-vapor phase diagram for Janus oblate ellipsoids with $\epsilon = 0.6$ and short ranged well-width $\lambda = 0.2$. The method of Noro and Frenkel says that at the thermodynamics of a system does not depend upon details in the potential and instead depend only on the second-virial coefficient B_2 and the density. Therefore, by calculting B_2 for the spheroids and comparing it to the known value of B_2 for spheres obtained from earlier work by Sciortino et al., a procedure known as B_2 scaling, the authors came up with an estimate for the phase diagram. That phase diagram is shown in Fig. 3.10 (a) as well as that of Sciortino from his study of Janus spheres and is the only previously known phase diagram of ellipsoidal patchy particles.[115].

One final note, although the advances in creating a more and more complex model of ellipsoidal particles has been presented here as a linear progression from hard spheres, to hard ellipsoids, to attractive spheres then ellipsoids, and finally

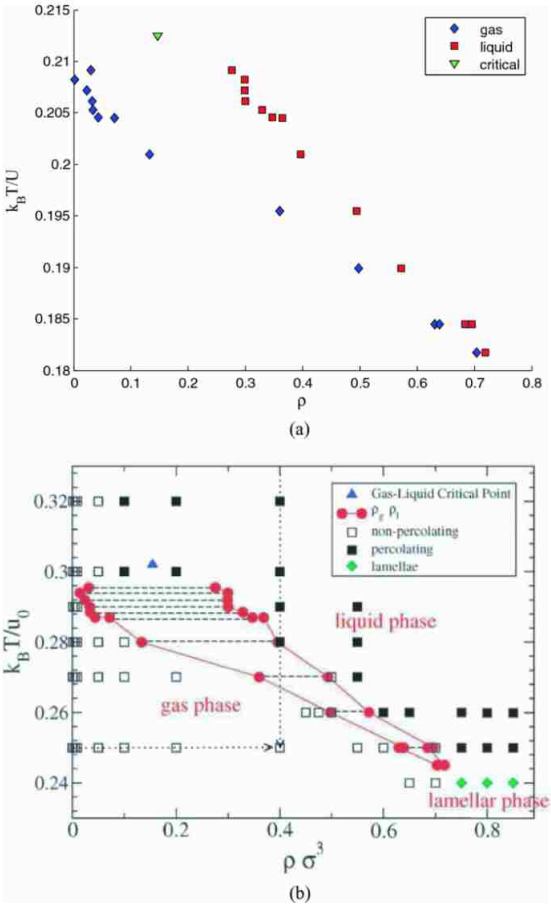

Figure 3.10: a) Phase Diagram of Janus oblate ellipsoids with $\epsilon = 0.6$ and $\lambda = 0.2$. [115] b) Phase diagram of Janus spheres with $\lambda = 0.5$. [119]

directionally attractive spheres and ellipsoids, in truth advances in one study informs the others. For example, after the empty liquid state was found and characterized for spheres with directional attraction, oblate ellipsoids were also studied to and found to exhibit empty liquid behavior. [79] [131] [132].

Also researchers continue to probe details of well-established problems. As shown above the hard ellipsoid problem was revisited in 2012 [92] [13]. Even the hard sphere problem is still being investigated. Packing fractions ϕ for randomly packed structures of both ellipsoids and spheres are still being investigated. [35] [34]. At the

time of this writing, it was recently shown that an equilibrium state fluid system of hard spheres can have the same density as a non equilibrium jammed stated indicating that the fluid branch of the phase diagram for hard spheres may extend further than originally thought. [16]

Additionally how these particles of different types interact with each other is another avenue of active research. The existence of micelles and vesicles in Janus particles makes them a good candidate for encapsulating agents. Gunton et al studied how a solution of Janus ellipsoids might be used to encapsulate isotropic spheres at various ratios of ellipsoid to sphere concentration and with varying inter-particle potential and elongated shaped. [71], [72].

Finally, the models, and particularly the square-well potential type discussed here are only a fraction of the many models and variations on the sphere/ellipsoid problem that exist and are currently being employed by researchers.

Chapter 4

Phase Diagram of Patchy Ellipsoidal Fluids

4.1 Introduction

The process of colloidal and protein self-assembly, which involves the aggregation of particles to form a range of morphologies, has attracted considerable attention owing to its potential in the fabrication of new materials [110] [147] [7] [144] [76] [143] and in the study of protein condensation[53]. Indeed, based on both experimental and simulation studies, several technologies that exploit self-assembly have been identified, including photonic crystals and drug delivery.[97][57][72] . Similar studies have been of great value in understanding how to grow high-quality protein crystals, an important step in the determination of protein structure and function. [53]

In recent years, it has been recognized that particle anisotropy in the form of orientationally-dependent interactions and varying particle shape is an important factor dictating the complexity of aggregate morphologies [47]. For this reason, various groups have developed techniques to manufacture colloids that have precisely controlled particle size, shape and interactions [143] [98] [117].

While our focus here is on colloidal systems, it should be noted that anisotropic

interactions play an important role in other systems as well. For example, protein-protein interactions are often anisotropic owing to the non-uniformity of distributed surface charges, the presence of hydrophobic/hydrophilic regions and the presence of hydrogen bonds[75] [54]. An understanding of the mechanism of protein aggregation is especially relevant since many diseases result from improper protein self-assembly, including cataracts [124] and neurological disorders such as Alzheimer's [121], Parkinson's and Huntington's disease [112]. Thus, the study of the role of anisotropy in *in vivo* protein self-assembly is of considerable interest.

Computer simulation is an important tool for the investigation of the energetics and dynamics of particle aggregation. Fully atomistic models are prohibitively expensive due to the required simulation time scales and the size of the conformational space. These models are too slow to map out phase diagrams and self-assembly of colloidal/protein solution. Coarse-grained models that simplify yet preserve many of the important characteristics are a tractable way to study collective behavior and reach the time and size that allow for comparison between computation and experiment. There exist many of these coarse-grained models that vary the amount of preserved detail. These coarse-grained models have been used extensively to study protein aggregation, crystallization, and folding. For more reviews we refer the reader to [87],[129],[89],[141], [64] [1],[11],[32],[81],[14],[55],[10].

Kern and Frenkel developed a simplified description of a colloidal system based upon hard spheres that are modified by surface patches [61]. The utility of this model becomes evident when one considers the remarkably diverse behavior that it exhibits. For example, one-patch particles having two chemically dissimilar hemi-surfaces (i.e., Janus particles) have been shown to spontaneously self-assemble into orientationally ordered micelles and vesicles [70][74]. Additionally decreasing the patch surface coverage in a one-patch system, particles were found to self-asemble into to wires and lamellae. [84]

However, despite the insights gained from this useful model, it cannot be employed to describe the effect of shape anisotropy on phase equilibrium, an important characteristic of many new and important functional colloids. The role of shape anisotropy in self-assembly cannot be overlooked since shape plays an important

role in particle packing and density and even ligand binding.[86] [58] (The situation may be analogous for proteins since these systems are often described by colloidal models.[61]) We note that recent Monte Carlo simulation studies of Janus ellipsoids have shown that the particle aspect ratio plays a significant role in determining the size and structure of aggregates [142]. For example, oblate Janus ellipsoids tend to form vesicle-like structures, whereas prolate Janus ellipsoids form ordered clusters that can become tubular micelles and micelles with increasing aspect ratio.[71] It should be noted, that other structures are also possible for the Janus ellipsoid system, including for example, fibers and ribbons. [130] [123] In extreme cases, such as systems comprising plate-like and rod-like particles, a range of behaviors is observed.[143] [117]. In particular, low-aspect-ratio oblate ellipsoids have been shown to have vanishing critical volume fraction and critical temperature with increasing anisotropy, whereas high-aspect-ratio prolate ellipsoids have been shown to have vanishing critical volume fraction (but not critical temperature) with increasing anisotropy.[79][132]

The above discussion suggests the importance of anisotropy in determining the equilibrium properties of self-assembled systems. Thus, in this paper, we examine quantitatively the impact of shape anisotropy and particle interaction energy on the phase behavior of a colloidal fluid comprising ellipsoidal particles, with an emphasis on critical behavior. More specifically, we employ Gibbs ensemble Monte Carlo [43][95] simulation to obtain the fluid-fluid equilibrium phase diagram of hard prolate ellipsoids having Kern-Frenkel surface patches under a variety of conditions. For concreteness, we consider particles of varying aspect ratios having the same volume, and having two or four polar patches of constant size. Finally, we examine the dependence of the critical temperature as a function of aspect ratio and patch area.

4.2 Simulation Methodology

4.2.1 Model

Consider a system comprising N prolate ellipsoidal (spheroidal) particles with semi-principal axes having lengths $a = b < c$ and patches distributed on their surfaces (see Fig. 1, panel I). The corresponding aspect ratio for these particles $\epsilon = \frac{c}{a}$. In this work, we consider particles with $\epsilon = 1.1 - 2$ such that the volume $V = (4/3)\,\pi a^3 \epsilon$ is held constant. It should be noted that the surface areas of the equi-volume ellipsoids are, in fact, a function of ϵ, as indicated below.

In our model, two spheroids, i and j, displaced by $\vec{r}_{ij} \equiv \vec{r}_i - \vec{r}_j$ and having patches with unit normals $\hat{u}_i$ and $\hat{u}_j$ interact via a "quasi-square-well" potential given by [71]

$$U_{ij}\left(r_{ij}, \hat{u}_i, \hat{u}_j\right) = U_{ij}\left(r_{ij}\right) f\left(\hat{u}_i, \hat{u}_j\right), \tag{4.1}$$

where the radial part of the potential is given by

$$U_{ij}\left(r_{ij}\right) = \begin{cases} \infty, \text{ (if particles overlap)} \\ -U_0 H\left(\sigma_{ij} + 0.5\sigma - r_{ij}\right), \end{cases}$$

and where U_0 is the well depth, H(x) is the Heaviside function and σ represents the total length of the c axis. The effective separation parameter, σ_{ij}, is the approximate distance between the two spheroids, as obtained from the Gaussion overlap model of Pechukas and Berne [15], and is given by

$$\sigma_{ij} = 2b \left[1 - \frac{\alpha}{2}\left(\frac{\left(\hat{u}_i \cdot \hat{r}_{ij} + \hat{u}_j \cdot \hat{r}_{ij}\right)^2}{1 + \alpha \hat{u}_i \cdot \hat{u}_j} + \frac{\left(\hat{u}_i \cdot \hat{r}_{ij} - \hat{u}_j \cdot \hat{r}_{ij}\right)^2}{1 - \alpha \hat{u}_i \cdot \hat{u}_j}\right)\right]^{-1/2}, \tag{4.2}$$

where $\alpha = \left(\epsilon^2 - 1\right) / \left(\epsilon^2 + 1\right)$. This corresponds to an interaction range $\lambda = 1.5\sigma$. As is customary, quantities will be reported in reduced units (i.e., in terms of U_0 and a).

The orientational $f\left(\hat{u}_i, \hat{u}_j\right)$ for two patches is given by

$$f(\hat{u}_i, \hat{u}_j) = \begin{cases} 1, \hat{u}_i \cdot \hat{r}_{ij} \leq \cos\delta \quad \text{and } \hat{u}_j \cdot \hat{r}_{ji} \leq \cos\delta \\ 0, \text{otherwise} \end{cases} \tag{4.3}$$

The generalization of this factor to the four-patch case is straightforward. Thus, particles interact if they are within the interaction range given by $U_{ij}(r_{ij})$, and if the dot product of the normals of the patch vectors $\hat{u}_i$, $\hat{u}_j$ and the vector $\vec{r_{ij}}$ between them is less than $\cos\delta$, where δ is the half-angle of the patch (i.e., the patches are facing each other).

The half-angle δ subtends the patch radius, as shown in Fig. 1 (panel II). It is convenient to define the ratio of the spheroidal patch area to the surface area of a corresponding sphere having the same volume as the spheroid, namely $\chi(\delta, \epsilon, V)$. χ therefore reflects the (normalized) total surface of a spheroid that is covered by patches and is given by

$$\chi(\delta, \epsilon, V) = \frac{S(\delta, \epsilon, V)}{S(\delta = \pi, \epsilon = 1, V)} \tag{4.4}$$

The total spheroidal surface area, corresponding to a patch half-angle $\delta = \pi$, is

$$S(\delta = \pi, \epsilon, V) = 2\pi \left(\frac{3V}{4\pi\epsilon}\right)^{2/3} \left[1 + \frac{\epsilon \sin^{-1}(e(\epsilon))}{e(\epsilon)}\right], \tag{4.5}$$

where $e^2(\epsilon) = 1 - \left(\frac{1}{\epsilon}\right)^2$. So, the total surface area of a sphere (i.e., for $\epsilon = 1$) is $S(\delta = \pi, \epsilon = 1, V) = 4\pi \left(\frac{3V}{4\pi}\right)^{2/3}$. In this instance $\delta = \pi$ corresponds to one hemisphere of the spheroid. So two times this value gives the total spheroid surface area. And $\epsilon = 1$ corresponds to the case of a sphere. It is worth noting that maintaining constant particle volume while increasing ϵ necessitates a small, but nontrivial, increase in total particle surface area. Thus, if patch sizes are held constant, fractional patch sizes would decrease slightly.

The patch area for each of two polar patches, $S(\delta, \epsilon, V)$, is given by the surface integral

$$S(\delta, \epsilon, V) = 2\pi \left(\frac{3V}{4\pi}\right)^{2/3} \epsilon \int_{u_{min}}^{1} du \sqrt{(1 - e(\epsilon) u^2)}, \tag{4.6}$$

where given a desired patch size, χ, u_{min} is related to the size of the patch as $u_{min} = (1/\epsilon) / \sqrt{\left(\tan^2\delta + (1/\epsilon)^2\right)}$. This integral can be evaluated to obtain

$$S(\delta, \epsilon, V) = 2\pi \left(\frac{3V}{8\pi}\right)^{2/3} \epsilon \left[\sqrt{1-e} - \sqrt{1 - e u_{min}} + \frac{\sin^{-1}(\sqrt{e})}{\sqrt{e}} - \frac{\sin^{-1}\left(\sqrt{e u_{min}}\right)}{\sqrt{e}}\right]. \tag{4.7}$$

Parameter	Definition
a, b, c	semi-principal axes, $a = b < c$
δ	half-angle that defines patch size
ϵ	aspect ratio, $\epsilon = \frac{c}{a}$
δ	half-angle that defines patch size
λ	interaction range, $\lambda = 1.5\sigma$
$\vec{r_{ij}}$	displacement vector between two particles
σ	total length of c axis
Tc	critical Temperature
$\vec{u_i}$, $\vec{u_j}$	vectors normal to the patch surfaces
u	average energy per particle
χ	total patch area/surface area of a sphere of equivalent volume

Table 4.1: Summary of the relevant parameters and their definitions

For equatorial patches, such as in the four-patch case,

$$S\left(\delta, \epsilon, V\right) = 2\pi \left(\frac{3V}{4\pi}\right)^{2/3} \epsilon \int_0^{\delta} d\theta \sin^2\theta \sqrt{1 + \frac{1}{\epsilon^2}\cot^2\theta}. \tag{4.8}$$

where θ is the standard polar angle.

Our aim is to describe the impact of patchiness on the phase behavior of spheroidal particles, with particular attention to the critical temperature.

4.2.2 Methodology

We employed both conventional Metropolis Monte Carlo (MC) and Gibbs ensemble Monte Carlo simulation [95] to investigate single fluid phase and fluid-fluid phase separation, respectively, in the aforementioned spheroid system. For the case of a single fluid phase simulations were performed at temperatures slightly below the critical the critical temperature T_c for a given aspect ratio ϵ and χ and at the relatively high number density $\rho = 0.62$. The purpose of these simulations was to determine the dependence of ensemble-averaged quantities, such as the internal

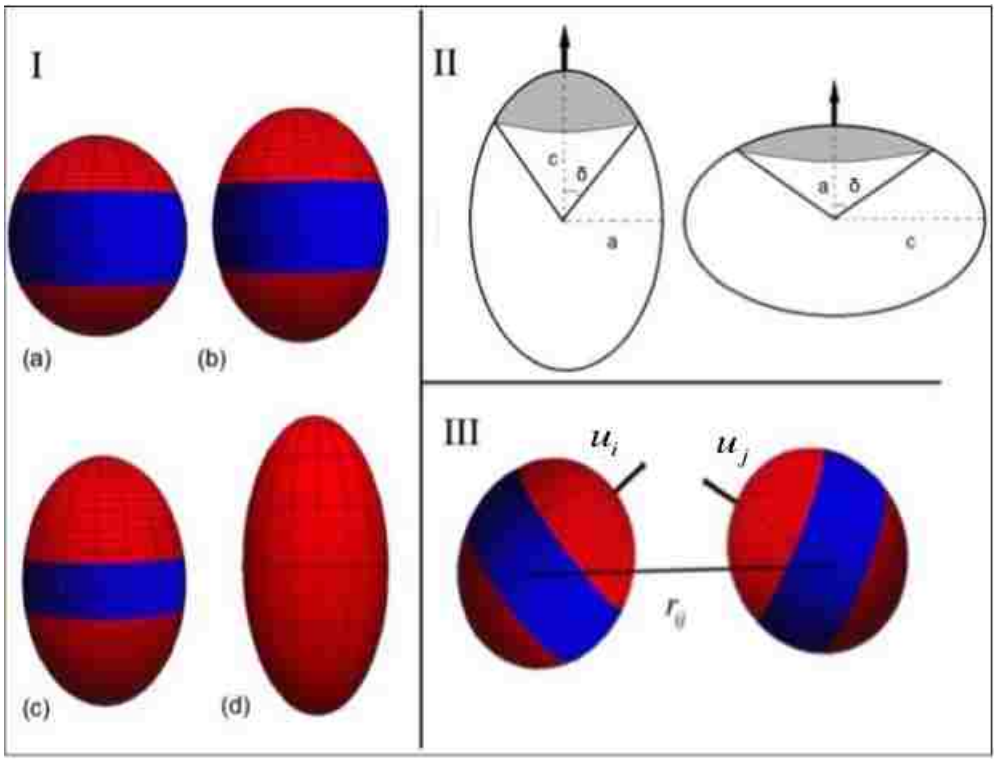

Figure 4.1: Panel 1 shows particles with various patch coverages and aspect ratios, namely (a) $\chi = 0.6$, $\epsilon = 1.1$, (b) $\chi = 0.7$, $\epsilon = 1.3$ (c) $\chi = 0.8453$, $\epsilon = 1.5$ (d)$\chi = 1$, $\epsilon = 2$. Panel 2 shows particles with semi-principal axes a and c. This panel also illustrates sample polar and equatorial patches. A patch is defined with solid angle δ. Panel 3 shows of two interacting particles with a center to center distance of r_{ij} and patch normals $\hat{u}_i$ and $\hat{u}_j$

energy per particle u, on ϵ. For the Gibbs ensemble simulation of phase coexistence with a selected χ and ϵ, $N = 256$ particles were randomly distributed in each of two simulation boxes such that the number density in each box $\rho = 0.3$. Each box individually was subject to periodic boundary conditions. A Monte Carlo step comprised N attempts to perform one of three possible particle moves in a randomly chosen box, namely: 1.) displacement within a box, 2.) displacement to another box, or 3.) change in orientation. In addition, the box size could also change. After each move attempt, the change in energy of the system was calculated. If the change in energy was less than or equal to zero, the move was accepted. Otherwise, the move

would be accepted with a probability proportional to the Boltzmann factor. As we are interested in phase coexistence, a starting temperature was selected based on what was found for the case of Kern and Frenkel spheres [61], and the fluid energies and densities in each box were monitored. If only a single phase was found, then the temperature was systematically lowered until coexistence was observed and the miscibility gap was mapped out.

It should be noted that this system typically requires relatively long equilibration times, with the largest values of ϵ requiring the longest times. In particular, in our studies roughly 5×10^5 Monte Carlo steps (MCS) were needed for equilibration of a $\epsilon = 1.1$ system, while approximately 2×10^6 MCS were necessary for $\epsilon = 2.0$ system. Density, energy and particle configuration data were sampled every 250 MCS and, to obtain statistically meaningful results, the data was averaged over 5 equivalent runs for a given ϵ, χ and temperature that differed only in the value of initial random seed.

Finally, once the coexistence curves are mapped, we estimate the critical temperature, T_c, and critical density, ρ_c, for a given miscibility gap using the law of rectilinear diameter [21]. This approximate method was employed here as small parameter changes resulted in large box volume fluctuations that precluded simulations too close to a critical point. More specifically, given the liquid and gas densities, ρ_{liq} and ρ_{gas}, respectively, one can determine the critical temperature and density by solving the coupled system of equations

$$(\rho_{liq} + \rho_{gas})/2 = \rho_c - A \cdot |T - T_c| \,, \tag{4.9}$$

$$(\rho_{liq} + \rho_{gas}) = B \cdot |T - T_c|^{0.32} \,, \tag{4.10}$$

where A and B are parameters to be determined based on a best fit to simulation data.

4.3 Results and Discussion

As stated above, our goal is to determine the effect of shape anisotropy on phase equilibrium for spheroidal particles. Recall, we employed an interaction range of $\lambda = 1.5$ as a prototype of long-ranged interactions that are characteristic of many experimental systems. The impact of both two-patch and four-patch geometries on phase behavior (i.e., patch valency) is also explored.

4.3.1 Particles with Two Patches

We first mapped the fluid-fluid coexistence curves as a function of aspect ratio, ϵ, by varying the simulation temperature. Consider the case of a system of interacting spheroids having two patches for which the spheroid volume, V, and the patch area fraction, χ, are held constant for any aspect ratio. The liquid-liquid miscibility gaps for this system for particles with $\epsilon = 1.1$ and 1.5 are displayed in Figs. 2a and b, respectively. In each figure, the bottom (top) curves depict the phase separation for particles with $\chi = 0.6$ ($\chi = 1.0$) patchy spheres. This ordering of the phase diagrams is expected since greater attractive patch coverage results in greater available surface area for bonding and implies that such liquids can coexist at higher temperatures. The locations of the critical points, $T_c(\epsilon, \chi)$, for each coexistence curve were estimated using the law of rectilinear diameter and are also indicated in the figures (with diamonds).

The impact of patchiness and anisotropy on phase transitions in this system are highlighted by examining the aforementioned critical points. The dependence of T_c on ϵ at fixed χ and particle volume, V, for several effective patch coverages, χ, is shown in Fig. 3. As is evident from the figure, T_c decreases roughly linearly with increasing ϵ. This linear dependence can be understood, at least in part, by examining the dependence of the energetics of this system on ϵ near T_c. For convenience, we focus on the internal energy of the system as an indicator of the strength of interparticle bonding. More specifically, to determine the dependence of the internal energy on on ϵ near the critical temperature, we performed Metropolis

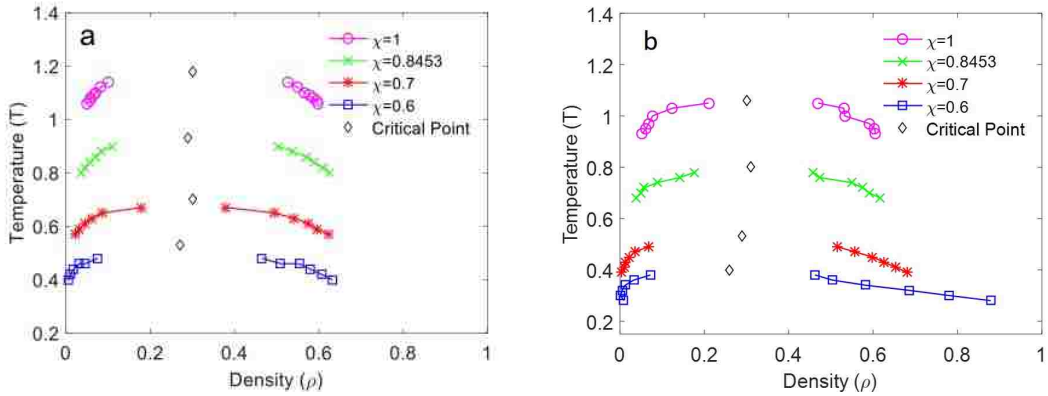

Figure 4.2: Examples of phase diagrams obtained using Gibbs Ensemble MC for particles with two patches and either $\epsilon = 1.1$ (a) or $\epsilon = 1.5$ (b). The patch area fraction, χ, is given in the legend. The $\diamond$ symbols denote estimates of critical temperatures, as obtained using the law of rectilinear diameter.

MC simulations of a dense fluid with $\rho = 0.62$ at temperatures just below the critical temperatures, as determined by the analysis above. Figure 4 shows a plot of the average energy per particle, $\langle u \rangle$, as a function of ϵ for coverages $\chi = 0.6 - 1.0$. As is evident from the figure, $\langle u \rangle \propto \epsilon$ for the various patch areas. This linear increase in $\langle u \rangle$ with ϵ implies a decreasing effective bond strength. Thus, as particles become more ellipsoidal, they are bonded, on average, more weakly with their neighbors and, therefore, one expects a concomitant (linear) decrease in T_c with increasing ϵ.

It is useful to examine the dependence of $T_c(\epsilon)$ on ϵ from a somewhat different perspective as well. We note that the observed behavior is dictated, at least in part, by several geometric factors. In particular, the critical temperature depends on the probability that a patch on a given particle subtends a patch on a neighboring particle. This probability is associated with the square of the solid angle, $\gamma(\epsilon, \chi)$, associated with each patch. Thus, from these considerations, one might expect that $T_c(\epsilon, \chi) / T_c(\epsilon = 1, \chi) \approx [\gamma(\epsilon, \chi) / \gamma(\epsilon = 1, \chi)]^2$. For a given χ, we obtain $\delta = \delta(\epsilon)$ using Eqs. 4.4 and 4.5 and then calculate numerically the corresponding γ for the two patches. Since δ is a decreasing function of ϵ, γ also decreases as ϵ increases.

The calculated values for $[\gamma(\epsilon, \chi) / \gamma(\epsilon = 1, \chi)]^2$ for $\chi = 0.7$ are shown in Fig. 5

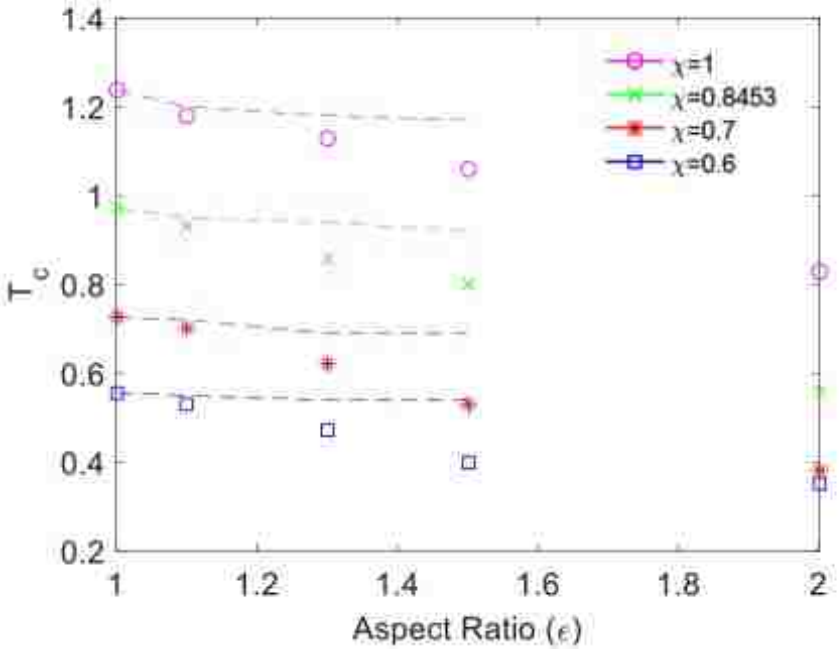

Figure 4.3: The critical temperature, T_c, versus aspect ratio, ϵ, for several values of the effective patch coverage, χ, including: $\chi = 0.6$ (blue squares), $\chi = 0.7$ (red asterisks), $\chi = 0.8453$ (green crosses), $\chi = 1$ (maroon circles). The dashed lines are estimates of T_c from simulations of spherical particles in which, for each value of ϵ, the patchy surface area of a sphere is equal to that of the corresponding spheroid of the same volume, V.

(solid curve), along with $T_c(\epsilon, \chi)/T_c(\epsilon = 1, \chi)$ from simulation. It should be noted that the ratio of the squares of the solid angles only captures a small contribution of the decrease of T_c with ϵ, and so this simple geometric argument does not fully describe the behavior of T_c. This result suggests that the change in surface area that attends an increase in ϵ may only be of minor importance here. To clarify this point, we also include in Fig. 3 the dependence of T_c on ϵ for a series of *spheres* as obtained from simulation such that, for each value of ϵ, the patchy surface area of a sphere is equal to that of the corresponding spheroid of the same volume, V. In short, we choose the patch angle for the sphere, $\delta_\circ$, such that, from Eq. 4.5, $S(\delta, \epsilon, V) = S(\delta_\circ, \epsilon = 1, V)$. Thus, the small increase in surface area with ϵ plays

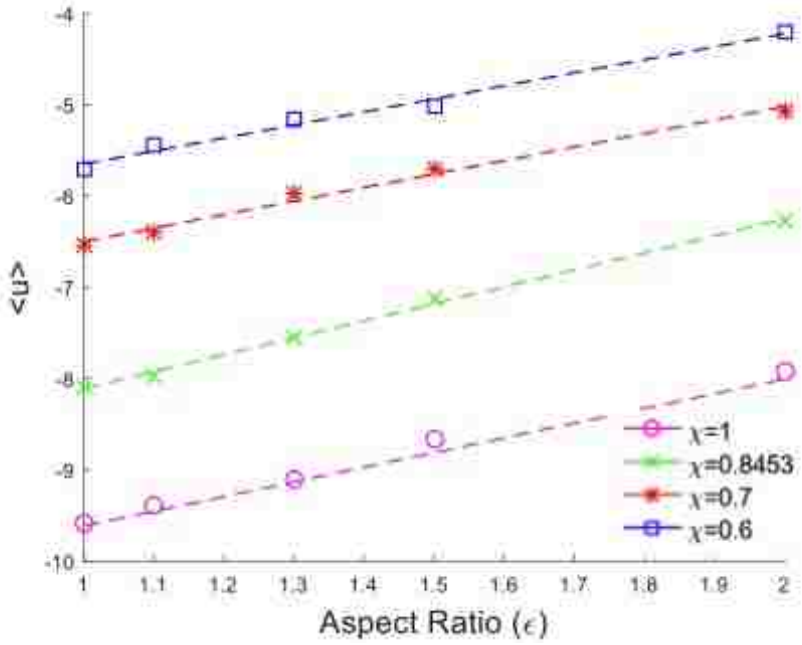

Figure 4.4: The average energy per particle, $\langle u \rangle$, as a function of aspect ratio, ϵ, obtained by conventional Metropolis MC simulation in a single liquid phase with $\rho = 0.62$ at temperatures, T, slightly below the critical temperature. The effective patch coverages shown correspond to: $\chi = 1$ (circles), $\chi = 0.8453$ (crosses), $\chi = 0.7$ (asterisks), $\chi = 0.6$ (squares). The dotted lines are a guide to the eye.

a role in determining T_c, but it alone cannot account for the observed behavior. Thus, the disparity between the values of T_c for the spheres and the corresponding spheroids indicates that shape anisotropy is also an important factor in determining critical behavior in this system.

The shape anisotropy and patchiness inherent in this system may also lead to structural changes in the dense fluid and thereby determine critical behavior. To see this more clearly, we characterized the fluid structure by calculating, for various aspect ratios, both the radial distribution function, $g(r)$, (Fig. 6) and the patch-angle correlation probability, $P(|\hat{u}_i \cdot \hat{u}_j|)$ (Fig. 7), the latter a function of the cosine of the angle between the patch normals for particles in the more dense fluid. As is evident from Fig. 6, the distribution of inter-particle distances remains relatively

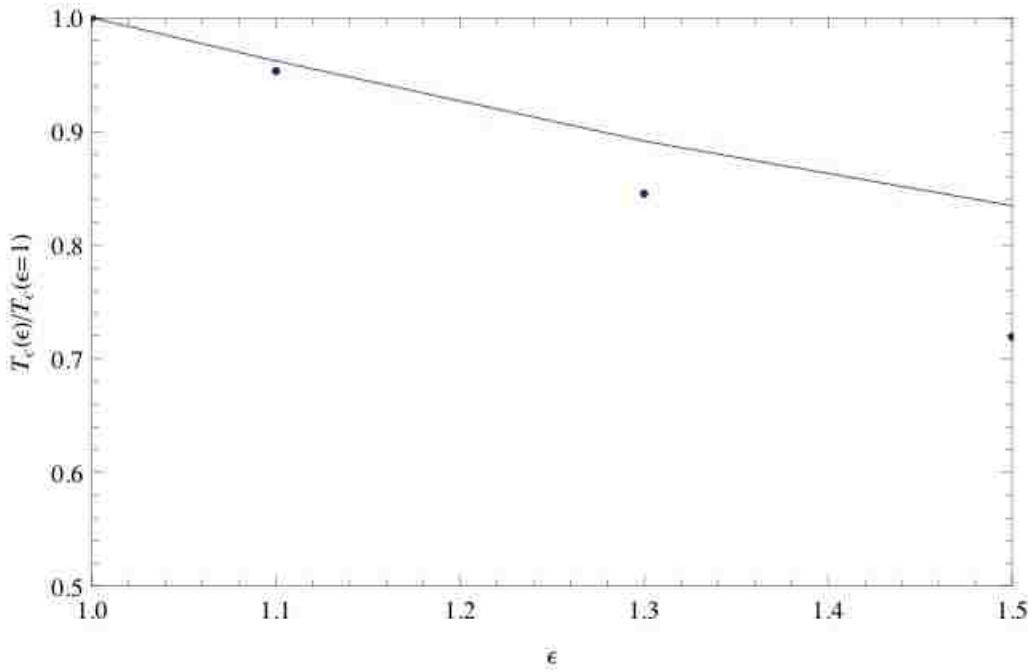

Figure 4.5: The normalized critical temperature, $T_c(\epsilon,\chi)/T_c(\epsilon=1,\chi)$, as a function of aspect ratio, ϵ, as determined from simulation (points) and as estimated from the square of the ratio of solid angles, $[\gamma(\epsilon,\chi)/\gamma(\epsilon=1,\chi)]^2$. For this case, $\chi = 0.7$. Clearly, the dependence on solid angle alone does not fully explain the observed dependence of T_c on ϵ.

constant for different values of ϵ, at least for $\epsilon \leq 1.5$. However, as indicated in Fig. 7, there is evidence for increasing orientational order with increasing values of ϵ, as neighboring patch normals align either parallel or anti-parallel to each other. Thus, for increasing ϵ constraints on patch orientation will lead to changes in phase coexistence as these constraints will alter the ensemble average of the orientational factor in the quasi-square well potential. (see Eq. (3)).

Finally, it is useful to determine whether a universal coexistence curve for the two-patch system may be obtained by a simple scaling procedure. According to the principle of corresponding states, for liquid-liquid phase coexistence the reduced density, ρ/ρ_c, where ρ_c is the critical density, is a universal function of the reduced temperature, T/T_c. All fluids that obey this principle should therefore behave identically when compared in terms of these reduced variables. [51] In Figs. 8 a and b

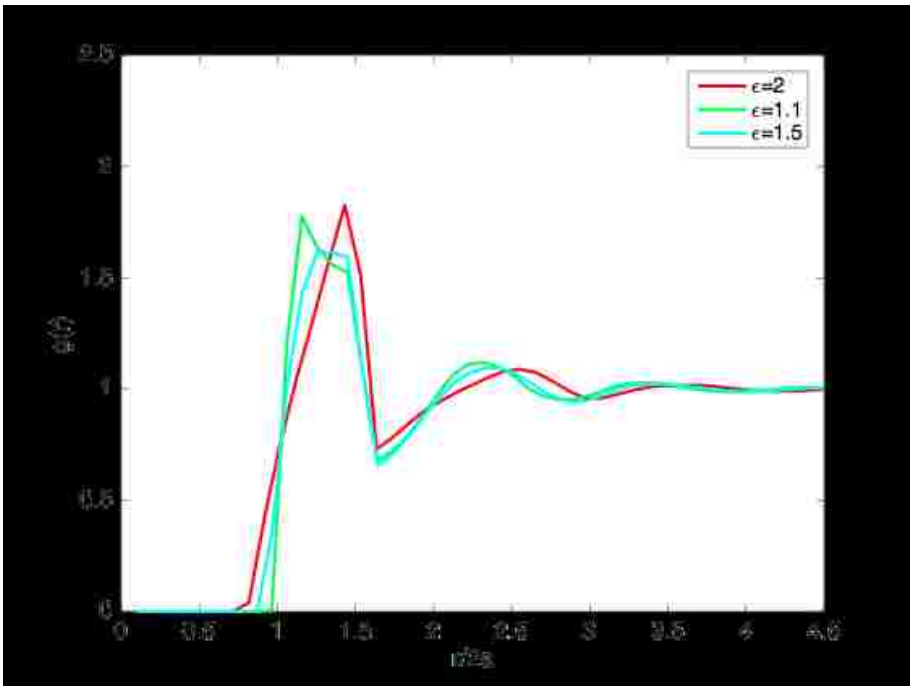

Figure 4.6: The radial distribution function, $g(r)$, as a function of particle separation for systems having $\epsilon = 1.1$ (green) $\epsilon = 1.5$ (cyan) and $\epsilon = 2$ (red). In each case particles has coverage $\chi = 0.7$ and simulation density $\rho = 0.3$. Distances are measured in units of the diameter of a sphere, $2a$, of constant volume.

we present the scaled phase diagrams for systems having aspect ratios $\epsilon = 1.5$ and $\epsilon = 1.1$, respectively. One observes that this scaling works modestly well for the low-density branches, but breaks down for the high-density liquids. This breakdown is attributable to the fact that our choice of patch angles permits bonding of more than one particle per patch and, at higher density, greater bonding is expected. Thus, systems having different patch area fractions behave differently, particularly at high densities.

4.3.2 Particles with Four Patches

Next we briefly consider the case of a system comprising four-patch spheroids for which the spheroid volume, V, and the effective patch area, χ, are held constant

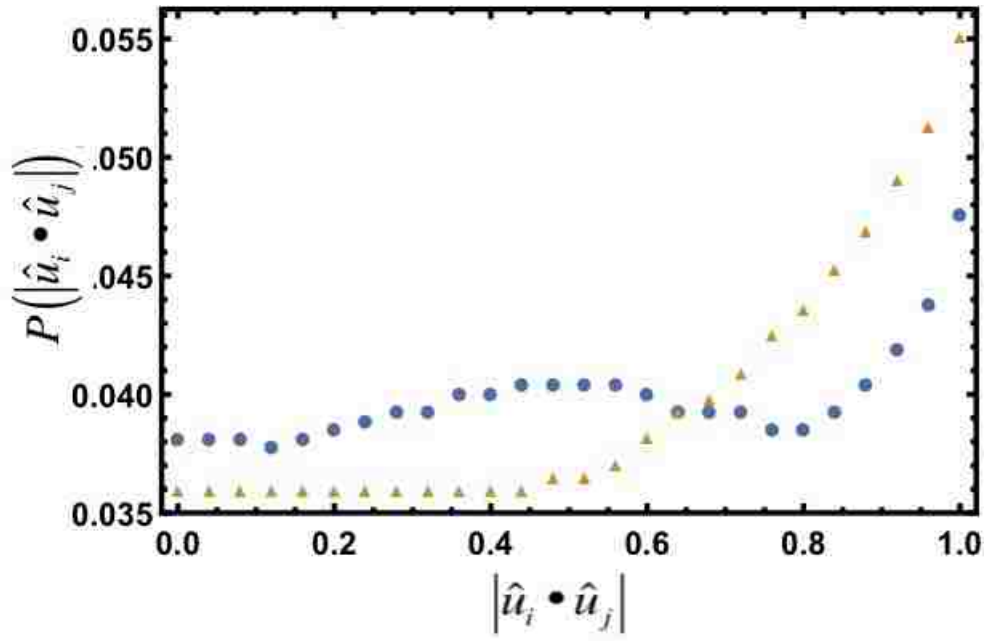

Figure 4.7: The patch-angle correlation probability, $P\left(|\hat{u}_i \cdot \hat{u}_j|\right)$ as a function of the magnitude of the dot product of patch normals. Two cases are considered, namely: $\epsilon = 1.1$ (blue circles) and $\epsilon = 2.0$ (yellow triangles). In both cases particles converage was $\chi = 0.7$ and simulation density $\rho = 0.3$. The plot indicates that, for greater aspect ratio ϵ, the particles have a greater tendency to align parallel or anti-parallel to one another.

for any aspect ratio. Our aim is to highlight the role of patchiness (or valence) on observed critical behavior. Recall that these patches are located on the polar and equatorial ends of the particles. The four patches on such particles, unlike the two-patch case, are not equidistant. The corresponding liquid-liquid miscibility gaps for this system of particles with $\epsilon = 1.1$ and 1.5 are displayed in Figs. 9 a and b, respectively. Note that for particles with four patches, to hold χ constant, each patch is itself smaller than in the case of particles with two patches. Smaller patches imply that fewer particles can bond at any particular patch site. Therefore, in relation to the two-patch case, the phase coexistence curves are lower on the temperature scale even though, in general, greater attractive patch coverage implies greater bonding.

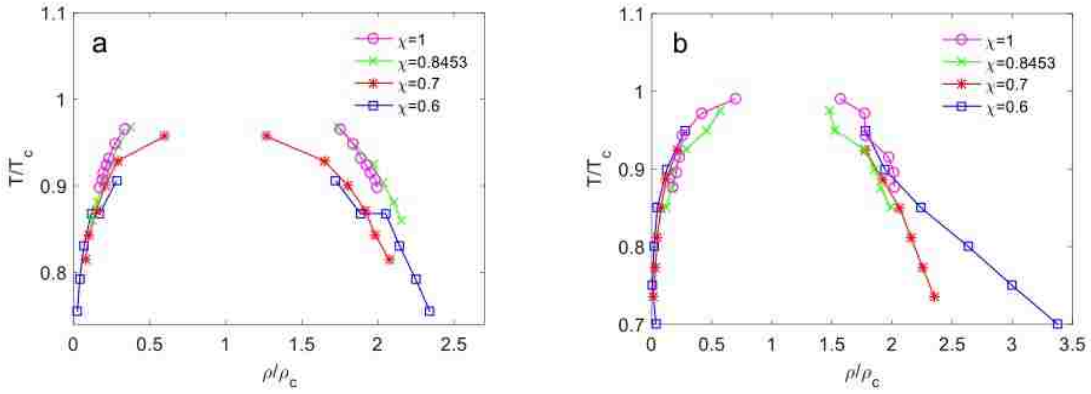

Figure 4.8: Scaled phase diagrams plotted in terms of the reduced temperature, T/T_c, and density, ρ_l/ρ_c, for $\epsilon = 1.1$ (a) and $\epsilon = 1.5$ (b). This scaling works modestly well for the low-density liquid, but less well for the high-density liquid where there is greater bonding between particles.

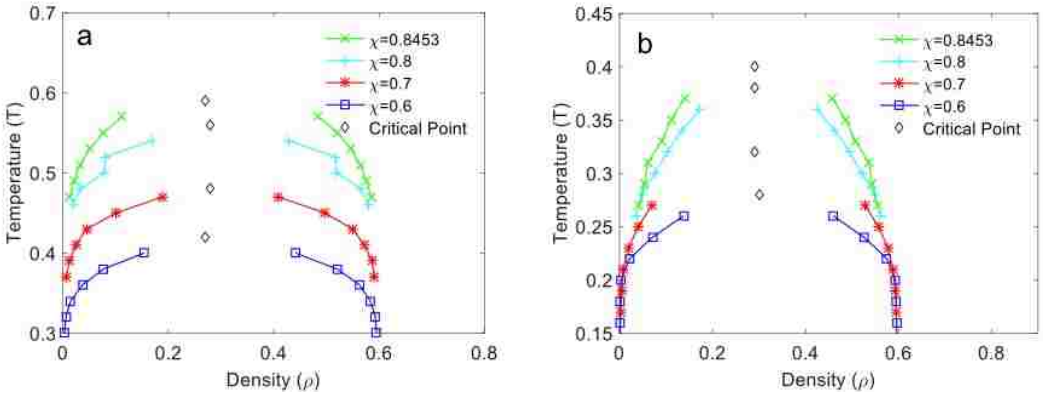

Figure 4.9: Examples of phase diagrams obtained via Gibbs Ensemble MC for particles with four-patch configurations and with $\epsilon = 1.1$ (a) and $\epsilon = 1.5$ (b). The results for various patch sizes χ are shown. Individual patches are smaller than in the two patch case, but they cover the same particle surface area. Points marked with $\diamond$ symbols are again obtained from the law of rectilinear diameter.

Figure 10a displays the dependence of T_c on ϵ for several values of χ. We observe similar behavior to that observed for the two-patch case, with the four-patch case showing a marked linear decrease in T_c with increasing ϵ. To compare the two- and

four-patch cases more directly, we show in Fig. 10b a plot of the reduced critical temperatures $T_c/T_c(\epsilon = 1)$ versus ϵ for these cases. The greater negative slopes for the four-patch system implies that greater anisotropy evinces greater effect. This is true for all values of coverage χ studied here.

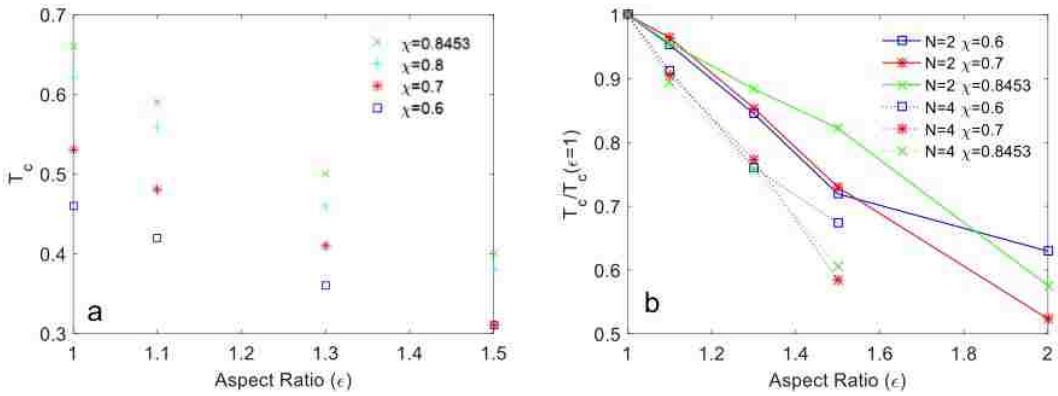

Figure 4.10: a) The dependence of the critical temperature, T_c, on aspect ratio, ϵ, for four-patch systems with $\chi = 0.6$ (blue squares), $\chi = 0.7$ (red asterisks), $\chi = 0.8$ (cyan pluses), $\chi = 0.8453$ (green crosses). b) A comparison of the reduced critical temperature, $T_c/T_c(\epsilon = 1)$, versus aspect ratio, ϵ, for two-patch (solid lines) and four-patch (dashed lines) systems having different values of χ.

Finally we determine whether a universal coexistence curve can be obtained for the four-patch case. Figures 11 a and b show the scaled phase diagrams for systems having aspect ratios $\epsilon = 1.1$ and 1.5, respectively. A comparison of these figures with the corresponding figures for the two-patch case (Figs. 8a and b) indicates that this simple scaling works better in the four-patch case, especially at larger ϵ. This behavior might be expected since individual patch areas are relatively smaller and therefore multiple bonding per patch is suppressed.

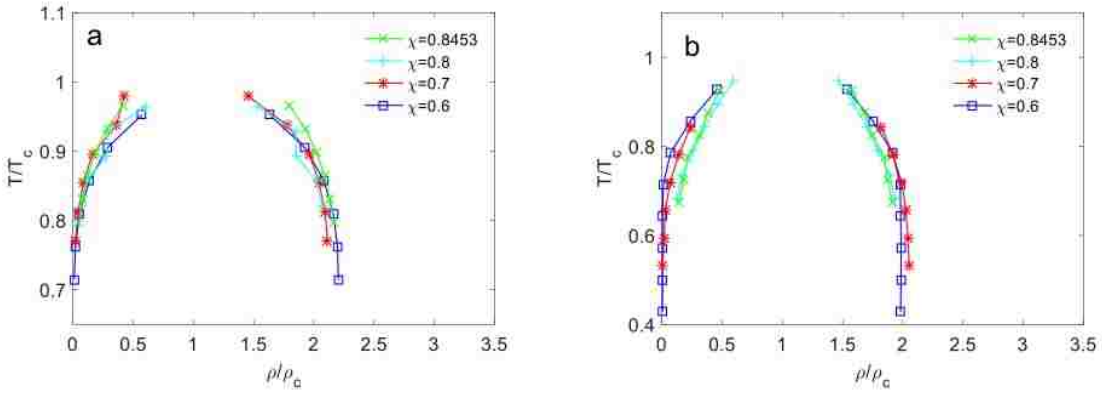

Figure 4.11: Scaled phase diagrams plotted in terms of the reduced temperature, T/T_c, and density, ρ_l/ρ_c, for $\epsilon = 1.1$ (a) and $\epsilon = 1.5$ (b) for the four-patch case. This simple scaling works better than in the corresponding two-patch case (Fig. 8a and b).

4.4 Conclusions

In this work, we examined the impact of combined shape and interaction anisotropy on phase behavior in a colloidal fluid. We modeled shape anisotropy in the form of ellipsoidal particles characterized by their degree of elongation, ϵ, and interaction anisotropy via a number of patches having various surface coverages. Monte Carlo simulation was employed to obtain fluid separation curves for a solution of these particles, and the corresponding critical behavior was analyzed. It was found that particles interact less strongly with increased shape anisotropy and this was attributable to decreased attractive patch coverage, and an increased likelihood for particles to orient in parallel or antiparallel fashion. Moreover, an examination of particles with four patches revealed that this anisotropy effect is more pronounced in this system. This study highlights, then, the importance of both particle shape and energetics on the thermodynamic behavior of colloidal particles, and by extension, proteins. From the results for the two-patch and the four-patch cases, it is reasonable to conclude that, as patchiness increases, the critical temperature decreases more markedly with ϵ. In addition, given that the law of corresponding states works better in the four-patch case relative to the two-patch case leads to the

conclusion that scaling the phase diagram as in Figs. 8 works better as ϵ increases. This behavior was explained by noting the relatively smaller individual patch areas leading to suppression of multiple bonding per patch.

Our model underlines the dual role of both shape and interaction anisotropy. The depression of critical points T_c with decreasing χ highlights the effect of patchiness whereas the linear trend of decreasing T_c with ϵ highlights shape. Varga et al studied the role of shape without patchiness [131] and the Kern and Frenkel patchy model has been studied extensively, recently by Newton et al [85] who examined the role of rotational diffusion independent of translational diffusion. As our model includes surface patchiness and elongated shape, rotational motion will certainly be affected as well. This is the first paper, to our knowledge, that examines both anisotropy parameters in this way.

The extension of our analysis to other related systems deserves some comment. For example, we expect that our results can be readily extended to the case of oblate spheroids where aspect ratio $\epsilon < 1$ and into regions of a phase diagram where one might expect other types of structures, such as particles with nematic ordering [142] [131]. In addition, as noted above, anisotropic interactions also dictate the phase behavior of proteins due, in part, to the differences in exposed surface amino acid groups. Thus, these systems are also amenable to patchy-model, coarse-grained descriptions, and so it is expected we can also analyze their phase behavior using the approach described here. Such studies are the subject of ongoing work.

4.5 Acknowledgments

This work was supported in part by a grant from the G. Harold and Leila Y. Mathers Foundation.

Chapter 5

Thermodynamic Properties of Ellipsoidal Patchy Fluids

Statistical mechanics links microscopic, particle descriptions of a system to thermodynamic whole system measurable quantities. Two such measurable quantities are the specific heat c_V and isothermal compressibility β_T. These quantities can be explored experimentally and also through simulation. Experiments take averages over time, whereas Monte Carlo simulations take averages over an ensemble of identically prepared but randomly different versions the system. In this chapter, c_V and β_T are calculated from the results of NVT Monte Carlo simulations for a system of patchy ellipsoidal fluids. The results of the patchiness and ellipsoidal elongation are discussed.

5.1 Specific Heat

For any given substance, the heat capacity C_V of that substance can be measured experimentally. It is the amount of heat required to change the temperature of that substance by 1 degree kelvin. This is an extensive quantity since it depends on the amount of the given substance. Dividing out the dependence on mass, gives the specific heat c_V. This is a material's property and depends on the substance.

Examining the particles that make up the substance, statistical mechanics says that the specific heat is related to the number of degrees of freedom available to the particles under experimental conditions. By the equiparition theorem, each accessible degree of freedom allows the particle to store energy and the more degrees of freedom the higher the specific heat.

In previous chapters, the NVT ensemble was introduced. This an ensemble which describes the plurality of states for a system of interest in thermal contact with a much larger heat bath. In this system, the internal energy of the system of interest is no longer fixed since energy is exchanged with the heat bath. Also the heat bath is considered to be much much larger than the system of interest so exchanges in energy do not affect the temperature of the heat bath.

According to fluctuation dissipation, if a system obeys detailed balance, particles in contact with a heat bath will appear to move about at random, but the average energy is known. Recalling from chapter 2, the expected value of the average energy of a system in the NVT ensemble is given by:

$$\langle U \rangle = \frac{\frac{1}{N!}\frac{1}{h^{3N}} \int dr^N dp^N U(p^N) \exp\left[-H(r,p)/k_B T\right]}{Q_{NVT}} \tag{5.1}$$

where Q_{NVT} is the canonical partition function:

$$Q_{NVT} = \frac{1}{N!}\frac{1}{h^{3N}} \int dr^N dp^N \exp\left[-H(r,p)/k_B T\right]$$

r^N denotes the position of all N particles. p^N is the momentum of the particles. h is Plank's constant. $H(r,p) = K(p) + U(r)$ is the Hamiltonian of that particles.

The first law of thermodynamics states $dU = \delta Q - PdV$. Changes in a system's internal energy are the result of changes in heat Q added to the system and any work that is done by the system. If the system does no work, volume is held constant and $dU = \delta Q$. The heat capacity, as a measure of how much heat is required to change the temperature of substance is therefore,

$$Cv = \frac{\partial Q}{\partial T} = \frac{\partial U}{\partial T} \tag{5.2}$$

Plugging in the expected value for the system energy and using the product rule and chain rule:

$$\frac{\partial \langle U \rangle}{\partial T} = \begin{array}{c} \frac{1}{Q_{NVT}} \frac{1}{N!} \frac{1}{h^{3N}} \int dr^N dp^N \frac{U(p^N)^2}{k_B T^2} \exp\left[-H(r,p)/k_B T\right] + \\ \left(\frac{-1}{Q_{NVT}^2} \frac{\partial Q_{NVT}}{\partial T}\right) \left(\frac{1}{N!} \frac{1}{h^{3N}} \int dr^N dp^N U(p^N) \exp\left[-H(r,p)/k_B T\right]\right) \end{array} \tag{5.3}$$

The first term on the left hand side is just the expectation value of the energy squared, $\langle U^2 \rangle$. Whereas

$$\langle U \rangle = \frac{\frac{1}{N!} \frac{1}{h^{3N}} \int dr^N dp^N U(p^N) \exp\left[-H(r,p)/k_B T\right]}{Q_{NVT}} \tag{5.4}$$

appears in the second term. This leaves

$$\frac{1}{Q_{NVT}} \frac{\partial Q_{NVT}}{\partial T} \tag{5.5}$$

It can be shown that a first derivative of Q_{NVT} with respect to T

$$\frac{\partial Q_{NVT}}{\partial T} = \frac{1}{N!} \frac{1}{h^{3N}} \int dr^N dp^N \frac{U(p^N)}{k_B T^2} \exp\left[-H(r,p)/k_B T\right] = \frac{< U >}{k_{BT} T^2} Q_{NVT} \tag{5.6}$$

Rearranging this equation,

$$\frac{1}{Q_{NVT}} \frac{\partial Q_{NVT}}{\partial T} = \frac{< U >}{k_{BT} T^2} \tag{5.7}$$

Finally the heat capacity,

$$C_V = \frac{\partial \langle U \rangle}{\partial T} = \frac{1}{k_{BT} T^2} < U^2 > - < U >^2 \tag{5.8}$$

And the specific heat for a system of N particles is

$$c_V = \frac{\partial \langle U \rangle}{\partial T} = \frac{1}{N k_{BT} T^2} < U^2 > - < U >^2 \tag{5.9}$$

This equation relates the macroscopic property, the specific heat with the microscopic fluctuations in the internal energy of the system. In a Monte Carlo simulation in the NVT ensemble, once equilibrium is reached, fluctuations at various MC steps of the internal energy of the system is used to calculate the specific heat.

5.1.1 Model

Having previously studied the phase diagram for patchy ellipsoids in chapter 4, we employed the same model for elongated ellipsoidal particles as described. Briefly, spheroidal particles with one of three axes is longer than the others. The elongated axis, $c > a = b$. The aspect ratio is defined $\epsilon = c/a$. These particles are hard particles, meaning that they cannot overlap. In addition, these elongated particles, have surface regions that interact via an attractive quasi-square well potential. These attractive surface regions, called patches, are defined by the half angle δ that subtends these patches. The amount of total surface area on any particular particle is given by the variable $\chi(\delta, \epsilon, V)$ that depends on the angle δ, the particle's aspect ratio ϵ, the total particle volume V and also the number of patches on the particle surface n. Exact expressions for the surface area of a patch in terms of δ, and $\chi(\delta, \epsilon, V)$ are given in chapter 4.

In this work, we examine particles with $\epsilon = 1.1$ and $\epsilon = 1.5$. With two surface patches on the two opposite polar (pointy) ends of the particles. For each value of ϵ for coverage values χ were examined: $\chi = 1, \chi = 0.8453, \chi = 0.7, \chi = 0.6$.

5.1.2 Method

A monodisperse fluid of N particles in a simulation cell with volume V and temperature T describes the NVT ensembles that were simulated. Two different sets of simulations were performed at various temperatures both above and below the critical temperature T_c. Within a set, each individual NVT simulation can be identified by its temperature. For both sets the total number of particles was held constant at N across values of T. The total number of Monte Carlo steps taken for both was $1X10^6$, and after every 250 steps, the total system energy was sampled and output into a file for analysis.

The way that the two sets differ is in the chosen densities and subsequent volumes across simulations. In the first set, for all values of T, simulations were done such that the number volume $\rho = N/V = 0.65$. Doing this, the critical point on the phase diagram was not approached. Instead simulations remained in the dense fluid

region of the phase diagram for both the $\epsilon = 1.1$ and $\epsilon = 1.5$ particles.

Since volume was held constant, $c_V = \frac{\partial \langle U \rangle}{\partial T}$ could also be calculated directly via numerical differentiation techniques. Here $< U >$ is the energy per particle.

The forward differencing method:

$$\frac{\partial < U(T_i) >}{\partial T} \approx \frac{U(T_j - T_i) - U(Ti)}{|T_i - T_j|} \tag{5.10}$$

for $T_j > T_i$ points taken from simulation (i.e. the average energy per particle results for different NVT simulation runs i and j at temperature T_i and T_j.

The central differencing method:

$$\frac{\partial < U(T_i) >}{\partial T} \approx \frac{U(T_i + |T_i - T_j|) - U(T_i - |T_i - T_j|)}{2\,|T_i - T_j|} \tag{5.11}$$

And the method that uses interpolating second-order Lagrange polynomials

$$\begin{array}{c} \frac{\partial < U(T) >}{\partial T} \approx \\ U(T_{i-1}) \frac{2U(T) - U(T_i) - U(T_{i+1})}{(U(T_{i-1}) - U(T_i))(U(T_{i-1}) - U(T_{i+1}))} + \\ U(T_i) \frac{2U(T) - U(T_{i-1}) - U(T_{i+1})}{(U(T_i) - U(T_{i-1}))(U(T_i) - U(T_{i+1}))} + \\ U(T_{i+1}) \frac{2U(T) - U(T_{i-1}) - U(T_i)}{(U(T_{i+1}) - U(T_{i-1}))(U(T_{i+1}) - U(T_i))} \end{array} \tag{5.12}$$

Note that in the equation above T is a temperature point that was not actually simulated but taken between T_k and T_j, specifically $T = (T_k + T_j)/2$ where $T_k > T_j > T_i$ are simulated temperature points.

The first two methods were employed because they are amongst the simplest. The last was employed because of its increase in accuracy having each derivative point being the result of three found data points instead of two and because the second-order Lagrange polynomial method allows for uneven spacing between sampling points.

The second set of NVT simulations were done such that for a particular value of T, if $T < T_c$ the simulation was performed at the value of ρ given by the more dense fluid phase on the phase diagram at that temperature. If $T > T_c$ simulations were done at the critical density ρ_c.

5.1.3 Results

The purpose of the first set of simulations at constant $\rho = 0.65$ across values of T was to check the agreement of our results against two methods of determining c_V presented above, i.e. via direct differentiation and also via the fluctuation formula. Fig. 5.1 (a-d) show the results for the runs of $\epsilon = 1.1$ particles. For all values of χ shown, the fluctuation formula shows generally good agreement with the values obtained via the various methods of numerical differentiation. The qualitative behavior of the derivatives and the results via fluctuations are generally the same.

Both methods produce results that are rather noisy with the results from the forward differentiation and lagrange method appearing to be the noisiest. For the numerical derivatives this could be the result of the large step size taken between temperatures. Theoretically the range of error for the central differencing method and the Lagrange method should be exactly the same if the difference between different independent variables T is held constant, which is true for all values of χ shown. However for most values of χ there is a marked difference in the results of the central differencing derivatives and the Lagrange differencing method derivatives. Indicating that the error range is at least the difference between the results of the two methods.

The noisiness in the results via the fluctuation method could also be the result of insufficient sampling. In this case, perhaps not enough ensemble average energies contributed to the noisiness of the fluctuation results.

The purpose of the second set of simulations was to examine the behavior of c_V as the critical temperature T_c is approached. In the thermodynamic limit, for second order phase transitions c_V diverges at the critical point as c_V is the derivative of an ensemble averaged quantity. The divergence of c_V behaves in a particular way that is specific to a whole class of systems whose specific heats also diverge in the same way. The set of all the systems that behave in the same way near their critical points is called a universality class. And the behavior of the divergences can be described by exponents, called critical exponents. In particular the critical exponent α relates the behavior of c_V near a critical point to the scaled temperature $c_V \propto |T - Tc|^{-\alpha}$.

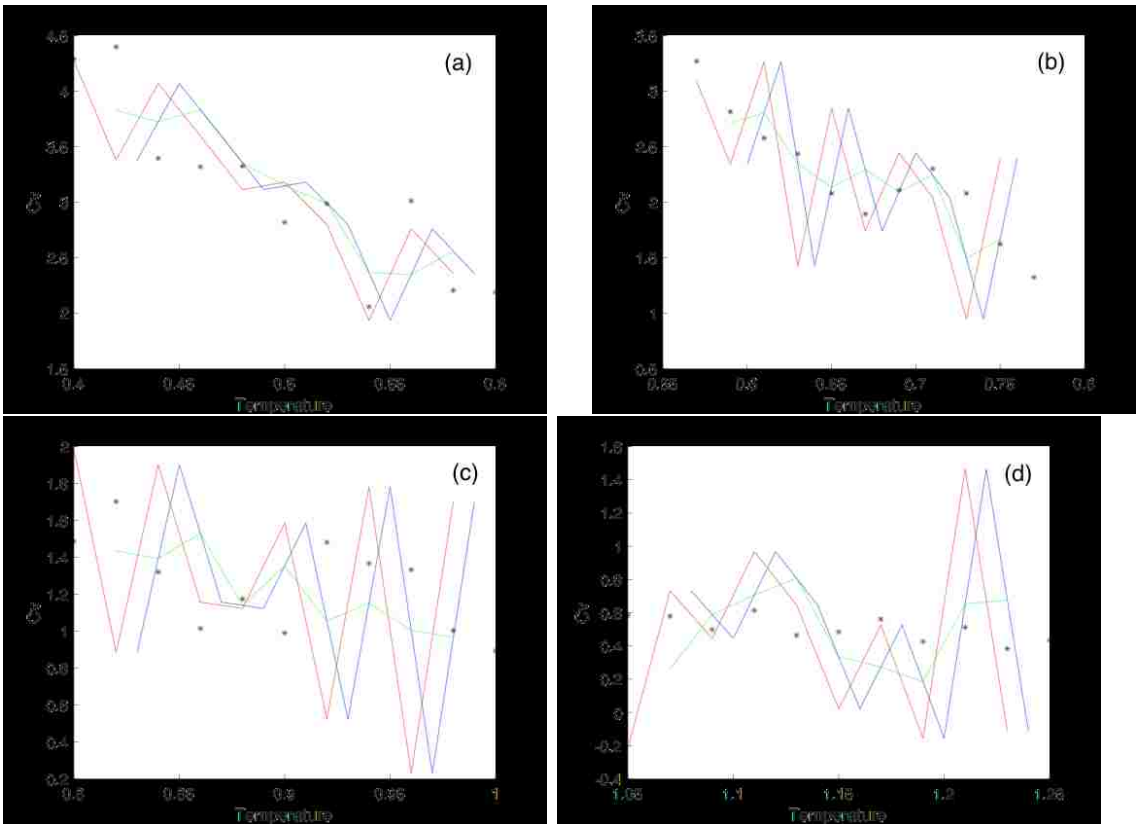

Figure 5.1: Specific heat c_V vs temperature T graphs for $\epsilon = 1.1$ particles for $\chi = 0.6$ (a) $\chi = 0.7$ (b) $\chi = 0.8453$ (c) and $\chi = 1$ (d). For each graph, results shown via line plot are the result of numerical differentiation with red lines the result of forward differencing, green lines the result of central differencing and blue lines the result of interpolation using the second order Lagrange polynomials. The results shown as black $*$ are from finding c_V using ensemble fluctuations in the energy per particle.

These ideas come originally from those developed by Wilson called the renormalization group with the motivation of constructing connections between theories at different length scales. [139] The renormalization group methods can describe phase transitions involving discontinuous changes in physical parameters such as divergence in thermodynamic derivatives such as the specific heat c_V.

c_V only shows true asymptotic behavior in the limit that the simulation box

length $L \to \infty$. In order to make simulations tractable, periodic boundary conditions are used, but even so, finite size effects are introduced. It can be shown that these finite size effects are proportional to the box length $L^{-}d$ where d is the number of dimensions of the system. In this case $d = 3$. In simulation, the divergence of c_V is smoothed out as the result of finite size effects. A smaller simulation box is likely to show a weaker divergence. [24]

To examine finite size effects, it is often useful to run the same simulation at different values of L. Finite size effects both introduce rounding errors in finding true divergence behavior and, at different values of L, peaks can appear shifted with respect to each other. [43] [67] Fig 5.2 shows the result for $\epsilon = 1.1$ and $\chi = 1$ particles. Since the size of the simulation cell was varied with each value of T such that the densities in simulation would be the coexistence densities, the number of particles N, rather than the actual box length L is given. Larger N values correspond to larger L. Varying the number of particles, rather than the actual box length was the method used by Panagiotopoulos when studying finite size effects on the Lennard-Jones fluid using the Gibbs ensemble in which the size of the two boxes fluctuates. [96].

For all values of N, the approximate behavior and location of the peak in c_V is similar, especially for values below T_c. Although the resultant peaks are not very sharp and narrow, the fact that they appear across all simulation sizes at approximately the same value of T indicates that c_V would likely diverge in the thermodynamic limit and for finite values of L it is expected that as L increases, the peaks should both narrow and increase in height, approaching true asymptotic behavior. This is not clearly shown in Fig. 5.2, however the variation in side length L was not actually very big. The difference for example of the box length L used to simulate critical density for the smallest simulation size and the largest was $\approx 20\%$. A more accurate method would be to simulate systems with a much greater difference in L and more specifically for values of L much larger than those studied here. However since systems with large L generally take longer real time to simulate, time constraints meant that smaller simulation sizes were used.

Fig 5.3 (a) shows the results of c_V vs T for all χ for $\epsilon = 1.1$ and 3 (b) shows

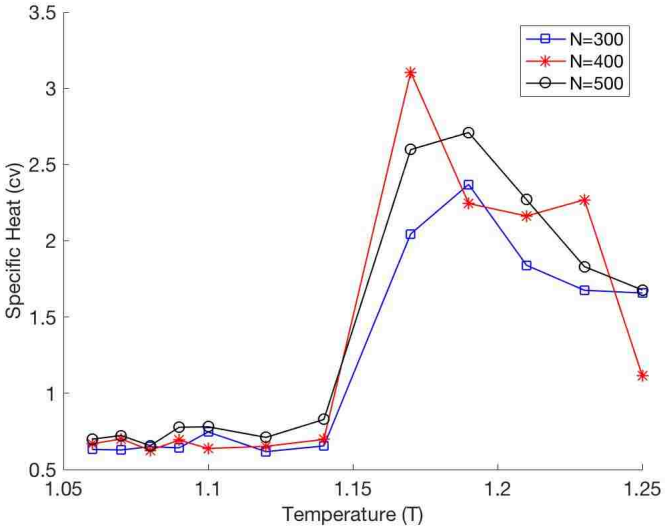

Figure 5.2: Finite size effects for the specific heat for $\epsilon = 1.1$ $\chi = 1$ particles. N number of particles was used as an approximate means of controlling the box length L with larger N corresponding to larger L.

the results for all values of χ and $\epsilon = 1.5$. These results are from the run with the largest simulation size studied $N = 500$. Across all values of ϵ and χ studied, there is a peak in the graph of c_V at values of $T \to T_c$. The largest peak appears to be at $\epsilon = 1.1$, $\chi = 0.8453$. In general the difference between chosen values of T were 0.02 in reduced units. For the simulated values of T, perhaps for $\epsilon = 1.1$, $\chi = 0.8453$ the simulated value near T_c was closer to the actual value of T_c than in any other simulation, hence the stronger divergence curve.

In general, the behavior of c_V did vary with χ. For larger values of χ, c_V was smaller. This is likely because with larger values of χ, the attractive surface area increases so the particles are more energetically linked together than for smaller values of χ. These particles might be more stable to thermal fluctuations than their counterparts with smaller χ values.

Additionally, across aspect ratios the differences in the values of c_V between the largest value $\chi = 1$ and the smallest value $\chi = 0.6$ is larger for greater ϵ. This

behavior is reminiscent of that found for T_c vs ϵ which is that as ϵ increases the particles in the system are less energetically connected.

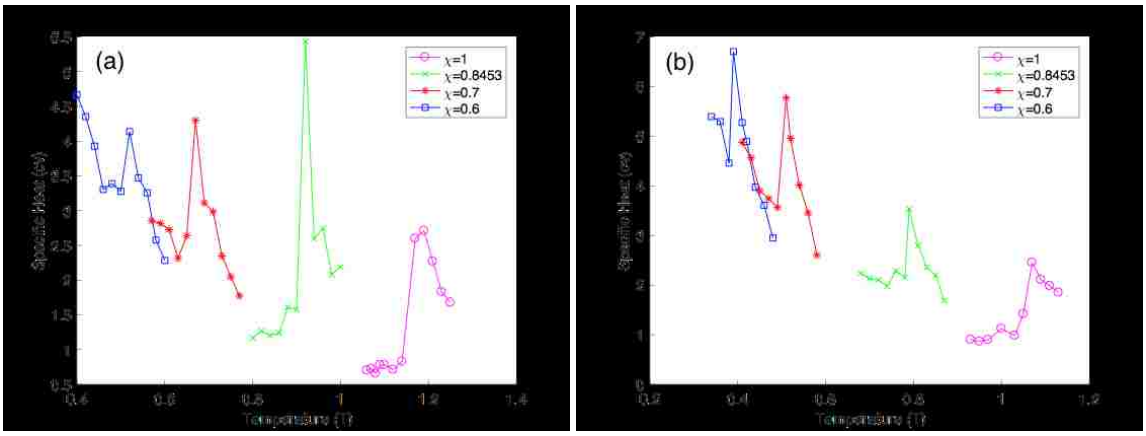

Figure 5.3: Specific heat c_V vs temperature for all studied values of χ for $\epsilon = 1.1$ (a) and $\epsilon = 1.5$(b). Simulations done at coexistence densities ρ for the more dense fluid for temperatures below T_c and at $\rho = \rho_c$ for $T > T_c$. At $T \to T_c$ c_V diverges. This divergence is mitigated by finite size effects.

5.2 Isothermal Compressibility

Turning attention to the isothermal compressibility this is another property that can be understood via measurement. It is the amount by which a given substance's volume changes with applied pressure at constant temperature. $\beta_T = -\frac{1}{V}\left(\frac{\partial V}{\partial P}\right)_T$ The isothermal compressibility can also be expressed via another metric that is indirectly related to experiment, the radial distribution. The radial distribution function $g(r)$ is a measure of the local order in a system of dense fluid. It can be measured experimentally as it is the fourier transform of the structure factor.

Given some particle from a system of N particles, $g(r)$ counts the number of particles some distance r away relative to the number expected for an ideal gas. Imagining the given particle at the origin, an infinitesimal shell of distance r from the particle with thickness dr would approximately have a volume given by

$$V = \frac{4}{3}\pi(r + dr)^3 - \frac{4}{3}\pi r^3 \approx 4\pi r^2 dr \tag{5.13}$$

The number of particles in that shell would then be related to the number density of particles in the system $\rho = N/V$, but since the number density of particles may not be homogenous $g(r)$ gives the exact number of particles at some distance r. Summing up all possible values of r from the center particle

$$N - 1 = 4\pi\rho \int_0^\infty r^2 g(r) dr \tag{5.14}$$

excluding the particle at the origin. The exact definition of the radial distribution function for particles interacting with a pairwise potential is given by:

$$g(r) = (r_1, r_2) = \frac{V^2(N-1)}{NZ_N} \int dr_3 ... dr_N \exp(-\beta U(r_1 ... r_N)) \tag{5.15}$$

Given $g(r)$, it is possible to calculate the isothermal compressibility.

$$\beta_T = -\frac{1}{V}\left(\frac{\partial V}{\partial P}\right)_T = \frac{1}{\rho}\left(\frac{\partial \rho}{\partial P}\right)_T \tag{5.16}$$

$$= \left(\frac{1}{\rho k_B T}\right) + \frac{4\pi}{k_B T} \int_0^\infty [g(r) - 1] r^2 dr$$

5.2.1 Method

Using the NVT Monte Carlo simulation runs at $T \to T_c$ described above for the specific heat c_V the isothermal compressibility β_T was calculated for aspect ratio $\epsilon = 1.1$ and $\epsilon = 1.5$ particles. Like the system energy, configurations of all particles were output every 250 Monte Carlo steps. After equilibrium, all the different particle configurations comprise samples of an ensemble. Those samples were then averaged in the calculation of $g(r)$ for that value of T.

Once $g(r)$ was known, the integral above for β_T was calculated via a simple Monte Carlo integrator where the values of the dependent variable $\beta_{T(r)}$ was evaluated at random values of the independent variable r over the domain $[0, L/2]$ were L is the box length. In simulation when periodic boundary conditions are applied, particles can be no further away from each other than $L/2$. The convergence of this simple integrator was also evaluated with a variance that is on the order of $10^{-1}\%$ of the computed value.

5.2.2 Results

β_T is also a derivative of an ensemble averaged quantity. Therefore, β_T should also diverge at values of $T \to T_c$ if $L \to \infty$. Finite size effects were examined for β_T. Fig 5.4 depicts the result for β_T at various values of N corresponding to changing simulation box length L. The approximate behavior at each value of N is similar. There is a peak in β_T at for each simulation at nearly the same values of T. Therefore, although the peaks are also not very sharp, β_T looks like it would likely diverge in the thermodynamic limit near the critical point.

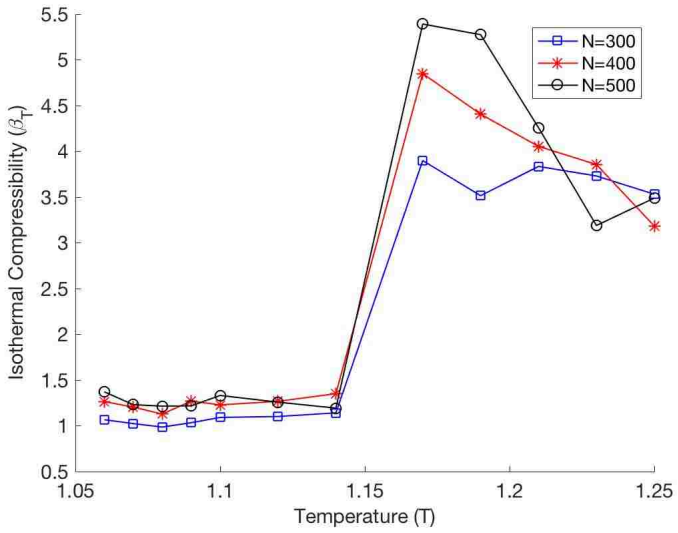

Figure 5.4: Finite size effects for the isothermal compressibility for $\epsilon = 1.1$ $\chi = 1$ particles. N number of particles was used as an approximate means of controlling the box length L with larger N corresponding to larger L.

As opposed to c_V, the behavior of β_T in the thermodynamic limit diverges with a different critical exponent, $\beta_T \propto |T - Tc|^{-\gamma}$. However for β_T the peak increase at $T \to T_c$ is larger than for c_V. This is because critical exponent γ associated with β_T is larger than α associated with c_V. At $L \to \infty$ a stronger divergence for β_T is expected but even at the relatively small system sizes studied, the stronger peak is shown. Furthermore, the larger and more narrow peak with increased system size

is more obvious for β_T Fig. 5.4 than for c_V Fig. 5.2

The peak height vs system size L^d is plotted in Fig. 5.5. The straight line behavior is predicted and explained by Challa, Landau and Binder [24]. Basically peak height should increase with L. This is the result shown in the figure.

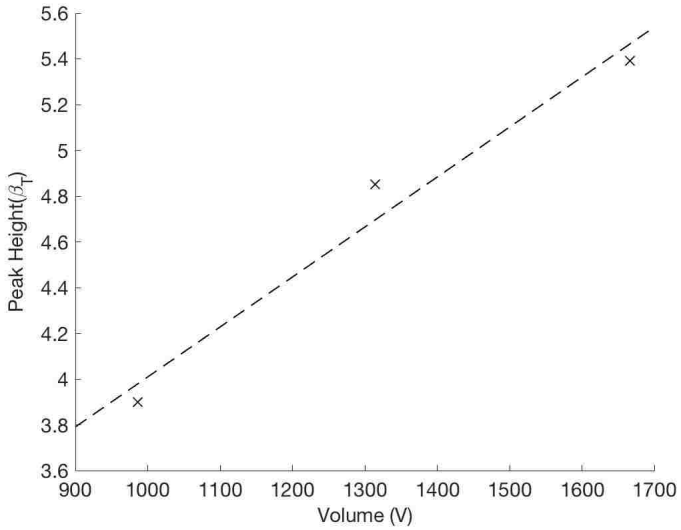

Figure 5.5: Peak height for isothermal compressibility β_T near critical temperatures T_c vs volume $V = L^d$. The values found from simulation are shown as black X. The dashed line is the result of a least squared fit to these points.

Together the exponents γ, associated with strong divergence, and α, associated with weak divergence, are often sufficient to determine the universality class. However exponents alone do not determine the universality class. As in the case of the parameter T which is treated with renormalization methods using a type of scaling, the Hamiltonian of a system also undergoes a type of scaling. These renormalizations act to reduce the number of degrees of freedom and reveal underlying symmetries. Members of the same universality class also must have these symmetries in their reduced Hamiltonians. [39]

There are methods that exist to study the behavior of systems in the thermodynamic limit despite finite size effects. These methods called finite size scaling

depend upon finding a correction factor that relates parameters determined via finite simulation to the "true" values found at $L \to \infty$. With these methods, the actual values of the critical exponents can be found as well as the locations of the critical points if they are not already known.

Fig. 5.6 (a) and (b) show the results of β_T vs T for all values of χ with $\epsilon = 1.1$ and $\epsilon = 1.5$ respectively. As in the case of c_V the largest peak was for $\epsilon = 1.1$, $\chi = 0.8453$. For all calculated values, β_T is small. This is expected as fluids, particularly dense fluids undergo very little volume change with increased pressure. This is because in a dense fluid, there is not much space between particles. Furthermore as the particle are hard, there is an excluded volume which the total volume must exceed.

The graphs of β_T vs T also show the same dependence on χ and ϵ as those c_V underlining the importance of the strength of the attractive energy interactions between the particles. The dependence on ϵ for β_T recalls one other aspect of ch. 4 which is that as ϵ increased there appeared to be a slight increase in a tendency to align. If particles are more aligned than the spacing between the particles might further decrease. Therefore large changes in pressure would affect an even smaller change in volume.

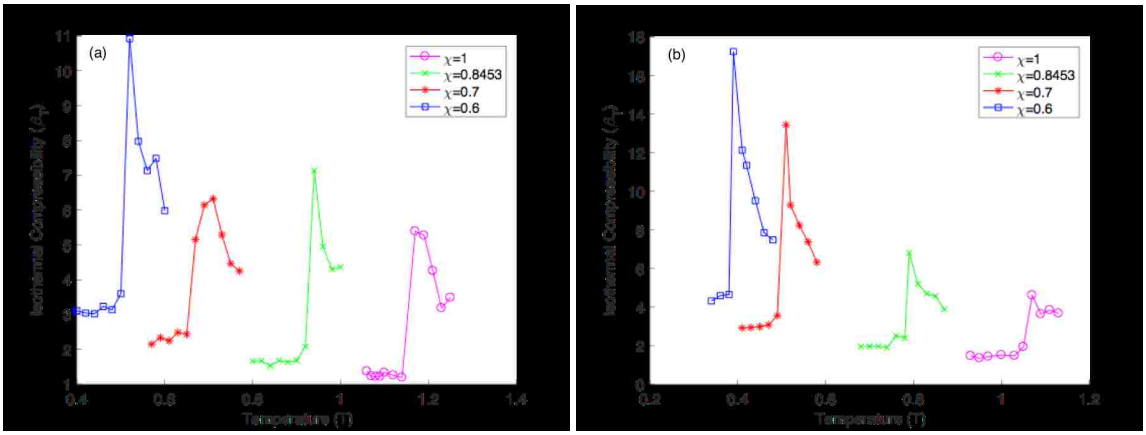

Figure 5.6: Isothermal Compressibility β_T vs temperature T for all studied values of χ for $\epsilon = 1.1$ (a) and $\epsilon = 1.5$(b). Simulations done at coexistence densities ρ for the more dense fluid for temperatures below T_c and at $\rho = \rho_c$ for $T > T_c$. At $T \to T_c$ β_T diverges.This divergence is mitigated by finite size effects.

5.3 Conclusion

c_V and β_T are thermodynamic quantities that can be measured through simulation. Fluid systems of patchy ellipsoidal fluids were studied with Monte Carlo simulations at conditions that approached the critical point on the phase diagram. Both c_V and β_T were found to likely diverge as $T \to T_c$ in the thermodynamic limit with the divergence of β_T being greater. Even at the small system sizes studied the peak beahvior of β_T was greater than that of c_V and present for even the smallest system size. Specific values for c_V and β_T seemed to depend on energetic attraction between particles. Particles with greater inter-particle attraction had smaller c_V and β_T values. The role of ϵ seemed to be in hindering the effective interparticle attraction.

Chapter 6

Phase Diagrams of Patch Ellipsoidal Fluids II: Patchy Distribution

6.1 Introduction

Patchy particles have been an ongoing area of study for several years. There is an entire class of simulation studies on patchy particles that are derived from the original pioneering work on Kern and Frenkel who devised a computationally simple but powerful model of hard spheres with well-defined surface regions of attractive interaction. [60]Their original model has been used by many other researchers in a variety of capacities and has demonstrated a stunning array of behaviors. [119] [46] [109][84] [73][125] [101] [100]

The primary advantage of patchiness is that it allows particles to interact in a directional manner. Patch distribution, meaning, the exact location of the patches on the particle surface with respect to each other therefore is an important aspect that should affect both the dynamic and equilibrium behavior. For example particle contact angle is known to be important at fluid interfaces. Contact energy affects the binding energies and the ways that particles move at the interface. [145].

At the time of this writing although there have been simulation studies that changed the total patch coverage, the number of patches, and range of interaction of the surface patches, but there has not been much research into patch distribution.

In 2007, Fantoni et al did mention patch distribution as in important factor in their studies of hard spheres with sticky surface patches interacting via a Baxter type potential. They noted a distinct change in the location of the critical points for the fluid-fluid transition with different patch distribution. However to change patch distribution, the number of patches were also varied although patch coverage was fixed.[37] In the original Kern and Frenkel work, although they did not make a point to note the effect of changing distribution in that way, the location of the critical points in their study of the fluid-fluid transition did vary significantly and of note, non-monotonically, with changing distribution by way of changing patch number, although total patch coverage was fixed. [60]

Since patch distribution was coupled with changing patch number, it is hard to know the effect of just distribution. The only paper found that examines patch distribution alone was performed by Khan, Haaga and Gunton where the model particle was sphere with two patchy sites. The angle between the two patchy sites, was varied between 30° and 150°. They found that hinge angle plays a crucial role in determining the dynamics and final morphology with micelles, rod-like structures, gels, and larger aggregates all possible with varying hinge angle. [62]

In this work, the model particle is a patchy ellipsoid. Patch distribution is studied by holding both the patch number and total surface coverage fixed. All particles have two patches. The axis of symmetry for the polar patch particles is one of the short semi-axes of the ellipsoids and the axis of symmetry for the side patch particles is the long axis of the ellipsoids. The two patches are found on opposite ends of the particles. For spheres, in simulations where particle rotation moves are allowed, these two patch configurations would be identical, but not for ellipsoids. The liquid-liquid phase separation is studied via Gibbs ensemble and the location of the critical points is found.

6.2 Model

The system studied is fluid comprised of N identical prolate ellipsoids of revolution with semi-axes $a = b < c$. $2a$ the diameter of one of the short sides of an ellipsdoid taken to be the fundamental unit of length in simulation. All other units are reported in terms of this this unit. The aspect ratio, a measure of the elongation of the ellipsoids is defined $\epsilon = \frac{c}{a}$. Values of ϵ studied here are $\epsilon = 1.1, 1.3, 1.5$.

Two ellipsoids interact with potential.

$$U_{ij}\left(r_{ij}, \hat{u}_i, \hat{u}_j\right) = U_{ij}\left(r_{ij}\right) f\left(\hat{u}_i, \hat{u}_j\right), \tag{6.1}$$

The radial part of the potential is given by

$$U_{ij}\left(r_{ij}\right) = \begin{cases} \infty, \text{ (if particles overlap)} \\ -U_0 H\left(\sigma_{ij} + 0.5\sigma - r_{ij}\right), \end{cases}$$

and U_0 is the well depth, H(x) is the Heaviside function. σ represents the total length of the c axis. The approximate closest approach distance for two ellipsoids is σ_{ij}. This distance is as obtained from the Gaussion overlap model of Berne and Pechukas. [15]

$$\sigma_{ij} = 2b \left[1 - \frac{\alpha}{2}\left(\frac{\left(\hat{u}_i \cdot \hat{r}_{ij} + \hat{u}_j \cdot \hat{r}_{ij}\right)^2}{1 + \alpha \hat{u}_i \cdot \hat{u}_j} + \frac{\left(\hat{u}_i \cdot \hat{r}_{ij} - \hat{u}_j \cdot \hat{r}_{ij}\right)^2}{1 - \alpha \hat{u}_i \cdot \hat{u}_j}\right)\right]^{-1/2}, \tag{6.2}$$

where $\alpha = \left(\epsilon^2 - 1\right) / \left(\epsilon^2 + 1\right)$. This corresponds to an interaction range $\lambda = 1.5\sigma$.

The orientational part of the potential that comprises the directional aspect and depends on the patches $f\left(\hat{u_i}, \hat{u_j}\right)$ is given by

$$f(\hat{u}_i, \hat{u}_j) = \begin{cases} 1, \hat{u}_i \cdot \hat{r}_{ij} \leq \cos\delta \quad \text{and } \hat{u}_j \cdot \hat{r}_{ji} \leq \cos\delta \\ 0, \text{otherwise} \end{cases} \tag{6.3}$$

Thus, particles interact if they are within the interaction range given by Eq. (4.2), and if the dot product of the normals of the patch vectors $\hat{u}_i$, $\hat{u}_j$ and the vector $\vec{r_{ij}}$ between them is less than $\cos\delta$, where δ is the half-angle of the patch (i.e., the patches are facing each other).

The total patch area is found via surface integration.

The patch area for polar patches, patches where the symmetry axis is one of the short semi-axes , $S(\delta, \epsilon, V)$, is given by

$$S(\delta, \epsilon, V) = 2\pi \left(\frac{3V}{4\pi}\right)^{2/3} \epsilon \int_{u_{min}}^{1} du \sqrt{(1 - e(\epsilon) u^2)}, \tag{6.4}$$

where given a desired patch size, χ, u_{min} is related to the size of the patch as $u_{min} = (1/\epsilon) / \sqrt{\left(\tan^2 \delta + (1/\epsilon)^2\right)}$.

For side patches, where the symmetry axis is the long axis c,

$$S(\delta, \epsilon, V) = 2\pi \left(\frac{3V}{4\pi}\right)^{2/3} \epsilon \int_{0}^{\delta} d\theta \sin^2 \theta \sqrt{1 + \frac{1}{\epsilon^2} \cot^2 \theta}. \tag{6.5}$$

where θ is the standard polar angle.

Total fractional patch surface coverage is given by χ and defined as the total surface area of the ellipsoid covered by all patches, divided by the total surface area of the ellipsoid. Note that this is a different definition of χ than was used in ch. 4. Total surface area increases with ϵ and in the previous work, χ was held fixed so that the total patch area was constant. In this case χ is allowed to vary with increasing surface area as ϵ moves away from the spherical case.

The reason for this change is that the definition of χ that will be used here is more simple to understand and for the range of ϵ values studied the difference in actual patch size is not large. Also since the primary interest is in comparisons between particle distributions not between different values of aspect ratio, keeping a simple definition for χ makes sense.

Fig. 6.1 illustrates several of the types of particles studied as well as an image depicting two interacting particles and vectors r_{ij} and patch normals $\hat{u}_i$ and $\hat{u}_j$.

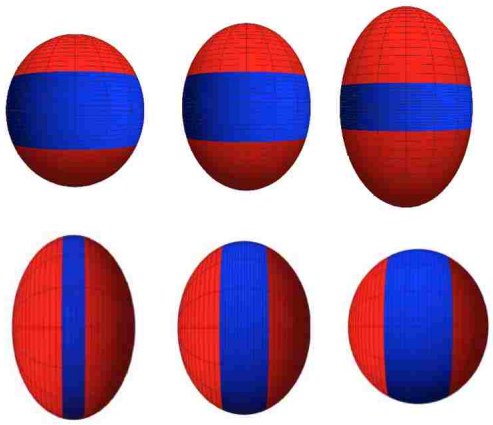

Figure 6.1: Examples of the various types of ellipsoids studied. The top row of particles have so called polar patches with varying fractional coverage. The bottom row of particles have so called side patches. These particles comprise all aspect ratios studied, $\epsilon = 1.1$, $\epsilon = 1.3$ and $\epsilon = 1.5$ and $\chi = 0.6$, $\chi = 0.7$ and $\chi = 0.8453$.

6.3 Methodology

Gibbs ensemble Monte Carlo simulations were performed in order with map out two-phase coexistence at various values of $\epsilon > 1$ and χ. [95] Equilibration time was between $5x10^5$ and $1X10^6$ Monte Carlo steps with higher ϵ value particles taking longer to equilibrate. The results from $\epsilon = 1$ are those from the original work by Kern and Frenkel. $N = 512$ total particles, the sum of all particles in both simulation boxes and V_{box} the initial density of each box was chosen to be such that $\rho_{box} = 0.3$.

After coexistence curves are mapped via the Gibbs ensemble method estimate of the critical temperature, T_c, and critical density, ρ_c, using the law of rectilinear diameter was performed [21]. With found values for the liquid and gas densities, ρ_{liq} and ρ_{gas}, respectively,the critical temperature and density was found by solving

the coupled system of equations

$$(\rho_{liq} + \rho_{gas})/2 = \rho_c - A \cdot |T - T_c| \,, \tag{6.6}$$

$$(\rho_{liq} + \rho_{gas}) = B \cdot |T - T_c|^{0.32} \,, \tag{6.7}$$

A and B are parameters to be determined based on a best fit to simulation data.

Standard Metropolis algorithm NVT ensemble simulations were performed in the single-phase dense fluid region at $\rho = 0.62$ with the goal of finding ensemble averaged energies. Further details are given in the previous work.

6.4 Results

The goal of this work was to examine the effect of changing patch distribution on the phase behavior of a system of patchy ellipsoids. To that end, the Gibbs ensemble method was used to map the fluid-fluid coexistence curves, by varying the simulation temperature for each of two systems of equivalent ellipsoids at various aspect ratios ϵ, one having polar patches and one having side patches.

Consider first the system of particles with two polar patches (i.e. patches at the two pointy ellipsoid ends). The fractional patchy coverage is given by χ. The resultant liquid-liquid miscibility gaps for this system for particles with $\epsilon = 1.1$ and 1.5 are displayed in Figs. 6.2a and b, respectively with black curves.The locations of the critical points, $T_c\,(\epsilon, \chi)$, are also shown in the figures (with diamonds). In each figure, the bottom (top) curves depict the phase separation for particles with $\chi = 0.6$ ($\chi = 0.8453$)

Fig 6.3a and b depicts the found liquid-liquid miscibility gap for the system of particles with two side patches with blue curves. The fractional patch coverage is again given by χ. As in the previous graph, the results for $\epsilon = 1.1$ and $\epsilon = 1.5$ particles are shown.

For both sets of particle distributions, as in the previous work, greater attractive patch coverage results in higher coexistence temperatures. Note again that the total

surface area of the patch increases with ϵ. So a particle with $\chi = 0.6$ and $\epsilon = 1.1$ has smaller patches than a particle with $\chi = 0.6$ and $\epsilon = 1.5$. However, since particles with the same aspect ratios but different patch configurations have the same total patch surface area, the results for the two patch distributions are comparable.

The Gibbs ensemble runs were done such that the range of temperatures investigated for each type of run was similar across particle patch distributions. Although the overall shape of the phase graphs are the same, particles with polar patches were found to have a wider miscibility gap.

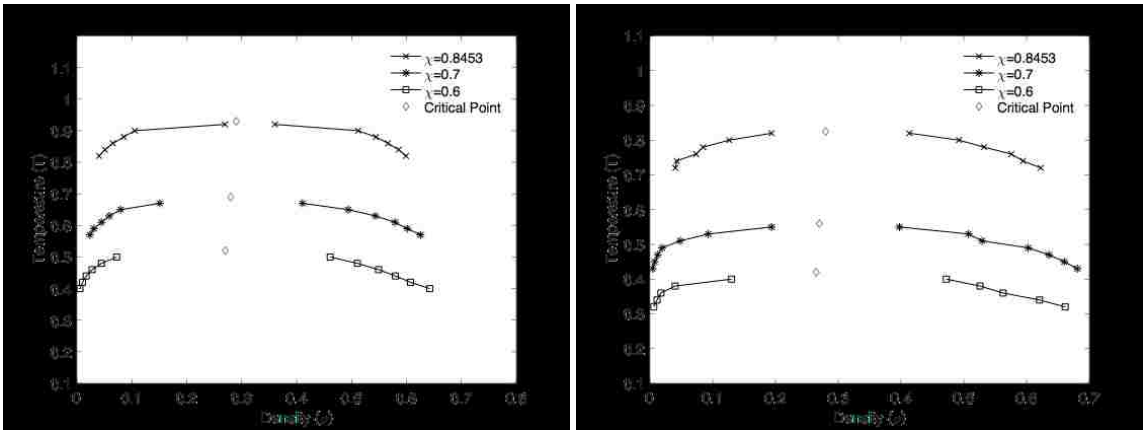

Figure 6.2: Examples of phase diagrams obtained using Gibbs Ensemble MC for particles with two polar patches and either $\epsilon = 1.1$ (a) or $\epsilon = 1.5$ (b). The patch area fraction, χ, is given in the legend. The $\diamond$ symbols denote estimates of critical temperatures, as obtained using the law of rectilinear diameter.

In order to compare the effect on the phase diagram across the two patch distributions it is instructive to examine the critical points. Fig. 6.4 is a plot of the critical temperature T_c as a function of aspect ratio ϵ for all values of χ studied.

For both types of patch configuration, T_c decreases with ϵ, which was the expected result from the previous work. Additionally, the discrepancy between the blue and black curves reveals that indeed patch distribution does play a role in determining phase behavior, the importance of which seems to increase with increasing aspect ratio and patch coverage. For smaller values of χ, $\chi = 0.7$ and $\chi = 0.6$ there is not much difference in T_c at the aspect ratios studied. In fact, the difference

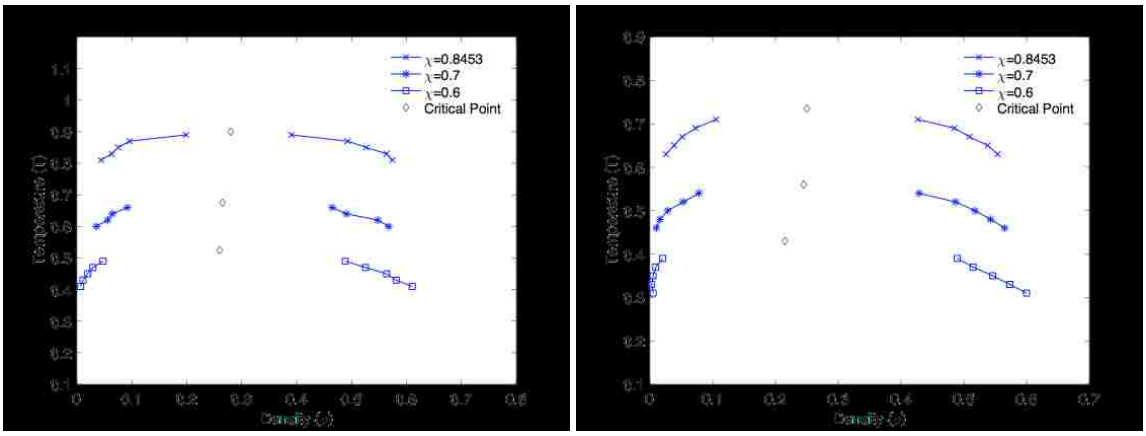

Figure 6.3: Examples of phase diagrams obtained using Gibbs Ensemble MC for particles with two side patches and either $\epsilon = 1.1$ (a) or $\epsilon = 1.5$ (b). The patch area fraction, χ, is given in the legend. The $\diamond$ symbols denote estimates of critical temperatures, as obtained using the law of rectilinear diameter.

between critical temperatures is found to be zero at certain points for these smaller values of χ. However, for the largest fractional patch coverage $\chi = 0.8453$, there is a marked difference between the results for the polar patch particles and the side patch particles with the largest discrepancy at the largest value of ϵ.

The critical density ρ_c also seems to be affected by the change in patch distribution. Fig. 6.5 shows ρ_c as a function of ϵ for the polar patch particles in black and side patch particles in blue. Although the behavior of ρ_c is non-monotonic and more jagged than T_c one key feature of this plot is that for all values of χ comparing between ρ_c for the polar patch and ρ_c for the side patches, the side patch ρ_c is always less than the equivalent polar patch ρ_c. This graph further underlines the fact that patch distribution makes a difference in phase behavior and that side patches affect a notable shift to lower density phase behavior.

To understand why this might be, the average internal energy per particle was found via ensemble averages using a standard NVT ensemble in the high-density fluid. In particular, the since $\chi = 0.8453$ particles seemed to show the most difference in behavior with changing patch distribution, only those particles were simulated.

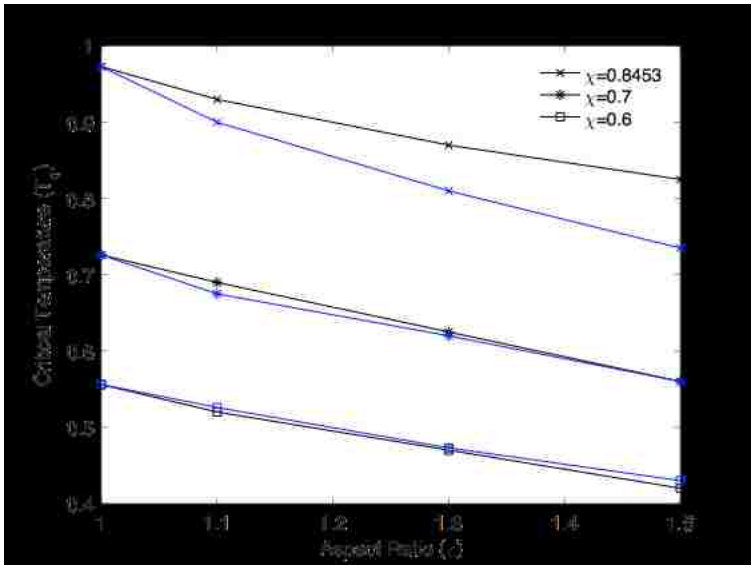

Figure 6.4: The critical temperature, T_c, versus aspect ratio, ϵ, for several values of χ. The results for the polar patches is shown in black. Whereas results for the side patches are shown in blue. Simulation results from this work comprise all $\epsilon > 1$. $\epsilon = 1$ results are taken from literature [60].

As in the previous work, for both the polar and the side patches the linear increase indicates that for both the side and polar patches, the particles are bonded less strongly as the aspect ratio increases. However these results are surprising because although the location of the critical temperature T_c seems to be lower for side patches the average energy per particle, is higher overall for side patches. Indicating that the difference in critical phase behavior is not just the number of bonds that the particle is making but somehow the shape of the particle must be important and exactly how those bonds are made is important.

The radial distribution function of the side and polar patches in the high-density fluid at coexistence densities slightly below T_c is calculated for the case of $\epsilon = 1.5$ and $\chi = 0.8453$ particles where the difference in phase behavior is largest. The black curve indicates the results for the polar patches. The blue curve shows results for the side patches. The shape for both side and polar patches indicates a dense a fluid.

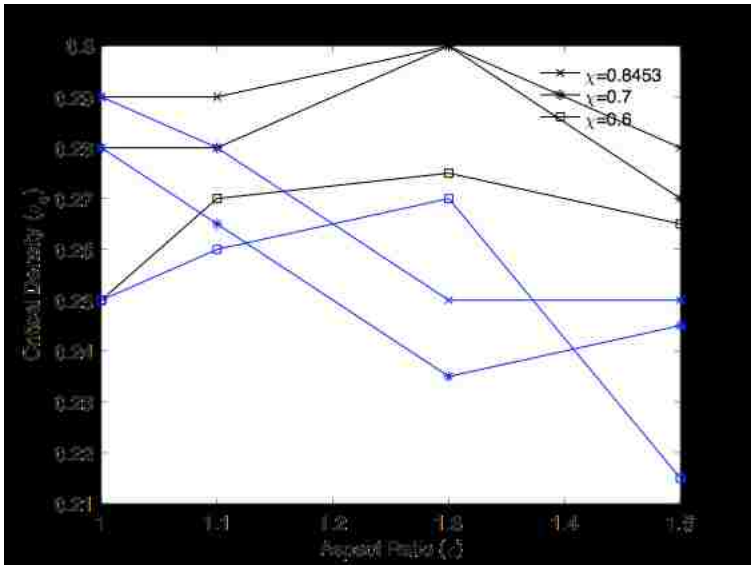

Figure 6.5: The critical density, ρ_c, versus aspect ratio, ϵ, for several values of χ. The results for the polar patches is shown in black. Results for the side patches are shown in blue. Simulation results from this work comprise all $\epsilon > 1$. $\epsilon = 1$ results are taken from literature [60].

There is a difference between the blue and black curves. As the radial distribution function is a measure of the local order, for particles with side patches, given any particular particle, there are a greater number of close neighbors than there are for the polar patches.

This result supports the results from calculating the internal energy per particle. Since the closer a particle is to its neighbors, the more likely a particle is to find another particle with which to bind. Additionally, the radial distribution seems to indicate that the distance between neighbors that are further away is greater for particles with side patches.

To investigate the possibility that there may be some orientational ordering taking place, the dot-product of the normal vectors of these patchy particles is calculated vs the probability of finding that dot product. This rough estimate for orientational ordering was used in the previous work, to find that for particles

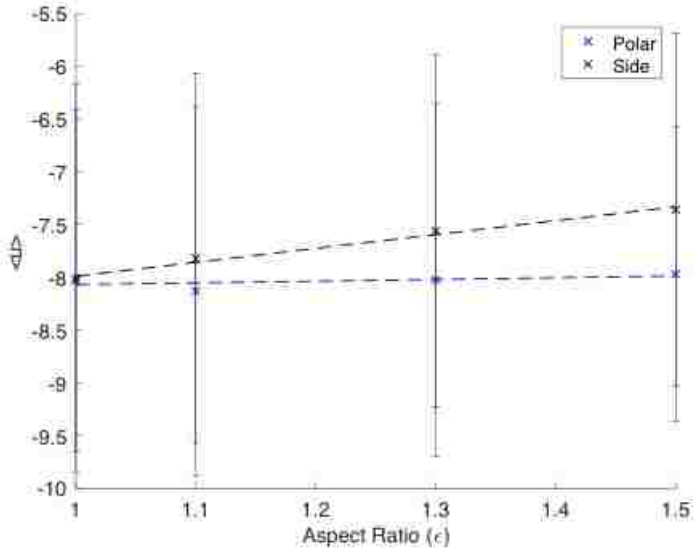

Figure 6.6: The average internal energy, versus aspect ratio, ϵ, for several values of $\chi = 0.8453$. The results for the polar patches is shown in black. Results for the side patches are shown in blue. Results obtained via conventional NVT ensemble Monte Carlo.

with increasing aspect ratio, there is a slightly greater tendency to adopt some sort of orientation. However, this tendency was very small. The results for the side and polar patches also very small. The orientational order parameter $P_2 = \frac{1}{2}\langle 3(\hat{u}_i \cdot \hat{u}_j)^2 - 1\rangle$ was also calculated for both and found to be on the order of $10^{-}4$.

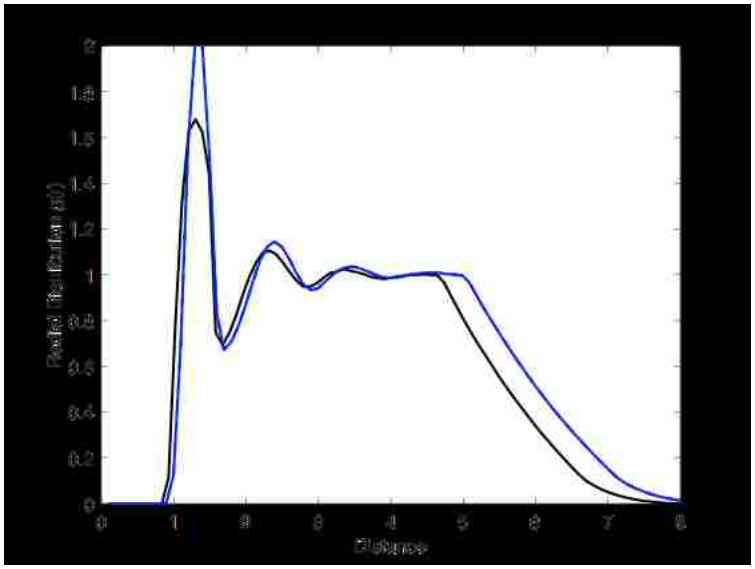

Figure 6.7: Radial distribution function for $\epsilon = 1.5$ and $\chi = 0.8453$ particles for polar (black) and side (blue) patch particles. Results obtained from Gibbs ensemble configurations at densities for the high-density fluid slightly below T_c for each patchy particle type.

6.5 Conclusions

Together these results indicate that there might be a difference in behavior at the local particle level and at the fluid level. The stronger bonding between particles with side patches and the increased local proximity indicate that particles with side patches are at least locally bonded more strongly.

However at the fluid level, the greater width of the miscibility gap and the higher values of T_c for the polar patches indicate that perhaps at longer ranges, particles with polar patches can comprise a fluid with stronger bonding. This is also supported by the radial distribution. As particles further away are closer to each other for particles with polar patches.

Additionally the found result that smaller χ particles have a smaller difference in patch distribution behavior is also surprising. Since in the limit of total $\chi \to 1$ polar patch particles and side patch particles should be exactly the same. This behavior

was not really explored in this work as the focus was on the divergent results for $\chi = 0.8453$ but the similarity between side and polar patches for small χ is an area of interest that should be explored in the future. At the very least, particle patch distribution was shown to be a factor in determining phase behavior and that role may be quite complicated.

Chapter 7

Future Work: Isotropic to Nematic Transition

7.1 Note

There is existing published work on the isotropic to nematic transition for ellipsoids in an attractive quasi-square well. The goal of this chapter was originally to study the effect of patchiness (i.e. particles with directional interactions that are not completely encompassed by the attractive square-well). The results of the published work could not be verified, so the patchy aspect has yet to be studied. Since so much time was dedicated to this goal, the unverified simulation results are presented here.

7.2 Introduction

Ellipsoid models are an extensively studied class of models that have been used to examine interesting properties of a wide variety of real systems. Ellipsoids, in particular, ellipsoids of revolution which are defined by an elongation in one three otherwise equal axes are the simplest non-spherical shape. The degree of elongation is characterized by the aspect ratio $\epsilon = c/a$ with the three spheroid axes $c > a = b$. This elongation from spherical to spheroidal is a type of anisotropy. There are

many different types of anisotropy and isotropic particles have been the subject of great interest and many reviews, [47],[29],[56],[4] the reason being that anisotropic particles are known to self-assemble into materials with a wide variety of novel and desired properties.[127], [49], [59],[82], [20] There are currently many new and ongoing advances in simulation and synthesis of particles carrying some sort of anisotropy. [88], [69], [135], [122], [52]

A colloidal fluid of shape anisotropic very elongated rods with solely hard core interactions has been shown since the pioneering work of Onsager to undergo an isotropic to nematic phase transition. [93]. Since then the simulation work of Frenkel and Mulder showed that hard ellipsoids of revolution with elongated axes as little as ≈ 3.7 times the length of the other two axes also undergoes the isotropic to nematic transition.[42], [41] In more recent work materials that include, at least in part, elongated colloids have significantly modified rheological properties such as changes in elastic modulus and yield strength. [126][137] Additionally there are many elongated rod or ellipsoid type particles found in nature including biological ones such as: f-actin, fd-virus and tobacco mosaic virus, to inorganic particles such as boehmite, hematite and laponite clays. [3], [103], [33], [44] [140], [102], [12]

Particles need not carry only one type of anisotropy. In fact particles with more complex anisotropic properties often display a greater richness of behavior. Furthermore natural materials rarely display one type of anisotropy. In the case of both the viruses and the mentioned above, their elongated particle shapes also include surface regions with charge interactions. [40] [102] One way that simulation studies have used to capture this type of anisotropy on particles surfaces is via the introduction of so called patchy surfaces. Particle patches were originally introduced by Kern and Frenkel for spherical particles. In this model otherwise hard-core spheres had surface regions that interact via an attractive square well potential. [60] The power and flexibility of this patchy model has been demonstrated repeatedly in many studies in which patch number, patch size, the range of patchy attractive interaction, and patch orientation have been varied to produce an incredible array of different behavior. [119], [84], [46], [109], [110], [100], [17],[23]

The isotropic to nematic phase transition is also independently an ongoing area

of interest. The nematic phase is a type of liquid crystal, characterized simply by particles having orientational ordering. Recent work that examined the isotropic to nematic phase transition include work on the tobacco mosaic virus [40] simulation studies of polymers undergoing the I/N transition [36] [28] and polydisperse solutions of colloidal platelets. [25]Further studies on the ellipsoids were done by Odriozola et al who showed that hard ellipsoids with attractive quasi-square well interactions and elongation axis 5 times the length of the other two axes undergo the I/N transition as shown originally by Frenkel and Mulder, [92][13] but also that the attractive interparticle potential shifted the phase diagram to higher packing fractions. [131]

In this work, we aimed to expand on the model originally proposed by Odriozola of hard ellipsoids with $\epsilon = 5$ in an attractive quasi-square well by adding patchiness as a modification and seeing how directional interactions given by both the shape anisotropy and the interaction anisotropy affects the I/N phase behavior.

7.3 Model

We consider a system of N uniaxial hard ellipsoids with $\epsilon = 5$. The short particle axis diameters $2a = 2b$ are considered the fundamental unit of length, with all other lengths given in terms of this unit. With $\epsilon = 5$ the elongated particle axis is $c = 2.5$. A fluid of these such particles interact via pairwise potential having both a radial component U_{ij} and a orientational component $f\left(\hat{u}_i, \hat{u}_j\right)$

$$U_{ij}\left(r_{ij}, \hat{u}_i, \hat{u}_j\right) = U_{ij}\left(r_{ij}\right) f\left(\hat{u}_i, \hat{u}_j\right), \tag{7.1}$$

Where two ellipsoids, i and j, displaced by $\vec{r}_{ij} \equiv \vec{r}_i - \vec{r}_j$ having patches with unit normals $\hat{u}_i$ and $\hat{u}_j$. The radial component that depends only on the distance between particles $\vec{r}_i - \vec{r}_j$ is given by:

$$U_{ij}\left(r_{ij}\right) = \begin{cases} \infty, \text{ (if particles overlap)} \\ -U_0 H\left(\sigma_{ij} + 0.5\sigma - r_{ij}\right), \end{cases}$$

and where U_0 is the well depth, H(x) is the Heaviside function and σ represents the total length of the c axis. The parameter σ_{ij} is an approximation of the closest

approach distance of the two ellipsoids. This approximation is made via a Gaussian overlap model. In our previous work we have relied upon the model originally proposed in 1972 by Berne and Pechukas.[15] However a modification to the original closest approach approximation was made by Rickayzen in 1998 that added an additional term that accounts for a mismatch in the exact value for closest approach distance and that obtain from the approximation in the case of two elongated particles approaching one another in the shape of a T. [108] This modified approximation to σ_{ij} is given by:

$$\sigma_{ij} = 2a \left(1 - \frac{1}{2}\chi \left[A^{+} + A^{-} \right] + (1-\chi)\chi\prime \left[A^{+}A^{-} \right] \right)^{1/2} \tag{7.2}$$

$$A\pm = \frac{\left(\hat{r_{ij}} \cdot \hat{u_i} \pm \hat{r_{ij}} \cdot \hat{u_j} \right)^2}{1 \pm \chi \hat{u_i} \cdot \hat{u_j}}$$

$$\chi = \frac{\epsilon^2 - 1}{\epsilon^2 + 1}$$

$$\chi\prime = \left(\frac{\epsilon - 1}{\epsilon + 1} \right)^2$$

Surface patches on the ellipsoids are assumed to be on the two polar (pointy) ends of the ellipsoids. The orientational $f\left(\hat{u_i}, \hat{u_j}\right)$ in Eq. (4.1) is given by

$$f(\hat{u}_i, \hat{u}_j) = \begin{cases} 1, \hat{u}_i \cdot \hat{r}_{ij} \leq \cos\delta \quad \text{and } \hat{u}_j \cdot \hat{r}_{ji} \leq \cos\delta \\ 0, \text{otherwise} \end{cases} \tag{7.3}$$

As in the previous chapter δ is the half angle that subtends the particle patch size. For $\delta = \pi$ this would imply that the entirety of one particle's hemisphere's is covered in an attractive patch. Total patch number on a particle n would have to be $n = 2$ with both hemisphere's having patches and $\delta = \pi$ to describe the original model of Odriozola in which the entire particle is encompassed by an attractive square well.

As previously noted, if particle volume is held constant, particle surface area increases with increased ϵ. Therefore the ratio of particle that is covered by a patch is a function of ϵ. However for this work, ϵ is held constant at $\epsilon = 5$. Further details can be found in the preceding chapters.

7.4 Methology

We employ a replica exchange Monte Carlo method in the an extended ensemble of otherwise standard NPT systems , $Q_{ext} = \prod_{i=1}^{n_r} Q_{NP_iT}$. Here n_r number of replicas of an NPT ensemble all have the same initial conditions except for pressure P_i. Each replica is run in parallel with all the others. As the Monte Carlo progresses, the pressure between these ensembles is periodically swapped with the following acceptance rule.

$$P_{acc} = min(1, exp(\beta(P_i - P_j)(V_i - V_j)) \tag{7.4}$$

This can be thought of as a type of parallel tempering except in pressure instead of temperature. In practice, within each replica there are three types of Monte Carlo moves: particle translation, rotation, and simulation box volume change. The only inter-replica Monte Carlo trial move is the pressure swap. In our implementation, over long times, translation moves are attempted about half the time, rotation moves are attempted the other half and volume moves are attempted at every time. Additionally inter-replica pressure swaps are also attempted each time. Across replicas, the acceptance rates of each trial move should be approximately the same.[105] As the simulation progressed, the scale by which the a particle move was attempted was regulated for intra-replica moves. For example in a translation move, the amount by which a particle is moved is continuously modified such that if the acceptance rate for that move type is too high, the particle would attempt a larger displacement the next time that a translation move was attempted. Acceptance rates, defined as the number of accepted trial moves divided by the number of attempted trial moves, for intra-replica trial moves was approximately between $0.2 - 0.4$. For inter-replica particle exchanges, pressure swaps were also made between a given replica and the replica with adjacent pressure value. Pressure swap acceptance rates were also in the same range.

Since the ensembles are NPT at the end of the simulation time, although pressures were swapped periodically, configurations can be collated according to pressure such that for each pressure final results are effectively the same as if the particle

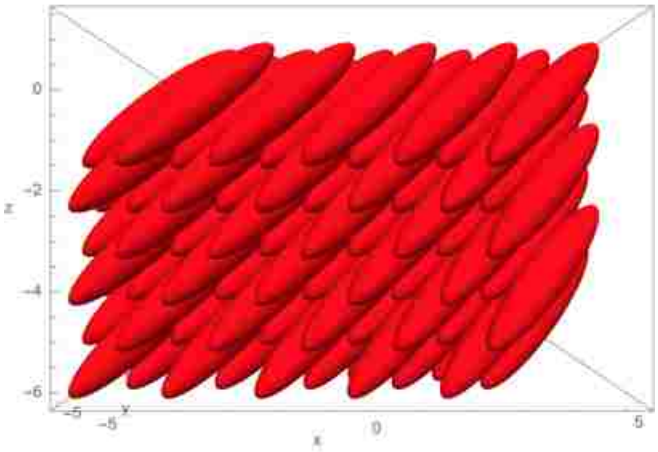

Figure 7.1: Visualization of the model particle, an ellipsoid with $\epsilon = 5$ in the simulation box. During initialization across all replicas, particles are placed on an FCC lattice and are all made to point diagonally in the same direction across the simulation box. As the simulation progresses, this structure melts. Some replicas will end in an isotropic phase. Some replicas will end in a nematic semi-ordered phase.

configurations have been swapped.

We want to explore the isotropic to nematic phase transition, so to do that, we have to run a set of replicas over a set of pressures high enough to give a high enough density to find the nematic transition. $N = 256$ particles are initialized on an FCC lattice with all unit vectors points diagonally across the simulation box (Fig. 7.1) This structure is allowed to melt and undergo the various Monte Carlo move types. Linear spacing between values of P were chosen to provide accurate estimates of the volume fraction ϕ of the phase transition point.

One Monte Carlo step is defined as each of N particles having a probability of having attempted some move type. In the original Odriozola model, an initial round of Monte Carlo sampling was done to $5X10^{12}$ Monte Carlo steps to ensure that the

system had reached equilibrium. An additional, $1X10^{13}$ steps were reported for sampling.

For practical reasons, these very long Monte Carlo simulation runs were not feasible. So our chosen Monte Carlo simulation lengths were up to $2X10^{7}$ steps. The convergence of this length of Monte Carlo runs resulted in calculated values having variance of $10^{-3}\%$.

7.4.1 Results

We were unable to confirm the results published literature results of Odriozola et al for $\epsilon = 5$ attractive square well-particles. Fig. 7.2 shows our results in blue superimposed upon those of Odriozla et al in black. For the one blue point shown, the difference between the volume fraction and the equivalent temperature volume fraction in black is $\approx 7\%$.

To ensure that the system had melted and no longer had signs of positional ordering, we examined the radial distribution function $g(r)$ for several values of the volume fraction. Using averages from multiple configurations after equilibrium and across various values for volume fraction, the radial distribution function did not show evidence of distinct positional ordering for any values of volume fraction examined. Fig. 7.3 shows an example of a calculated $g(r)$. At other volume fractions, $g(r)$ was virtually indistinguishable.

We made several attempts to accurately determine the phase transition point between the isotropic and nematic phase and employed several metrics. The order parameter for a simple nematic phase is expressed as the second legengre polynomial $P_2 = \frac{1}{2}3x^2 - 1$ where x is the director (average orientation of the long axis) of the particles. Using the results of our code P_2 can be expressed as $P_2 = \frac{1}{2}\left\langle 3(\hat{u}_i \cdot \hat{u}_j)^2 - 1 \right\rangle$. For a completely ordered nematic phase, in which all particles are exactly pointing in the same direction $P_2 = 1$, for an isotropic phase with no discernable preferred direction $P_2 = 0$

In the case of a non-uniaxial nematic phase, higher-order order parameters may reveal more information about particle orientation. Therefore we also examined the

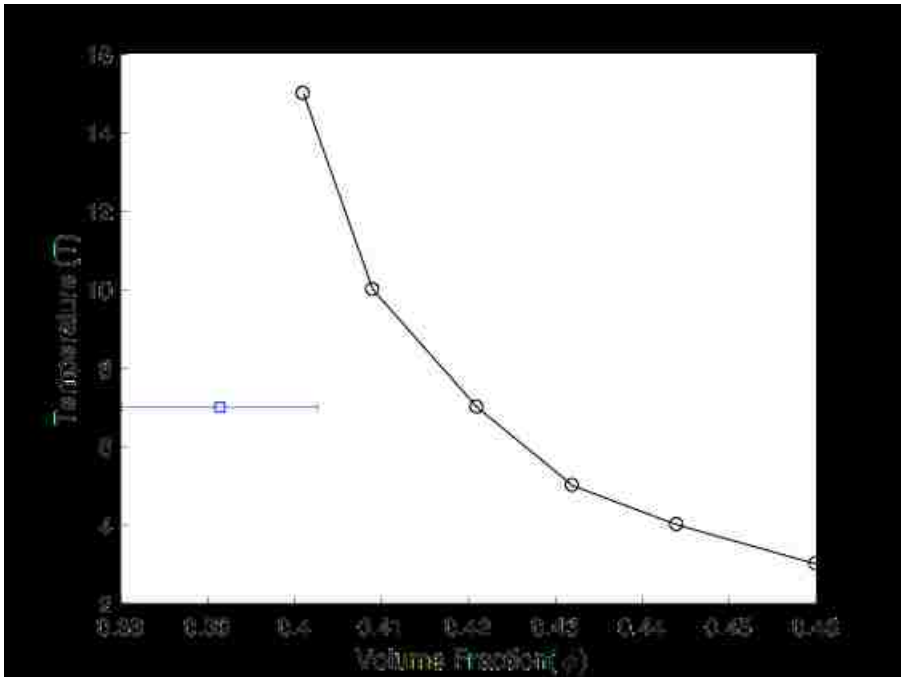

Figure 7.2: Phase diagram for the isotropic to nematic phase transition of $\epsilon = 5$ ellipsoid particles in an attractive quasi-square well. Published results from [131] in in black circles. Our results are shown by the blue square. Simulation temperature for our results was T=7 in standard reduced units.

next order parameter, expressed as the fourth order Legendre polynomial, $P_4 = \frac{1}{8}(35x^4 - 30x^2 + 3) = P_4 = \frac{1}{8}\langle 35(\hat{u}_i \cdot \hat{u}_j)^4 - 30(\hat{u}_i \cdot \hat{u}_j)^2 + 3\rangle$. Like P_2 a completely order phase has $P_4 = 1$ and an unordered phase has $P_4 = 0$. Fig. 7.4 shows the results of examining P_2 and P_4 vs volume fraction ϕ. Qualitatively, both P_2 and P_4 increase monotonically with ϕ indicating that the system is responsive to undergoing a phase transition. For a phase transition to occur, there must be some spontaneous symmetry breaking in the order parameter. This is illustrated by the clear uptick in both P_2 and P_4 at nearly the same point indicating that a phase transition must be in the vicinity of that value.

Another metric used to analyze the phase transition point was the isothermal compressibility β_T. Since it is known that β_T diverges near the critical point, but

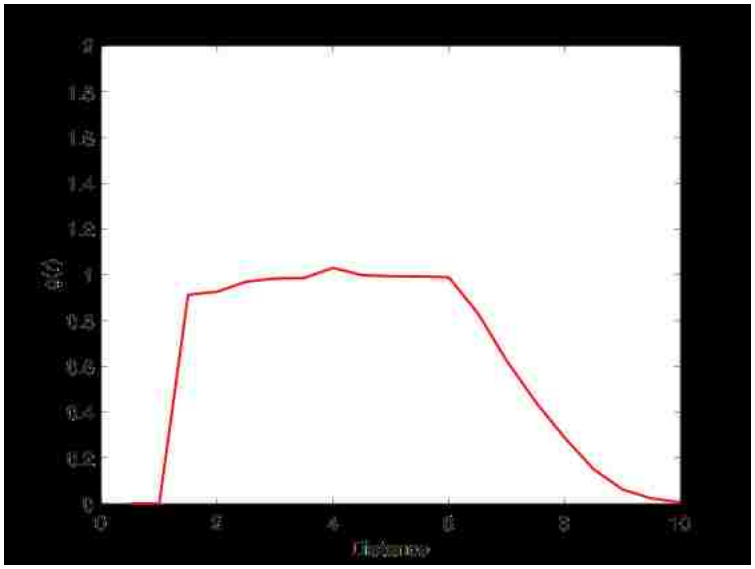

Figure 7.3: Sample radial distribution function $g(r)$ for a system of ellipsoidal particles calculated from 1000 average final configurations. Number density for $g(r)$ shown is $\rho = 0.1535$ and volume fraction $\phi = 0.4018$. Unit length is given by the diameter of the short side of the ellipsoid.

that behavior can be smoothed out a bit by the finite nature of simulations, a peak in a plot of the β_T indicates a phase transition. In this case since the simulation cell was allowed to change volume during the course of simulation, and the number of particles was held constant, β_T can be expressed via fluctuations in the number of density $\beta_T = \frac{<\rho^2>-<\rho>^2}{<\rho>^2}$. Fig.7.5 shows the results for β_T vs ϕ. There is a clear peak in β_T at $\phi = 0.3901$. This peak and the proximity of the changes in P_2 and P_4 were the primary methods by which the volume fraction ϕ_c of the phase transition was determined.

And indeed for values of ϕ less than our determined transition point, visualizations of the final particle configuration appears to show an isotropic fluid. For values of ϕ greater than the determined transition point, visualizations of the final particle configuration clearly show orientational ordering. Fig. 7.6 (a) and (b) shows particle visualizations for values less than ϕ_c and greater than ϕ_c respectively.

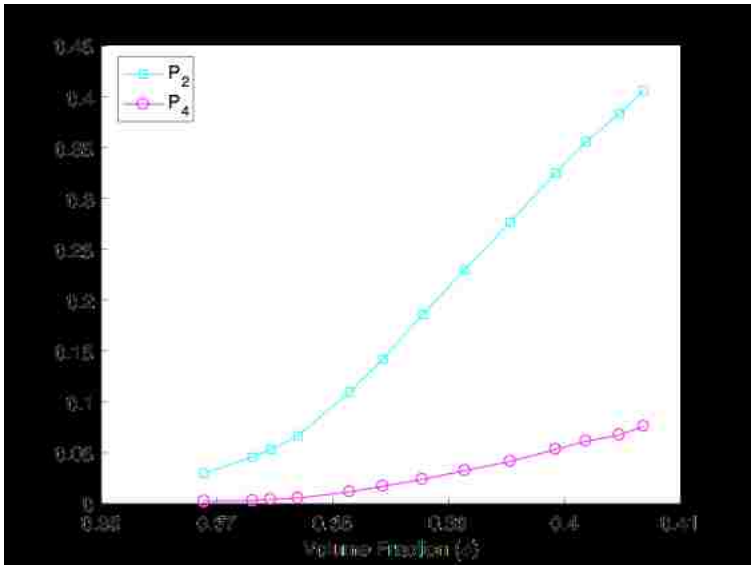

Figure 7.4: Nematic order parameters P_2 (cyan, squares) and P_4 (magenta, circles) vs volume fraction ϕ. Spontaneous change in order parameter indicate a phase transition. For both P_2 and P_4 there is a marked increase at volume fraction $\approx 0.38 - 0.39$. For the smallest value of ϕ studied, the $P_2 = ...$, whereas for the largest value of ϕ, $P_2 = ...$ The upward trend of P_2 and P_4 indicate that there is clearly an increase in ordering with larger values of ϕ.

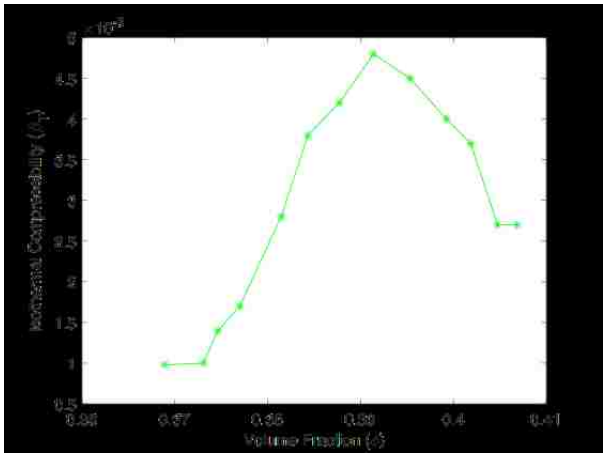

Figure 7.5: Isothermal Compressibility β_T vs Volume fraction ϕ. A peak in this graph indicates that a phase transition occurred. β_T peak at $\phi = 0.3914$ this is $\approx 7\%$ off from the value of the isotropic to nematic phase transition in literature.

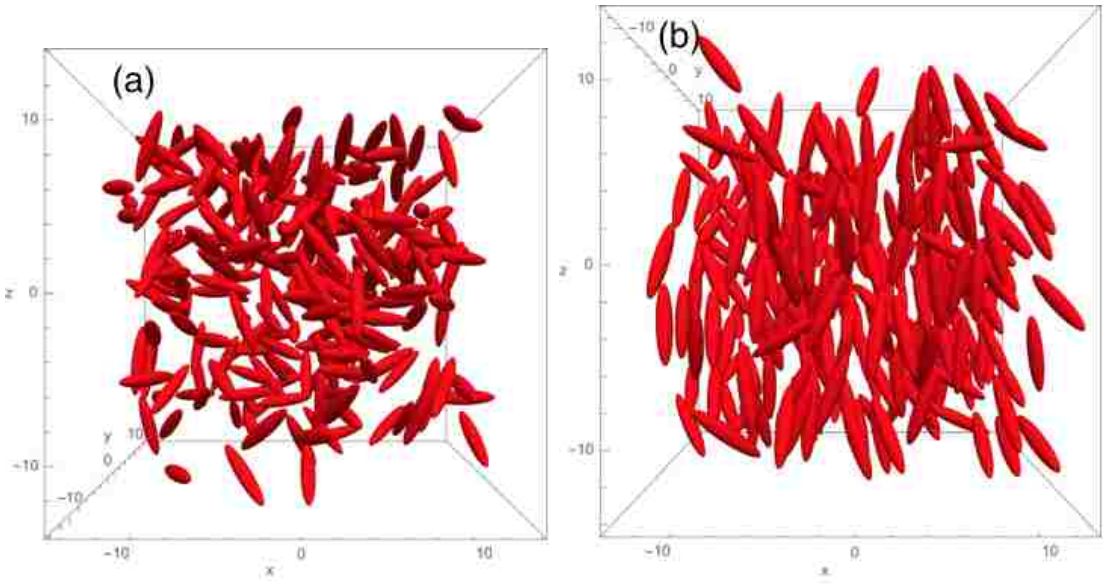

Figure 7.6: Examples of particle configurations visualized for a system in an isotropic phase (a) and nematic phase (b). The chosen configuration for visualization was the final configuration at the end of $2X10^7$ Monte Carlo steps. The volume fractions of the systems visualized are at 4% above and below our determined phase transition point at $\phi_c = 0.3914$

7.5 Conclusion

The discrepancies between our data and that of the published literature could possibly be the result of an extremely long equilibration time that was simply not able to be reached with the computing resources and time available. Perhaps the unusually long simulation times reported by Odriozola et al indicate that the system was not in fact in equilibrium and that the equilibration time is very extensive. Any possible reasons for this were not reported and unknown.

The problem of patchy ellipsoids undergoing an isotropic to nematic phase transition remains of interest, but at this time unsolved.

Bibliography

[1] S. Yadav T. W. Patapoff S. J. Shire A. Chaudri, I. E. Zarraga and G. A. Voth. *J. Phys. Chem. B*, 117:1269, 2013.

[2] James H Adair and Ender Suvaci. Morphological control of particles. *Current opinion in colloid & interface science*, 5(1):160–167, 2000.

[3] Marie Adams, Zvonimir Dogic, Sarah L Keller, and Seth Fraden. Entropically driven microphase transitions in mixtures of colloidal rods and spheres. *Nature*, 393(6683):349–352, 1998.

[4] Pinar Akcora, Hongjun Liu, Sanat K Kumar, Joseph Moll, Yu Li, Brian C Benicewicz, Linda S Schadler, Devrim Acehan, Athanassios Z Panagiotopoulos, Victor Pryamitsyn, et al. Anisotropic self-assembly of spherical polymer-grafted nanoparticles. *Nature materials*, 8(4):354–359, 2009.

[5] BJ Alder and TEf Wainwright. Phase transition for a hard sphere system. *The Journal of chemical physics*, 27(5):1208–1209, 1957.

[6] I Ali, D Marenduzzo, and JM Yeomans. Polymer packaging and ejection in viral capsids: shape matters. *Physical review letters*, 96(20):208102, 2006.

[7] Ronald P Andres, Jeffrey D Bielfeld, Jason I Henderson, David B Janes, et al. Self-assembly of a two-dimensional superlattice of molecularly linked metal clusters. *Science*, 273(5282):1690, 1996.

[8] Neer Asherie, Aleksey Lomakin, and George B Benedek. Phase diagram of colloidal solutions. *Physical review letters*, 77(23):4832, 1996.

[9] M.A. Athanassopoulou, D.M.P. Mingos, M.A. Bates, S.J. Clark, J. Crain, W. Haase, G.R. Luckhurst, B.I. Ostrovskii, and M.R. Wilson. *Liquid Crystals I.* Structure and Bonding. Springer Berlin Heidelberg, 2003.

[10] Stefan Auer. Phase diagram of polypeptide chains. *The Journal of chemical physics*, 135(17):175103, 2011.

[11] M. Baaden and S. J. Marrink. *Curr. Opin. in Structural Biology*, 23:878, 2013.

[12] Joseph K Bailey, C Jeffrey Brinker, and Martha L Mecartney. Growth mechanisms of iron oxide particles of differing morphologies from the forced hydrolysis of ferric chloride solutions. *Journal of Colloid and Interface Science*, 157(1):1–13, 1993.

[13] Gustavo Bautista-Carbajal, Arturo Moncho-Jordá, and Gerardo Odriozola. Further details on the phase diagram of hard ellipsoids of revolution. *The Journal of chemical physics*, 138(6):064501, 2013.

[14] T. Bereau and M. Deserno. *J. Chem. Phys.*, 130:235106, 2009.

[15] Bruce J Berne and Philip Pechukas. Gaussian model potentials for molecular interactions. *The Journal of Chemical Physics*, 56(8):4213–4216, 1972.

[16] Ludovic Berthier, Daniele Coslovich, Andrea Ninarello, and Misaki Ozawa. Equilibrium sampling of hard spheres up to the jamming density and beyond. *Physical review letters*, 116(23):238002, 2016.

[17] Emanuela Bianchi, Ronald Blaak, and Christos N Likos. Patchy colloids: state of the art and perspectives. *Physical Chemistry Chemical Physics*, 13(14):6397–6410, 2011.

[18] Emanuela Bianchi, Julio Largo, Piero Tartaglia, Emanuela Zaccarelli, and Francesco Sciortino. Phase diagram of patchy colloids: towards empty liquids. *Physical review letters*, 97(16):168301, 2006.

[19] Emanuela Bianchi, Piero Tartaglia, Emanuela Zaccarelli, and Francesco Sciortino. Theoretical and numerical study of the phase diagram of patchy colloids: Ordered and disordered patch arrangements. *The Journal of chemical physics*, 128(14):144504, 2008.

[20] Hari Krishna Bisoyi and Sandeep Kumar. Liquid-crystal nanoscience: an emerging avenue of soft self-assembly. *Chemical Society Reviews*, 40(1):306–319, 2011.

[21] L. Cailletet and E. C. Mathias. . *C. R. Acad. Sd.*, 102(1202), 1886.

[22] Philip J Camp, Carl P Mason, Michael P Allen, Anjali A Khare, and David A Kofke. The isotropic–nematic phase transition in uniaxial hard ellipsoid fluids: Coexistence data and the approach to the onsager limit. *The Journal of chemical physics*, 105(7):2837–2849, 1996.

[23] TN Carpency, JD Gunton, and JM Rickman. Phase behavior of patchy spheroidal fluids. *The Journal of Chemical Physics*, 145(21):214904, 2016.

[24] Murty SS Challa, David P Landau, and K Binder. Finite-size effects at temperature-driven first-order transitions. *Physical Review B*, 34(3):1841, 1986.

[25] Fang Chen, Mingfeng Chen, Ya-Wen Chang, Pengcheng Lin, Ying Chen, and Zhengdong Cheng. Polydispersity reduction of colloidal plates via size fractionation of the isotropic–nematic phase transition. *Soft Matter*, 13(20):3789–3793, 2017.

[26] Qian Chen, Sung Chul Bae, and Steve Granick. Directed self-assembly of a colloidal kagome lattice. *Nature*, 469(7330):381, 2011.

[27] Ting Chen and Sharon C Glotzer. Simulation studies of a phenomenological model for elongated virus capsid formation. *Physical Review E*, 75(5):051504, 2007.

[28] Wenduo Chen, Youliang Zhu, Fengchao Cui, Lunyang Liu, Zhaoyan Sun, Jizhong Chen, and Yunqi Li. Gpu-accelerated molecular dynamics simulation to study liquid crystal phase transition using coarse-grained gay-berne anisotropic potential. *PloS one*, 11(3):e0151704, 2016.

[29] Helmut Cölfen and Stephen Mann. Higher-order organization by mesoscale self-assembly and transformation of hybrid nanostructures. *Angewandte Chemie International Edition*, 42(21):2350–2365, 2003.

[30] P Cool, N Maes, I Heylen, M De Bock, and EF Vansant. Theoretical evaluation of pillared clay adsorbents: Part ii: Differences in porosity between al-pillared laponite and hectorite. *Journal of Porous Materials*, 3(3):157–168, 1996.

[31] Scott L Crick, Kiersten M Ruff, Kanchan Garai, Carl Frieden, and Rohit V Pappu. Unmasking the roles of n-and c-terminal flanking sequences from exon 1 of huntingtin as modulators of polyglutamine aggregation. *Proceedings of the National Academy of Sciences*, 110(50):20075–20080, 2013.

[32] D. H. deJong, G. Singh, W. F. D. Bennett, C. Arnarez, T. A. Wassenaar, L. V. Schäfer, X. Periole, D. P. Tieleman, and S. J. Marrink. *J. Chem. Theory and Computation*, 9:687, 2013.

[33] Zvonimir Dogic and Seth Fraden. Ordered phases of filamentous viruses. *Current opinion in colloid & interface science*, 11(1):47–55, 2006.

[34] Aleksandar Donev, Ibrahim Cisse, David Sachs, Evan A Variano, Frank H Stillinger, Robert Connelly, Salvatore Torquato, and Paul M Chaikin. Improving the density of jammed disordered packings using ellipsoids. *Science*, 303(5660):990–993, 2004.

[35] Aleksandar Donev, Frank H Stillinger, PM Chaikin, and Salvatore Torquato. Unusually dense crystal packings of ellipsoids. *Physical review letters*, 92(25):255506, 2004.

[36] Sergei A Egorov, Andrey Milchev, Peter Virnau, and Kurt Binder. A new insight into the isotropic–nematic phase transition in lyotropic solutions of semiflexible polymers: density-functional theory tested by molecular dynamics. *Soft Matter*, 12(22):4944–4959, 2016.

[37] Riccardo Fantoni, Domenico Gazzillo, Achille Giacometti, Mark A Miller, and Giorgio Pastore. Patchy sticky hard spheres: Analytical study and monte carlo simulations. *The Journal of chemical physics*, 127(23):234507, 2007.

[38] D. Feng and G. Jin. *Introduction to Condensed Matter Physics*. Number v. 1 in Introduction to Condensed Matter Physics. World Scientific, 2005.

[39] Michael E Fisher. The renormalization group in the theory of critical behavior. *Reviews of Modern Physics*, 46(4):597, 1974.

[40] Seth Fraden, Georg Maret, DLD Caspar, and Robert B Meyer. Isotropic-nematic phase transition and angular correlations in isotropic suspensions of tobacco mosaic virus. *Physical review letters*, 63(19):2068, 1989.

[41] D Frenkel and BM Mulder. The hard ellipsoid-of-revolution fluid: I. monte carlo simulations. *Molecular physics*, 55(5):1171–1192, 1985.

[42] D Frenkel, BM Mulder, and JP McTague. Phase diagram of a system of hard ellipsoids. *Physical review letters*, 52(4):287, 1984.

[43] Daan Frenkel and Berend Smit. *Understanding Molecular Simulation: From Algorithms to Applications (Computational Science)*. Academic Press, 2001.

[44] Jean-Christophe P Gabriel, Clément Sanchez, and Patrick Davidson. Observation of nematic liquid-crystal textures in aqueous gels of smectite clays. *The Journal of Physical Chemistry*, 100(26):11139–11143, 1996.

[45] Oleg Galkin and Peter G Vekilov. Control of protein crystal nucleation around the metastable liquid–liquid phase boundary. *Proceedings of the National Academy of Sciences*, 97(12):6277–6281, 2000.

[46] Achille Giacometti, Fred Lado, Julio Largo, Giorgio Pastore, and Francesco Sciortino. Effects of patch size and number within a simple model of patchy colloids. *The Journal of chemical physics*, 132(17):174110, 2010.

[47] Sharon C Glotzer and Michael J Solomon. Anisotropy of building blocks and their assembly into complex structures. *Nature materials*, 6(8):557–562, 2007.

[48] Sylvain Grouazel, Francoise Bonnete, Jean-Pierre Astier, Natalie Ferte, Javier Perez, and Stephane Veesler. Exploring bovine pancreatic trypsin inhibitor phase transitions. *The Journal of Physical Chemistry B*, 110(39):19664–19670, 2006.

[49] Marek Grzelczak, Jan Vermant, Eric M Furst, and Luis M Liz-Marzán. Directed self-assembly of nanoparticles. *ACS nano*, 4(7):3591–3605, 2010.

[50] F de J Guevara-Rodríguez and G Odriozola. Hard ellipsoids: Analytically approaching the exact overlap distance. *The Journal of chemical physics*, 135(8):084508, 2011.

[51] E Ao Guggenheim. The principle of corresponding states. *The Journal of Chemical Physics*, 13(7):253–261, 1945.

[52] Florian Günther, Florian Janoschek, Stefan Frijters, and Jens Harting. Lattice boltzmann simulations of anisotropic particles at liquid interfaces. *Computers & Fluids*, 80:184–189, 2013.

[53] James D Gunton, Andrey Shiryayev, and Daniel L Pagan. *Protein condensation: kinetic pathways to crystallization and disease*. Cambridge university press, 2007.

[54] C Haas, J Drenth, and W William Wilson. Relation between the solubility of proteins in aqueous solutions and the second virial coefficient of the solution. *The Journal of Physical Chemistry B*, 103(14):2808–2811, 1999.

[55] T. X. Hoang, A. Trovato, F. Seno, J. R. Banavar, and A. Maritan. *Proc. Natl. Acad. Sci*, 101:7960, 2004.

[56] Nikhil R Jana. Shape effect in nanoparticle self-assembly. *Angewandte Chemie International Edition*, 43(12):1536–1540, 2004.

[57] Shan Jiang, Qian Chen, Mukta Tripathy, Erik Luijten, Kenneth S Schweizer, and Steve Granick. Janus particle synthesis and assembly. *Advanced materials*, 22(10):1060–1071, 2010.

[58] Matthew R Jones, Robert J Macfarlane, Andrew E Prigodich, Pinal C Patel, and Chad A Mirkin. Nanoparticle shape anisotropy dictates the collective behavior of surface-bound ligands. *Journal of the American Chemical Society*, 133(46):18865–18869, 2011.

[59] Takashi Kato, Norihiro Mizoshita, and Kenji Kishimoto. Functional liquid-crystalline assemblies: self-organized soft materials. *Angewandte Chemie International Edition*, 45(1):38–68, 2006.

[60] Norbert Kern and Daan Frenkel. Fluid–fluid coexistence in colloidal systems with short-ranged strongly directional attraction. *The Journal of chemical physics*, 118(21):9882–9889, 2003.

[61] Norbert Kern and Daan Frenkel. Fluid–fluid coexistence in colloidal systems with short-ranged strongly directional attraction. *The Journal of chemical physics*, 118(21):9882–9889, 2003.

[62] Siddique Khan, Jason Haaga, and JD Gunton. Kinetics of aggregation of an anisotropic model of self-assembling molecules. *The Journal of chemical physics*, 143(2):024906, 2015.

[63] Jin-Woong Kim, Ryan J Larsen, and David A Weitz. Synthesis of nonspherical colloidal particles with anisotropic properties. *Journal of the American Chemical Society*, 128(44):14374–14377, 2006.

[64] Sebastian Kmiecik, Dominik Gront, Michal Kolinski, Lukasz Wieteska, Aleksandra Elzbieta Dawid, and Andrzej Kolinski. Coarse-grained protein models and their applications. *Chemical Reviews*, 116(14):7898–7936, 2016.

[65] Tuomas PJ Knowles, Michele Vendruscolo, and Christopher M Dobson. The amyloid state and its association with protein misfolding diseases. *Nature reviews Molecular cell biology*, 15(6):384–396, 2014.

[66] Vinal V Lakhani, Feng Ding, and Nikolay V Dokholyan. Polyglutamine induced misfolding of huntingtin exon1 is modulated by the flanking sequences. *PLoS computational biology*, 6(4):e1000772, 2010.

[67] David Landau and Kurt Binder. *A Guide to Monte Carlo Simulations in Statistical Physics*. Cambridge University Press, New York, NY, USA, 2005.

[68] Kyung Jin Lee, Jaewon Yoon, and Joerg Lahann. Recent advances with anisotropic particles. *Current opinion in colloid & interface science*, 16(3):195–202, 2011.

[69] Na Li, Pengxiang Zhao, and Didier Astruc. Anisotropic gold nanoparticles: synthesis, properties, applications, and toxicity. *Angewandte Chemie International Edition*, 53(7):1756–1789, 2014.

[70] Wei Li and James D Gunton. Self-assembly of janus ellipsoids ii: Janus prolate spheroids. *Langmuir*, 29(27):8517–8523, 2013.

[71] Wei Li, Ya Liu, Genevieve Brett, and James D Gunton. Encapsulation by janus spheroids. *Soft Matter*, 8(22):6027–6032, 2012.

[72] Wei Li, Donovan Ruth, James D Gunton, and Jeffrey M Rickman. Selective encapsulation by janus particles. *The Journal of chemical physics*, 142(24):244705, 2015.

[73] Hongjun Liu, Sanat K Kumar, Francesco Sciortino, and Glenn T Evans. Vapor-liquid coexistence of fluids with attractive patches: an application of wertheims theory of association. *The Journal of chemical physics*, 130(4):044902, 2009.

[74] Ya Liu, Wei Li, Toni Perez, James D Gunton, and Genevieve Brett. Self assembly of janus ellipsoids. *Langmuir*, 28(1):3–9, 2011.

[75] Aleksey Lomakin, Neer Asherie, and George B Benedek. Aeolotopic interactions of globular proteins. *Proceedings of the National Academy of Sciences*, 96(17):9465–9468, 1999.

[76] Vinothan N Manoharan, Mark T Elsesser, and David J Pine. Dense packing and symmetry in small clusters of microspheres. *Science*, 301(5632):483–487, 2003.

[77] Vasilios I Manousiouthakis and Michael W Deem. Strict detailed balance is unnecessary in monte carlo simulation. *The Journal of chemical physics*, 110(6):2753–2756, 1999.

[78] Jennifer J McManus, Patrick Charbonneau, Emanuela Zaccarelli, and Neer Asherie. The physics of protein self-assembly. *Current Opinion in Colloid & Interface Science*, 22:73–79, 2016.

[79] E Meneses-Juarez, S Varga, P Orea, and G Odriozola. Towards understanding the empty liquid of colloidal platelets: Vapour–liquid phase coexistence of square-well oblate ellipsoids. *Soft Matter*, 9(21):5277–5284, 2013.

[80] Nicholas Metropolis, Arianna W Rosenbluth, Marshall N Rosenbluth, Augusta H Teller, and Edward Teller. Equation of state calculations by fast computing machines. *The journal of chemical physics*, 21(6):1087–1092, 1953.

[81] A. Morriss-Andrews and Joan-Emma Shea. *J. Phys. Chem. Lett.*, 5:1899, 2014.

[82] Milan Mrksich and George M Whitesides. Using self-assembled monolayers to understand the interactions of man-made surfaces with proteins and cells. *Annual review of biophysics and biomolecular structure*, 25(1):55–78, 1996.

[83] A. Mulero. *Theory and Simulation of Hard-Sphere Fluids and Related Systems*. Lecture Notes in Physics. Springer Berlin Heidelberg, 2008.

[84] Gianmarco Munao, Zdenek Preisler, Teun Vissers, Frank Smallenburg, and Francesco Sciortino. Cluster formation in one-patch colloids: low coverage results. *Soft Matter*, 9(9):2652–2661, 2013.

[85] Arthur C Newton, Jan Groenewold, Willem K Kegel, and Peter G Bolhuis. Rotational diffusion affects the dynamical self-assembly pathways of patchy particles. *Proceedings of the National Academy of Sciences*, 112(50):15308–15313, 2015.

[86] Trung Dac Nguyen, Eric Jankowski, and Sharon C Glotzer. Self-assembly and reconfigurability of shape-shifting particles. *ACS nano*, 5(11):8892–8903, 2011.

[87] Steve O Nielsen, Carlos F Lopez, Goundla Srinivas, and Michael L Klein. Coarse grain models and the computer simulation of soft materials. *Journal of Physics: Condensed Matter*, 16(15):R481, 2004.

[88] Takasi Nisisako, Toru Torii, Takanori Takahashi, and Yoichi Takizawa. Synthesis of monodisperse bicolored janus particles with electrical anisotropy using a microfluidic co-flow system. *Advanced Materials*, 18(9):1152–1156, 2006.

[89] WG Noid. Perspective: Coarse-grained models for biomolecular systems. *The Journal of chemical physics*, 139(9):090901, 2013.

[90] Massimo G Noro and Daan Frenkel. Extended corresponding-states behavior for particles with variable range attractions. *The Journal of Chemical Physics*, 113(8):2941–2944, 2000.

[91] Gerardo Odriozola. Replica exchange monte carlo applied to hard spheres. *The Journal of chemical physics*, 131(14):144107, 2009.

[92] Gerardo Odriozola. Revisiting the phase diagram of hard ellipsoids. *The Journal of chemical physics*, 136(13):134505, 2012.

[93] Lars Onsager. The effects of shape on the interaction of colloidal particles. *Annals of the New York Academy of Sciences*, 51(1):627–659, 1949.

[94] DL Pagan and JD Gunton. Phase behavior of short-range square-well model. *The Journal of chemical physics*, 122(18):184515, 2005.

[95] Athanassios Z Panagiotopoulos. Direct determination of phase coexistence properties of fluids by monte carlo simulation in a new ensemble. *Molecular Physics*, 61(4):813–826, 1987.

[96] AZ Panagiotopoulos. Molecular simulation of phase coexistence: Finite-size effects and determination of critical parameters for two-and three-dimensional lennard-jones fluids. *International journal of thermophysics*, 15(6):1057–1072, 1994.

[97] Amar B Pawar and Ilona Kretzschmar. Multifunctional patchy particles by glancing angle deposition. *Langmuir*, 25(16):9057–9063, 2009.

[98] Amar B Pawar and Ilona Kretzschmar. Fabrication, assembly, and application of patchy particles. *Macromolecular rapid communications*, 31(2):150–168, 2010.

[99] Max F Perutz and AH Windle. Cause of neural death in neurodegenerative diseases attributable to expansion of glutamine repeats. *Nature*, 412(6843):143–144, 2001.

[100] Zdeněk Preisler, Teun Vissers, Gianmarco Munaò, Frank Smallenburg, and Francesco Sciortino. Equilibrium phases of one-patch colloids with short-range attractions. *Soft Matter*, 10(28):5121–5128, 2014.

[101] Zdenek Preisler, Teun Vissers, Frank Smallenburg, Gianmarco Munao, and Francesco Sciortino. Phase diagram of one-patch colloids forming tubes and lamellae. *The Journal of Physical Chemistry B*, 117(32):9540–9547, 2013.

[102] Kirstin R Purdy, Zvonimir Dogic, Seth Fraden, Adrian Rühm, Lawrence Lurio, and Simon GJ Mochrie. Measuring the nematic order of suspensions of colloidal fd virus by x-ray diffraction and optical birefringence. *Physical Review E*, 67(3):031708, 2003.

[103] Kirstin R Purdy, Szabolcs Varga, Amparo Galindo, George Jackson, and Seth Fraden. Nematic phase transitions in mixtures of thin and thick colloidal rods. *Physical review letters*, 94(5):057801, 2005.

[104] Marc Radu, Patrick Pfleiderer, and Tanja Schilling. Solid-solid phase transition in hard ellipsoids. *The Journal of chemical physics*, 131(16):164513, 2009.

[105] Nitin Rathore, Manan Chopra, and Juan J de Pablo. Optimal allocation of replicas in parallel tempering simulations. *The Journal of chemical physics*, 122(2):024111, 2005.

[106] Serge Ravaine and Etienne Duguet. Synthesis and assembly of patchy particles: Recent progress and future prospects. *Current Opinion in Colloid & Interface Science*, 2017.

[107] Kristian Rechendorff, Mads Bruun Hovgaard, Morten Foss, VP Zhdanov, and Flemming Besenbacher. Enhancement of protein adsorption induced by surface roughness. *Langmuir*, 22(26):10885–10888, 2006.

[108] Gerald Rickayzen. A model for the study of the structure of hard molecular fluids. *Molecular Physics*, 95(2):393–400, 1998.

[109] Flavio Romano and Francesco Sciortino. Two dimensional assembly of triblock janus particles into crystal phases in the two bond per patch limit. *Soft Matter*, 7(12):5799–5804, 2011.

[110] Flavio Romano and Francesco Sciortino. Colloidal self-assembly: patchy from the bottom up. *Nature materials*, 10(3):171–173, 2011 publisher=Nature Publishing Group.

[111] Marshall N Rosenbluth and Arianna W Rosenbluth. Further results on monte carlo equations of state. *The Journal of Chemical Physics*, 22(5):881–884, 1954.

[112] Christopher A Ross and Michelle A Poirier. Protein aggregation and neurodegenerative disease. 2004.

[113] John Russo, Piero Tartaglia, and Francesco Sciortino. Reversible gels of patchy particles: role of the valence. *The Journal of chemical physics*, 131(1):014504, 2009.

[114] John Russo, Piero Tartaglia, and Francesco Sciortino. Association of limited valence patchy particles in two dimensions. *Soft Matter*, 6(17):4229–4236, 2010.

[115] DP Ruth, JD Gunton, JM Rickman, and Wei Li. The impact of anisotropy and interaction range on the self-assembly of janus ellipsoids. *The Journal of chemical physics*, 141(21):214903, 2014.

[116] Barbara Ruzicka, Emanuela Zaccarelli, Laura Zulian, Roberta Angelini, Michael Sztucki, Abdellatif Moussaïd, Theyencheri Narayanan, and Francesco Sciortino. Observation of empty liquids and equilibrium gels in a colloidal clay. *Nature materials*, 10(1):56, 2011.

[117] Stefano Sacanna, David J Pine, and Gi-Ra Yi. Engineering shape: the novel geometries of colloidal self-assembly. *Soft Matter*, 9(34):8096–8106, 2013.

[118] Francesco Sciortino, Achille Giacometti, and Giorgio Pastore. Phase diagram of janus particles. *Physical review letters*, 103(23):237801, 2009.

[119] Francesco Sciortino, Achille Giacometti, and Giorgio Pastore. A numerical study of one-patch colloidal particles: from square-well to janus. *Physical Chemistry Chemical Physics*, 12(38):11869–11877, 2010.

[120] Francesco Sciortino and Emanuela Zaccarelli. Reversible gels of patchy particles. *Current Opinion in Solid State and Materials Science*, 15(6):246–253, 2011.

[121] Dennis J Selkoe. Alzheimer's disease: a central role for amyloid. *Journal of Neuropathology & Experimental Neurology*, 53(5):438–447, 1994.

[122] Aayush A Shah, Benjamin Schultz, Kevin L Kohlstedt, Sharon C Glotzer, and Michael J Solomon. Synthesis, assembly, and image analysis of spheroidal patchy particles. *Langmuir*, 29(15):4688–4696, 2013.

[123] Aayush A Shah, Benjamin Schultz, Wenjia Zhang, Sharon C Glotzer, and Michael J Solomon. Actuation of shape-memory colloidal fibres of janus ellipsoids. *Nature materials*, 14(1):117–124, 2015.

[124] Roland J Siezen, Michael R Fisch, Christine Slingsby, and George B Benedek. Opacification of gamma-crystallin solutions from calf lens in relation to cold cataract formation. *Proceedings of the National Academy of Sciences*, 82(6):1701–1705, 1985.

[125] Frank Smallenburg and Francesco Sciortino. Liquids more stable than crystals in particles with limited valence and flexible bonds. *Nature Physics*, 9(9):554–558, 2013.

[126] Michael J Solomon and Patrick T Spicer. Microstructural regimes of colloidal rod suspensions, gels, and glasses. *Soft Matter*, 6(7):1391–1400, 2010.

[127] Kari Thorkelsson, Peter Bai, and Ting Xu. Self-assembly and applications of anisotropic nanomaterials: A review. *Nano Today*, 10(1):48–66, 2015.

[128] Salvatore Torquato and Frank H Stillinger. Jammed hard-particle packings: From kepler to bernal and beyond. *Reviews of modern physics*, 82(3):2633, 2010.

[129] Valentina Tozzini. Coarse-grained models for proteins. *Current opinion in structural biology*, 15(2):144–150, 2005.

[130] Robert Vácha and Daan Frenkel. Relation between molecular shape and the morphology of self-assembling aggregates: a simulation study. *Biophysical journal*, 101(6):1432–1439, 2011.

[131] S Varga, E Meneses-Juarez, and G Odriozola. Empty liquid state and self-assembly of high valence non-spherical colloidal systems. *Soft Matter*, 9(47):11178–11182, 2013.

[132] Szabolcs Varga, Efrain Meneses-Júarez, and Gerardo Odriozola. Empty liquid phase of colloidal ellipsoids: The role of shape and interaction anisotropy. *The Journal of chemical physics*, 140(13):134905, 2014.

[133] Lourdes Vega, Enrique de Miguel, Luis F Rull, George Jackson, and Ian A McLure. Phase equilibria and critical behavior of square-well fluids of variable width by gibbs ensemble monte carlo simulation. *The Journal of chemical physics*, 96(3):2296–2305, 1992.

[134] Jacques Vieillard-Baron. The equation of state of a system of hard spherocylinders. *Molecular Physics*, 28(3):809–818, 1974.

[135] Andreas Walther and Axel HE Müller. Janus particles: synthesis, self-assembly, physical properties, and applications. *Chem. Rev*, 113(7):5194–5261, 2013.

[136] Ting Wang, Minxuan Kuang, Feng Jin, Jinhua Cai, Lei Shi, Yongmei Zheng, Jingxia Wang, and Lei Jiang. Simultaneous synthesis/assembly of anisotropic cake-shaped porphyrin particles toward colloidal microcrystals. *Chemical Communications*, 52(18):3619–3622, 2016.

[137] Georgina MH Wilkins, Patrick T Spicer, and Michael J Solomon. Colloidal system to explore structural and dynamical transitions in rod networks, gels, and glasses. *Langmuir*, 25(16):8951–8959, 2009.

[138] Tim E Williamson, Andreas Vitalis, Scott L Crick, and Rohit V Pappu. Modulation of polyglutamine conformations and dimer formation by the n-terminus of huntingtin. *Journal of molecular biology*, 396(5):1295–1309, 2010.

[139] Kenneth G Wilson. Renormalization group and strong interactions. *Physical Review D*, 3(8):1818, 1971.

[140] Gerard CL Wong, Jay X Tang, Alison Lin, Youli Li, Paul A Janmey, and Cyrus R Safinya. Hierarchical self-assembly of f-actin and cationic lipid complexes: stacked three-layer tubule networks. *Science*, 288(5473):2035–2039, 2000.

[141] Chun Wu and Joan-Emma Shea. Coarse-grained models for protein aggregation. *Current opinion in structural biology*, 21(2):209–220, 2011.

[142] Jing Xu, Yali Wang, and Xuehao He. Self-assembly of janus ellipsoids: a brownian dynamics simulation with a quantitative nonspherical-particle model. *Soft matter*, 11(37):7433–7439, 2015.

[143] Gi-Ra Yi, David J Pine, and Stefano Sacanna. Recent progress on patchy colloids and their self-assembly. *Journal of Physics: Condensed Matter*, 25(19):193101, 2013.

[144] Yadong Yin, Yu Lu, Byron Gates, and Younan Xia. Template-assisted self-assembly: a practical route to complex aggregates of monodispersed colloids with well-defined sizes, shapes, and structures. *Journal of the American Chemical Society*, 123(36):8718–8729, 2001.

[145] Michele Zanini and Lucio Isa. Particle contact angles at fluid interfaces: pushing the boundary beyond hard uniform spherical colloids. *J. Phys.: Condens. Matter*, 28:313002, 2016.

[146] GJ Zarragoicoechea, D Levesque, and JJ Weis. Monte carlo study of dipolar ellipsoids. ii. search for an isotropic-nematic phase transition. *Molecular Physics*, 75(5):989–998, 1992.

[147] Junhu Zhang, Yunfeng Li, Xuemin Zhang, and Bai Yang. Colloidal self-assembly meets nanofabrication: From two-dimensional colloidal crystals to nanostructure arrays. *Advanced materials*, 22(38):4249–4269, 2010.

Vita

Maria Nguyen Thienbao was born and raised in Colorado. She received a Bachelor of Science with double majors in physics and math from the University of Denver in 2012. In August of that year, she started graduate school at Lehigh University and obtained her Master of Science in physics in 2014. In 2016 she married Mark Carpency and published her first paper, "Phase Behavior of Patchy Spheroidal Fluids" in the Journal of Chemical Physics with Dr. James Gunton and Dr. Jeffrey Rickman as T.N.Carpency. She obtained her PhD in January 2018.